Coherent and squeezed phonons in semiconductor quantum wells

Simulating optically-induced lattice dynamics

Thomas Papenkort

Coherent and squeezed phonons in semiconductor quantum wells: Simulating optically-induced lattice dynamics

Inaugural-Dissertation zur Erlangung des Doktorgrades der Naturwissenschaften im Fachbereich Physik der Mathematisch-Naturwissenschaftlichen Fakultät der Westfälischen Wilhelms-Universität Münster

Dissertation in partial fulfillment of the requirements for a doctoral degree presented to the Department of Physics of the Faculty of Mathematics and Natural Sciences at the University of Muenster

vorgelegt von | *submitted by*: Thomas Papenkort
aus | *from*: Bocholt

2012

URN: urn:nbn:de:hbz:6-59359474648
URL: http://nbn-resolving.de/urn:nbn:de:hbz:6-59359474648

Dekan | *Dean*	Prof. Dr. Tilmann Kuhn
Erster Gutachter | *First Referee*	Prof. Dr. Tilmann Kuhn
Zweiter Gutachter | *Second Referee*	Prof. Dr. Vollrath Martin Axt
Tag der mündlichen Prüfung | *Date of Defense*	26.11.2012
Tag der Promotion | *Date of Graduation*	26.11.2012

Contents (short)

Contents

Abstract

This thesis is about how the crystal lattice of a semiconductor can be put into certain non-equilibrium states, in particular states with coherent and squeezed phonons. To this end, the dynamics of GaAs/AlAs quantum wells under ultrafast optical excitation is simulated by quantum kinetic calculations.

Many experiments have shown that a short laser pulse can excite lattice oscillations in solids; in other words, the pulse creates coherent phonons. This is often explained by an effective direct coupling of the lattice to the light field, although the process in reality is indirect: the optical pulse affects the electronic subsystem, which in turn acts on the lattice. The microscopic model adopted in this work therefore consists of the following parts: the electronic states of the quantum well (including subband quantization and Coulomb interaction), their driving by a laser field, and the coupling to the longitudinal-optical phonon branch. This allows to successfully describe the generation of coherent phonons in the regime of the effective-coupling mechanisms as well as situations in which the electronic subsystem cannot be factored out. Such a situation arises when a quantum beat is excited whose frequency is matched to a phonon frequency, which provides a resonant driving that very efficiently creates coherent phonons. The simulations agree well with experiments on this subject. Additionally they show that most of the energy flowing into the lattice actually goes into incoherent phonons, i.e., it does not serve to amplify the oscillation but only increases the quantum fluctuations of the lattice.

In a squeezed phonon state, those fluctuations are particularly small: the quantum-mechanical uncertainty of either the position or the momentum of the lattice nuclei is reduced to a value smaller than that at absolute zero temperature. Any measurement of the uncertainties will always record some spatial average, which is shown to significantly change the perceived uncertainties. Spatial averaging hence has to be accounted for in the calculations; as a side effect, this can substantially reduce the numerical complexity. The ways in which squeezed phonon states can be created are analyzed in detail. Depending on its parameters, a single Gaussian pulse can produce a phonon state that is very close to a prototypical squeezed state; a state with sustained squeezing of lattice displacement; or a strong oscillation of the position uncertainty that for certain times breaks the zero-point limit. A sequence of two pulses resonant with the lowest exciton transition can also be employed to create squeezed states. At non-cryogenic temperatures, thermal noise becomes important. In that case, squeezing below the thermal limit can be obtained, for example, by tuning the laser to an energy that lies below the band gap by the energy of one phonon. This leads to absorption of incoherent thermal phonons and in this way reduces the uncertainty of both lattice variables.

Zusammenfassung

In dieser Dissertation geht es darum, wie das Kristallgitter eines Halbleiters in spezielle Nichtgleichgewichtszustände versetzt werden kann, insbesondere in solche, die aus kohärenten oder gequetschten Phononen bestehen. Dazu wird quantenkinetisch die Dynamik eines GaAs/AlAs-Quantenfilms berechnet, der durch ultrakurze Laserpulse angeregt wird.

In einer Vielzahl von Experimenten wurde gezeigt, dass das Kristallgitter eines Festkörpers in Schwingung versetzt wird, wenn man ihn mit einem kurzen Laserpuls anregt; der Puls erzeugt also kohärente Phononen. Oft lässt sich das durch eine effektive direkte Kopplung zwischen Lichtfeld und Gitter erklären, obwohl die Anregung eigentlich indirekt erfolgt: Der Laserpuls regt Elektronen an, und diese wiederum bewirken eine Kraft auf das Gitter. Das in dieser Arbeit verwendete Modell besteht deshalb aus dem elektronischen System des Quantenfilms (einschließlich Subbandstruktur und Coulomb-Wechselwirkung), dem treibenden Lichtfeld und die Ankopplung an die longitudinal-optischen Phononen. Die Simulationen beschreiben damit erfolgreich sowohl Erzeugungsmechanismen, bei denen die Annahme einer direkten Kopplung gerechtfertigt ist, als auch solche, in denen die Dynamik des elektronischen Systems nicht vernachlässigt werden kann. Ein Beispiel für Letztere ist die resonante Erzeugung von kohärenten Phononen, bei der eine Quantenschwebung angeregt wird, deren Frequenz zu der einer Phononmode passt. Diese Methode produziert sehr effizient eine kohärente Gitterschwingung, wie Experimente zeigen. Die Simulationen stimmen mit diesen Experimenten gut überein; sie zeigen außerdem, dass der größte Teil der dem Gitter zugeführten Energie in inkohärente Phononen fließt, also statt die Gitterschwingung anzutreiben nur die Quantenfluktuationen des Gitters erhöht.

Ein gequetschter Phononzustand liegt vor, wenn die quantenmechanische Unschärfe entweder der Gitterauslenkung oder des zugehörigen Impulses unter den Wert fällt, den sie am absoluten Temperaturnullpunkt hätte. Eine Messung der Unschärfen ist experimentell nicht möglich, ohne über viele Gitteratome zu mitteln. Die gemittelten Größen haben eine verringerte Unschärfe und die Mittelung muss deshalb in den Rechnungen berücksichtigt werden; ein positiver Nebeneffekt ist, dass dadurch auch die numerische Berechnung vereinfacht werden kann. Es werden verschiedene Möglichkeiten gezeigt, wie sich gequetschte Phononzustände erzeugen lassen. Ein einzelner Laserpuls kann, abhängig von seinen genauen Eigenschaften, einen Zustand sehr ähnlich zum prototypischen gequetschten Zustand erzeugen; die Impulsunschärfe dauerhaft herabsetzen; oder eine starke Oszillation der Positionsunschärfe auslösen, die für kurze Zeit das Nullpunktniveau unterschreitet. Zwei Pulse hintereinander, die beide auf die unterste Exzitonlinie eingestellt sind, können ebenfalls Quetschen hervorrufen. Bei höheren Temperaturen sind einige Phononen thermisch angeregt und die Unschärfen entsprechend erhöht. In diesem Fall können beispielsweise mithilfe eines Laserpulses, dessen Energie gerade um eine Phononenergie unterhalb der Bandlücke liegt, inkohärente thermische Phononen wieder vernichtet werden, um so beide Unschärfen gleichzeitig zu verkleinern und sie unter ihre thermischen Gleichgewichtswerte abzusenken.

Introduction

Phonons are often perceived as just a source of noise and decoherence, limiting the effectiveness of electronic devices. Indeed the technical applications that rely on electronic dynamics far outreach those which employ phonons. Nevertheless, the dynamics of phonons deserves attention in its own right, and for this endeavor the often undesirable coupling of the electrons to the lattice becomes a blessing: It provides us with the means to control the lattice dynamics, i.e., to prepare and measure special phonon states. In particular two kinds of non-equilibrium phonon states are discussed in this work, states with coherent phonons and squeezed phonon states.

The physical system under investigation is a semiconductor quantum well driven by short laser pulses, whose dynamics is simulated by quantum kinetic calculations. The big advantage of quantum wells is that their quantum properties can be tailored to our needs, while they also are relatively easily accessible in experiments and theoretically well understood. Excitation with laser pulses is a very well established technique capable of reaching the pico- to femtosecond timescales that govern the electronic and phononic dynamics.

An ultrashort laser pulse incident on the quantum well in many cases creates an oscillation of the lattice nuclei; in other words, coherent phonons are excited. The excitation process is an indirect one: The pulse rapidly changes the electronic subsystem, which exerts a force on the crystal lattice and in this way drives an oscillation of the lattice. Different mechanisms for generating coherent phonons will be discussed, in particular a resonant mechanism in which an electronic quantum beat is tuned to a phonon frequency. That mechanism is quite effective, but also produces a large amount of incoherent phonons, which in simple terms means that the lattice is heated up. Comparison with experiments attests to the validity of the simulations.

The crystal lattice is an inherently quantum-mechanical system, and therefore the lattice nuclei carry a quantum uncertainty blurring their position and momentum. Even at absolute zero temperature the uncertainties are not reduced to zero. The Heisenberg principle mandates a lower bound only for the product of position and momentum uncertainties, and hence it is possible to lower one of those uncertainties while increasing the other. A state in which one of the uncertainties is smaller than its zero-point value is called a squeezed state. Such states are by now routinely generated in light fields, where the conflicting uncertainties are those of phase and amplitude, allowing interferometric measurements that break the shot-noise limit. The simulations show how squeezed states can be created in a crystal lattice, which compared to light is a much more tangible system.

There is little overlap between the literature on coherent and on squeezed phonons. Therefore this work follows a slightly unconventional structure: Instead of first summing up the existing scientific work on coherent and squeezed phonons, this is discussed separately at the beginning of each of the respective chapters. We begin with a presentation of the model system for the coupled electron-phonon dynamics in a quantum well, which is common to all of the simulations.

1 Phonons in quantum wells

Although this chapter briefly answers the question, What are phonons and quantum wells?, its main purpose is to establish and explain the model system that is the basis for the dynamical calculations. More detailed information about phonons and quantum wells can be found, e.g., in the textbooks by Madelung [41] and Bastard [6].

1.1 Phonons

A solid is made up of atomic nuclei and their electrons held together by Coulomb forces. Because the nuclei have a much larger mass, we can assume that the electrons can adapt very fast to any change of position of the nuclei and in this way provide an effective potential for the motion of the nuclei. When this potential, which depends simultaneously on the positions of all nuclei, is approximated up to second order around the configuration of lowest energy, we end up with a system of coupled harmonic oscillators. This system can be diagonalized into uncoupled harmonic oscillators; these so-called normal modes describe collective motions of the nuclei. The excitation quantum of one of these harmonic oscillators is called a phonon. For example, a sound wave traveling through the solid in this picture corresponds to a coherent excitation of phonons and its dynamical evolution in time.

In a crystal the nuclei are neatly arranged in a periodic lattice. This allows for a very convenient labeling of the normal modes by two quantum numbers, the branch index α and the wave vector $\boldsymbol{q}$. In a three-dimensional lattice with n atoms per unit cell there are $3n$ different branch indices. $\boldsymbol{q}$ is a vector from the first Brillouin zone; its possible values are discrete and defined by the periodic boundary conditions. The number of possible values is equal to the number of unit cells N in the system volume V, so if this volume is sufficiently large, the range of possible values is quasi-continuous.

The branches can be divided into acoustic and optical branches by their behavior in the long-wavelength limit, i.e., for small q. There are three acoustic branches in which all nuclei in a unit cell move collectively in the same direction and therefore the mode frequency $\omega_{\alpha,\boldsymbol{q}}$ goes to zero for small q. All other branches are called optical; here the nuclei within one unit cell move against each other and $\omega_{\alpha,q=0}$ does not vanish. The branches can further be classified as longitudinal or transverse by whether the displacement of the nuclei is parallel or perpendicular to the wave vector. However, this separation holds strictly only at high-symmetry points of the Brillouin zone.

The ladder operators of the harmonic oscillator of the mode $(\alpha, \boldsymbol{q})$, or, equivalently, the creation and annihilation operators for a phonon of that mode, are $b^\dagger_{\alpha,\boldsymbol{q}}$ and $b_{\alpha,\boldsymbol{q}}$. The Hamiltonian of the phonon system can then be written as

$$H_{\mathrm{ph}} = \sum_{\alpha,\boldsymbol{q}} \hbar\omega_{\alpha,\boldsymbol{q}}\, b^\dagger_{\alpha,\boldsymbol{q}} b_{\alpha,\boldsymbol{q}}. \tag{1.1}$$

In this work, we will be concerned with long-wavelength optical phonons in a gallium arsenide (GaAs) crystal. Since there is one gallium and one arsenic atom per primitive unit cell, we have three optical branches. A simplified model of the GaAs phonon mode structure will be used: We neglect effects of the anisotropy of the crystal and assume that there is one exactly longitudinal and two exactly transverse modes. This implies that the two transverse optical (TO) modes are degenerate, which is true for small q [57]. In addition we will assume a flat optical phonon dispersion, $\omega_{\alpha,\boldsymbol{q}} \equiv \omega_\alpha$, also a good approximation in the region of the Brillouin zone center.

By the mode eigenvectors the phonon operators are connected to the position and momentum of the lattice nuclei. The optical modes describe a relative displacement of the gallium and arsenide sublattices; the corresponding operator of the displacement field $\boldsymbol{u}(\boldsymbol{r})$ in terms of the phonon operators is

$$\hat{\boldsymbol{u}}(\boldsymbol{r}) = \frac{1}{\sqrt{N}} \sum_{\alpha,\boldsymbol{q}} \sqrt{\frac{\hbar}{2M\omega_\alpha}}\, \boldsymbol{e}_{\alpha,\boldsymbol{q}} \left(\mathrm{e}^{\mathrm{i}\boldsymbol{q}\cdot\boldsymbol{r}} b_{\alpha,\boldsymbol{q}} + \mathrm{e}^{-\mathrm{i}\boldsymbol{q}\cdot\boldsymbol{r}} b^\dagger_{\alpha,\boldsymbol{q}} \right). \tag{1.2}$$

Here α counts over the optical branches only. The polarization vector $\boldsymbol{e}_{\alpha,\boldsymbol{q}}$ for the longitudinal optical (LO) branch is $\boldsymbol{e}_{\mathrm{LO},\boldsymbol{q}} = \frac{\boldsymbol{q}}{q}$. For the two TO branches it can be chosen arbitrarily as long as all three vectors form an orthonormal set. Because we are looking at a relative motion, M is the reduced mass of the two lattice atoms: $M^{-1} = M_{\mathrm{Ga}}^{-1} + M_{\mathrm{As}}^{-1}$.

The operator $\hat{\boldsymbol{p}}(\boldsymbol{r})$ of the momentum corresponding to the relative displacement is

$$\hat{\boldsymbol{p}}(\boldsymbol{r}) = \frac{-\mathrm{i}}{\sqrt{N}} \sum_{\alpha,\boldsymbol{q}} \sqrt{\frac{\hbar M\omega_\alpha}{2}}\, \boldsymbol{e}_{\alpha,\boldsymbol{q}} \left(\mathrm{e}^{\mathrm{i}\boldsymbol{q}\cdot\boldsymbol{r}} b_{\alpha,\boldsymbol{q}} - \mathrm{e}^{-\mathrm{i}\boldsymbol{q}\cdot\boldsymbol{r}} b^\dagger_{\alpha,\boldsymbol{q}} \right). \tag{1.3}$$

Strictly speaking, $\hat{\boldsymbol{u}}(\boldsymbol{r})$ and $\hat{\boldsymbol{p}}(\boldsymbol{r})$ are not continuous fields but only defined if $\boldsymbol{r}$ is a lattice vector. However, at least for long-wavelength phonons and accordingly slowly varying displacements it seems natural to interpolate between lattice sites.

1.1.1 Coherent and incoherent phonons

The dynamics of the lattice displacement can be observed by, e.g., a time-resolved measurement of small changes in the reflectivity of the crystal [11]. This is usually done in a pump-probe setup where we do not have a one-shot measurement but the mean value of a large amount of measurements is recorded. The mean value corresponds to the quantum mechanical expectation value $\boldsymbol{u} = \langle \hat{\boldsymbol{u}} \rangle$.

Lattice excitations which lead to a non-vanishing lattice displacement $\boldsymbol{u}$ are called coherent phonons. In most cases this means that the displacement is oscillating in time. Because $\boldsymbol{u}$ is fully determined by $\langle b_{\alpha,\boldsymbol{q}} \rangle$, that quantity is called the coherent phonon amplitude.

The number of phonons in one mode, $\langle b^\dagger_{\alpha,\boldsymbol{q}} b_{\alpha,\boldsymbol{q}} \rangle$, can be partitioned in the following way:

$$\langle b^\dagger_{\alpha,\boldsymbol{q}} b_{\alpha,\boldsymbol{q}} \rangle = \langle b^\dagger_{\alpha,\boldsymbol{q}} \rangle \langle b_{\alpha,\boldsymbol{q}} \rangle + \delta \langle b^\dagger_{\alpha,\boldsymbol{q}} b_{\alpha,\boldsymbol{q}} \rangle, \tag{1.4}$$

where the first addend is called the number of coherent phonons and the remaining part of the sum is defined as the number of incoherent phonons [35]. While coherent phonons determine the lattice displacement, incoherent phonons increase its uncertainty, i.e., the variance $(\Delta u_i)^2 = \left\langle (u_i - \langle u_i \rangle)^2 \right\rangle$ with $i = \mathrm{x}, \mathrm{y}, \mathrm{z}$.

1.1.2 Confined phonon modes

We have so far considered phonons in a bulk crystal. The situation in a quantum well can be quite different; as we will see in the next section, the layered structure of a quantum well gives rise to confined electron states, and in the same way a confinement of phonons can be expected. In our case, however, we do not need to explicitly include phonon confinement: The phonons will be generated almost exclusively within the well, and as we have assumed a constant dispersion relation, their group velocity vanishes and they can neither travel out of the well nor be reflected at the interfaces. In this sense, phonon confinement is already included.

Additional effects of the confinement become important in very thin quantum wells. Experiments on a GaAs/AlAs quantum well have shown a shift in the phonon energies and the emergence of new modes [19]. However, when the quantum well width exceeds some 15 monolayers (4.2 nm), these effects become negligible. We will only be dealing with quantum wells considerably wider than this.

1.2 Semiconductor quantum wells

A semiconductor quantum well consists of a thin sheet of a semiconductor material sandwiched between two sheets of another semiconductor whose band gap is larger. The inner sheet is the well and the outer material is called the barrier. Electronic excitations are trapped within the well as long as their excess energy is smaller than the band discontinuity to the barrier. The confinement leads to a quantization of energy. The electronic properties of the quantum well can be tailored in a wide range by changing, e.g., the composition of materials or their doping, the spacing of well and barrier, or the growth direction.

A very common combination of materials is GaAs as the well material and AlAs as the barrier. Those materials have the same crystallographic structure (zincblende type) and a very similar lattice constant. Throughout this work material parameters for a GaAs/AlAs quantum well grown along the [001] direction will be used. Concrete values for all material parameters used are given in the appendix (section 5.1).

1.2.1 Envelope function description

The wave functions of energy eigenstates in a quantum well close to a band extremum can be approximated by the Bloch function $u_0(\boldsymbol{r})$ at that extremum multiplied by the so-called envelope function $\phi_n(z)$, which only depends on the coordinate in the confinement direction, together with a plane-wave factor taking care of the in-plane directions $\boldsymbol{r}_\parallel$ [6]:

$$\psi_{n,\boldsymbol{k}}(\boldsymbol{r}) = \frac{1}{\sqrt{A}} \mathrm{e}^{\mathrm{i}\boldsymbol{k}\cdot\boldsymbol{r}_\parallel} \phi_n(z)\, u_0(\boldsymbol{r}) \tag{1.5}$$

Here A is the system area in in-plane direction and $\boldsymbol{k}$ is a two-dimensional wave vector. The Bloch function $u_0(\boldsymbol{r})$ is used within both well and barrier, implying that the bulk eigenstates of well and barrier material at the chosen extremum are sufficiently similar.

The envelope function $\phi_n(z)$ and its energy $\varepsilon_{n,0}$ are defined by the one-dimensional Schrö-

dinger-like equation

$$\left[-\frac{\hbar^2}{2}\frac{\mathrm{d}}{\mathrm{d}z}\frac{1}{m(z)}\frac{\mathrm{d}}{\mathrm{d}z}+V(z)\right]\phi_n(z)=\varepsilon_{n,0}\phi_n(z). \tag{1.6}$$

$m(z)$ is a piecewise constant function that gives the effective electron mass, depending only on whether z is within the well or in the barrier. In the same way the potential $V(z)$ is defined as the band-edge energy in the respective material. If an external electric field is applied to the quantum well, its potential is included into $V(z)$.

The energy of the full state (1.5) is then given by $\varepsilon_{n,\boldsymbol{k}}=\varepsilon_{n,0}+\frac{\hbar^2k^2}{2m}$. The in-plane mass m can be set equal to the effective electron mass of the well material as long as the electron density $|\phi_n(z)|^2$ is small within the barrier. The index n, which labels the different solutions to (1.6), is called the subband index. Each subband has a constant density of states above its minimum energy because of the two-dimensional parabolic dispersion. The density of states of several subbands combined consequently exhibits a step-like energy dependence.

As we are interested in states close to the band gap, we consider envelope states resulting from the lowest conduction band and the highest valence band at the Γ point. We will only consider heavy hole states, as a much more complicated model would be needed to include light holes and their band mixing with the heavy hole states. We will later see that this reduced model of the electronic system is sufficient when the focus lies on the optically-induced lattice dynamics.

1.2.2 Quantum confined Stark effect

An easy way to influence the subband level energies and their wave functions is to apply an external electric field in growth direction. The additional electric potential produces a tilt in the potential $V(z)$. This is demonstrated in figure 1.1, which shows the quantum well potential and the subband energies and envelope functions with and without an external electric field. The data have been produced by numerically solving (1.6) with quantum well parameters as detailed in section 5.1.2(A).

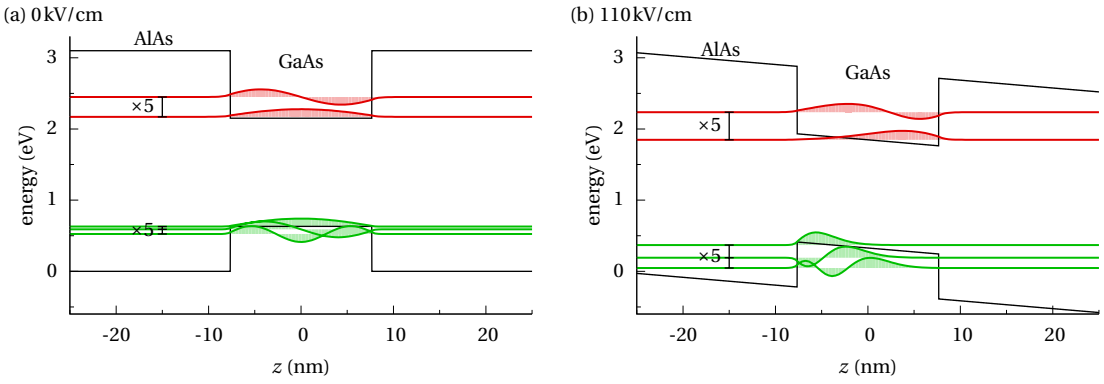

Figure 1.1: Subband structure (a) without and (b) with electric field. Shown are the quantum well potential (black lines, zero point is shifted) and the envelope functions (colored lines). The baselines of the envelope functions indicate their energy. For better visibility, the energy relative to the lowest subband is exaggerated by a factor of five; in other words, the well is much deeper than it seems here. [parameter set A]

Two electron and three heavy-hole subbands are included in the calculation. The energy splitting between hole subbands is smaller than that of the electron subbands because the effective mass of the holes is larger.

The changes due to the electric field are subsumed under the name quantum confined Stark effect (QCSE). We see that the splitting between the subband levels is increased and the shape of the envelope functions is changed. Because the quantum well potential is no longer symmetric, the parity symmetry of the envelope functions is broken. The hole states in particular now have a strong bias towards the left-hand side of the well. This means that the charge separation after excitation of electron-hole pairs is increased, which will prove to be important for the coupling between charge carriers and phonons.

1.3 The full model Hamiltonian

With the theoretical descriptions of the phononic subsystem and the electronic single-particle states in place, we are now in the position to set up a model that can realistically describe the coupled electron-phonon dynamics in quantum wells driven by short laser pulses. A few aspects are still missing, which will now be introduced: Coulomb interaction between charge carriers strongly influences the electronic states and consequently the light absorption characteristics; the coupling to the light field itself is needed; and most importantly, the coupling between electrons and phonons has to be included.

1.3.1 Electronic subsystem and Coulomb interaction

The electronic system will also be described in the language of second quantization. We make use of the electron-hole picture: $c^\dagger_{i,\boldsymbol{k}}$ creates an electron in the conduction band state $\psi^{\mathrm{c}}_{i,\boldsymbol{k}}$ (subband i, in-plane wave vector $\boldsymbol{k}$), and the hole creation operator $d^\dagger_{j,\boldsymbol{k}}$ annihilates a valence band electron in the state $\psi^{\mathrm{v}}_{j,-\boldsymbol{k}}$. The free-particle Hamiltonian can then be written as

$$H_{\mathrm{el}} = \sum_{i,\boldsymbol{k}} \varepsilon^{\mathrm{e}}_{i,\boldsymbol{k}} c^\dagger_{i,\boldsymbol{k}} c_{i,\boldsymbol{k}} + \sum_{j,\boldsymbol{k}} \varepsilon^{\mathrm{h}}_{j,\boldsymbol{k}} d^\dagger_{j,\boldsymbol{k}} d_{j,\boldsymbol{k}}. \tag{1.7}$$

The electron energy $\varepsilon^{\mathrm{e}}_{i,\boldsymbol{k}}$ is just the energy of the corresponding conduction band state, while the hole energy is the negative energy of the valence band electron, $\varepsilon^{\mathrm{h}}_{j,\boldsymbol{k}} = -\varepsilon^{\mathrm{v}}_{j,-\boldsymbol{k}}$. In the same way the hole mass m_{h} is defined as minus the effective valence band mass, which itself is negative due to the positive curvature of the valence band.

Although both conduction band and heavy-hole band have a twofold spin degeneracy, the spin index has been left out. For the moment let us assume that the spin index is subsumed into the subband index; in the appropriate places, its effects are stated in the text. A more comprehensive discussion of the spin degree of freedom will be given later on in section 2.2.6.

Because of their charge electrons and holes attract each other while repelling their own species. As a result, electrons and holes can form bound pairs, i.e., excitons. Effects like this have to be

accounted for by including the Coulomb interaction. It is given by [33]

$$\begin{aligned} H_{\mathrm{Cb}} = & \frac{1}{2} \sum_{\substack{i_1 i_2 i_3 i_4 \\ \boldsymbol{k}_1 \boldsymbol{k}_2 \boldsymbol{k}_3}} V_{\boldsymbol{k}_3}^{i_1 i_2 i_3 i_4} \, c^\dagger_{i_1 \boldsymbol{k}_1 + \boldsymbol{k}_3} c^\dagger_{i_2 \boldsymbol{k}_2 - \boldsymbol{k}_3} c_{i_3 \boldsymbol{k}_2} c_{i_4 \boldsymbol{k}_1} \\ & + \frac{1}{2} \sum_{\substack{j_1 j_2 j_3 j_4 \\ \boldsymbol{k}_1 \boldsymbol{k}_2 \boldsymbol{k}_3}} V_{\boldsymbol{k}_3}^{j_4 j_3 j_2 j_1} \, d^\dagger_{j_1 \boldsymbol{k}_1 + \boldsymbol{k}_3} d^\dagger_{j_2 \boldsymbol{k}_2 - \boldsymbol{k}_3} d_{j_3 \boldsymbol{k}_2} d_{j_4 \boldsymbol{k}_1} \\ & - \sum_{\substack{i_1 j_2 j_1 i_2 \\ \boldsymbol{k}_1 \boldsymbol{k}_2 \boldsymbol{k}_3}} V_{\boldsymbol{k}_3}^{i_1 j_2 j_1 i_2} \, c^\dagger_{i_1 \boldsymbol{k}_1 + \boldsymbol{k}_3} d^\dagger_{j_1 \boldsymbol{k}_2 - \boldsymbol{k}_3} d_{j_2 \boldsymbol{k}_2} c_{i_2 \boldsymbol{k}_1}. \end{aligned} \tag{1.8}$$

This definition neglects terms that do not conserve the number of electrons and holes separately, and therefore cannot account for effects like Auger scattering. However, such effects are of no importance for the low-density excitations close to the band gap that we are interested in.

Here and in what follows the i-indices are used for electron subbands, the j-indices for hole subbands, and n-indices if both are possible. In addition, commas between indices are left out as long as their distinctness is obvious. The Coulomb matrix element is then defined as [32]

$$V_{\boldsymbol{k}}^{n_1 n_2 n_3 n_4} = \frac{e^2}{2\varepsilon_0 \varepsilon_\infty A} \frac{1}{k} \iint \phi^*_{n_1}(z) \phi^*_{n_2}(z') \phi_{n_3}(z') \phi_{n_4}(z) \, \mathrm{e}^{-|z-z'|k} \, \mathrm{d}z \, \mathrm{d}z', \tag{1.9}$$

where e is the elementary charge and ε_0 is the electric constant. The high-frequency dielectric constant ε_∞ instead of its static counterpart ε_s has been used here; as soon as phonons are included, the contribution of the lattice to the dielectric constant would otherwise be counted twice. The definition again lacks spin indices. Since the Coulomb interaction does not affect spins, $V_{\boldsymbol{k}}^{n_1 n_2 n_3 n_4}$ vanishes if the spins connected to n_1 and n_4 or those connected to n_2 and n_3 are different.

As a technical aside, the derivation of the Coulomb matrix element involves a substitution of sums over $\boldsymbol{k}$ by an integral. Letting the spacing Δk approach zero is equivalent to assuming an infinitely large system volume. Only by this we obtain the $1/k$-dependence and the singular point at $k = 0$. Some of the singularities thus introduced into the equations of motion will only vanish if we use the same limit there.

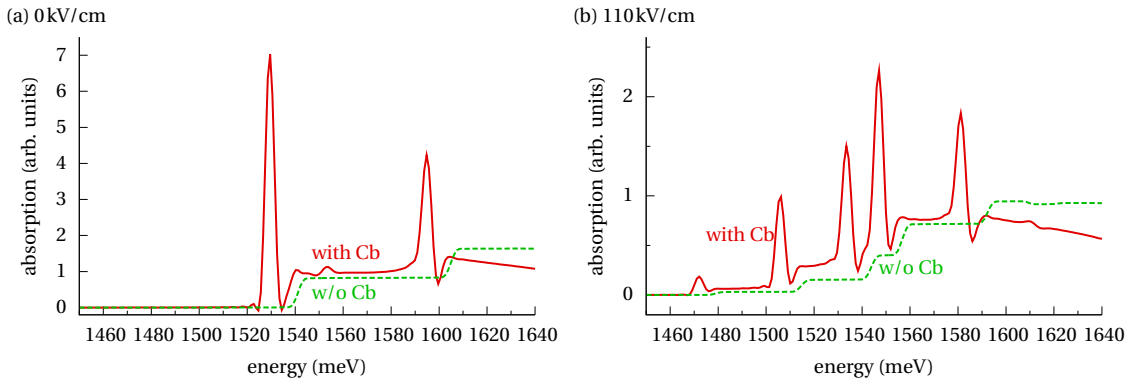

Figure 1.2: Effects of the Coulomb interaction on optical absorption spectra, (a) without and (b) with static electric field. Phonon effects are excluded in this calculation. Between (a) and (b) the vertical axis is rescaled. [parameter set $\mathrm{A_s}$ w/o phonons]

How the Coulomb interaction affects the electronic states can be seen in the optical absorption of the quantum well, as shown in figure 1.2; the underlying calculations will be explained in the chapter 2. Without Coulomb interaction and with no static electric field (left hand side, dashed line), we observe a step-like behavior. This is to be expected because each subband has two free dimensions and hence its density of states is zero below the subband edge and constant above. There are only two steps, resulting from the transitions from the lowest electron to the highest heavy hole subband (e1h1) and from the next respective subbands (e2h2); the transitions e1h2, e2h1 and e2h3 are parity forbidden, and e1h3 has a very small transition probability. With Coulomb interaction (solid line), excitons show up as peaks shortly below the subband edges. A small third peak develops (at about 1552 meV), which belongs to the e1h3 transition. In the case with an electric field (right hand side), the selection rules are lifted and therefore more steps and exciton lines are visible.

1.3.2 Optical driving

In order to calculate optical spectra and to simulate the dynamics after optical pumping, the coupling to laser pulses has to be included into our model. Optical laser pulses affect a semiconductor predominantly by driving electronic interband transitions. Intraband transitions and lattice vibrations can be neglected because their energy is much smaller than the energy of a single photon and such processes therefore are highly off-resonant. Then, the interaction between electrons and the electric field $\boldsymbol{E}(t)$ of the laser, which here is assumed to be spatially homogeneous, is described by the Hamiltonian [33]

$$H_{\mathrm{opt}} = \sum_{i_1 j_1 \boldsymbol{k_1}} \left[-\boldsymbol{E}\cdot\boldsymbol{M}_{i_1 j_1} c^\dagger_{i_1 \boldsymbol{k_1}} d^\dagger_{j_1 -\boldsymbol{k_1}} - \boldsymbol{E}\cdot\boldsymbol{M}^*_{i_1 j_1} d_{j_1 -\boldsymbol{k_1}} c_{i_1 \boldsymbol{k_1}} \right]. \tag{1.10}$$

The spin selection rules, which again are not written out explicitly, require that the sum of electron and hole spin is equal to the spin of a photon, which can be plus or minus one.

The interband dipole matrix element $\boldsymbol{M}_{ij}$ is basically the overlap between electron- and hole envelope functions,

$$\boldsymbol{M}_{ij} = \boldsymbol{M_0} \int \phi^{\mathrm{e}*}_i(z)\phi^{\mathrm{h}}_j(z)\,\mathrm{d}z. \tag{1.11}$$

$\boldsymbol{M_0}$ can in principle be calculated as the dipole matrix element between the bulk electron and hole Bloch functions. However, because the product of the electric field amplitude $\boldsymbol{E}_0$ and $\boldsymbol{M}_0$ enters just as a simple factor in (1.10), we will instead use $\boldsymbol{E}_0 \cdot \boldsymbol{M}_0$ as a parameter that determines the strength of the optical driving.

The electric field of a Gaussian-shaped laser pulse with central frequency ω_0 and a full width at half maximum (FWHM) of τ is modeled as

$$\boldsymbol{E}(t) = \boldsymbol{E}_0\, \mathrm{e}^{-4\ln(2)\, t^2/\tau^2} \left(\mathrm{e}^{-\mathrm{i}\omega_0 t} + \mathrm{e}^{\mathrm{i}\omega_0 t} \right). \tag{1.12}$$

In the numerical calculations the rotating wave approximation is used, i.e., terms in (1.10) that rotate very fast in time are dropped. More precisely, according to the free particle Hamiltonian (1.7), the operator $d_{j-\boldsymbol{k}} c_{i\boldsymbol{k}}$ in the Heisenberg picture rotates as $\exp\left(-\mathrm{i}(\varepsilon^{\mathrm{e}}_{i\boldsymbol{k}} + \varepsilon^{\mathrm{h}}_{j\boldsymbol{k}})\, t/\hbar\right)$. Therefore only the electric field term proportional to $\mathrm{e}^{+\mathrm{i}\omega_0 t}$ is considered in the product with this operator.

The adjoint operator rotates in the opposite direction and is multiplied only with the term proportional to $\mathrm{e}^{-\mathrm{i}\omega_0 t}$.

1.3.3 Electron-phonon coupling

In a semiconductor with partly ionic bonds like GaAs, a displacement of the two sublattices entails a polarization that interacts with the electronic subsystem. This gives rise to a coupling between LO phonons and charge carriers, the so-called Fröhlich interaction. Other types of electron-phonon coupling in these materials are usually much weaker and will not be included. The Fröhlich Hamiltonian for the quantum well system is given by [33]

$$\begin{aligned} H_{\mathrm{Fr}} = & \sum_{\substack{i_1 i_2 \\ \boldsymbol{k}_1 \boldsymbol{k}_2 q_{1z}}} \left[g_{\boldsymbol{q}_1}^{i_1 i_2} c_{i_1 \boldsymbol{k}_2}^\dagger c_{i_2 \boldsymbol{k}_1} b_{\boldsymbol{q}_1} + g_{\boldsymbol{q}_1}^{*\, i_1 i_2} c_{i_2 \boldsymbol{k}_1}^\dagger c_{i_1 \boldsymbol{k}_2} b_{\boldsymbol{q}_1}^\dagger \right] \\ & - \sum_{\substack{j_1 j_2 \\ \boldsymbol{k}_1 \boldsymbol{k}_2 q_{1z}}} \left[g_{\boldsymbol{q}_1}^{j_2 j_1} d_{j_1 \boldsymbol{k}_2}^\dagger d_{j_2 \boldsymbol{k}_1} b_{\boldsymbol{q}_1} + g_{\boldsymbol{q}_1}^{*\, j_2 j_1} d_{j_2 \boldsymbol{k}_1}^\dagger d_{j_1 \boldsymbol{k}_2} b_{\boldsymbol{q}_1}^\dagger \right]. \end{aligned} \tag{1.13}$$

$\boldsymbol{k}_1$ and $\boldsymbol{k}_2$ are in-plane wave vectors, whereas the phonon wave vector $\boldsymbol{q}_1$ is three-dimensional with $\boldsymbol{q}_1 = \boldsymbol{k}_2 - \boldsymbol{k}_1 + q_{1z}\boldsymbol{e}_z$. Phonon operators without a branch index are from here on understood to refer to the LO branch. The Fröhlich coupling matrix element is defined as

$$g_{\boldsymbol{q}}^{n_1 n_2} = -\mathrm{i}\sqrt{\frac{e^2 \hbar \omega_{\mathrm{LO}}}{2\varepsilon_0 V}\left(\frac{1}{\varepsilon_\infty} - \frac{1}{\varepsilon_{\mathrm{s}}}\right)} \cdot \mathscr{F}_{q_z}^{n_1 n_2} \frac{1}{q} \tag{1.14}$$

with the form factor

$$\mathscr{F}_{q_z}^{n_1 n_2} = \int \phi_{n_1}^*(z) \phi_{n_2}(z) \mathrm{e}^{\mathrm{i} q_z z} \, \mathrm{d}z. \tag{1.15}$$

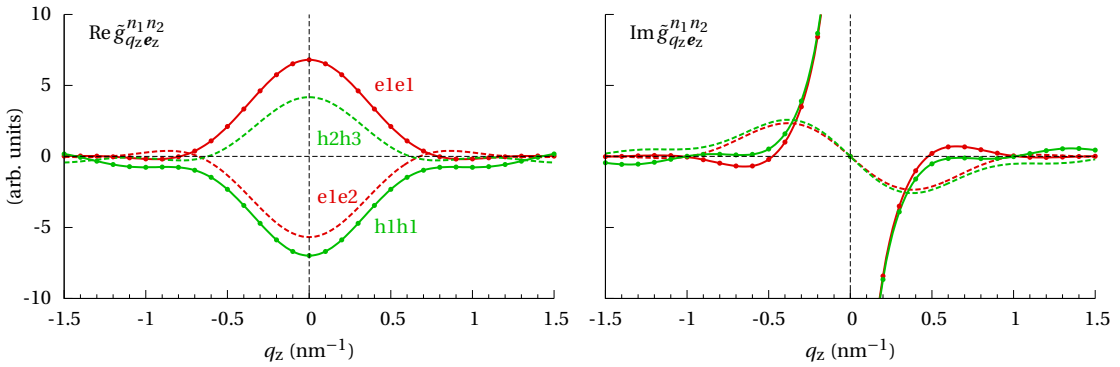

Figure 1.3: q_z-dependence of the Fröhlich matrix element for several subband combinations. Solid (dashed) lines indicate diagonal (off-diagonal) subbands indices, and color differentiates between electron subbands (red) and hole subbands (green). The q_z-discretization used in calculations is shown by little knobs on the solid lines. [parameter set A]

Just as with the Coulomb interaction, we again have a $1/q$-term in the coupling matrix element. This will later prove to be important because we will focus on phonons with very small wave vectors. The behavior of the coupling matrix for the quantum well with electric field

is depicted in figure 1.3. The definition of the LO polarization vector as $\boldsymbol{e}_{\mathrm{LO},\boldsymbol{q}} = \frac{\boldsymbol{q}}{q}$ leads to an inversion for negative q_z that has been reversed by plotting $\tilde{g}_{\boldsymbol{q}}^{n_1 n_2} = \mathrm{sgn}(q_z) g_{\boldsymbol{q}}^{n_1 n_2}$. The singularity is visible in the imaginary part of $\tilde{g}_{\boldsymbol{q}}^{n_1 n_2}$ for diagonal subband indices ($n_1 = n_2$). However, it is the same for electrons and holes, and as long as the system as a whole is uncharged, the divergent contributions from electrons and holes will balance out. For off-diagonal indices and for the real part, the form factor removes the singularity.

We also see that the coupling is loosely confined to relatively small values of $|q_z|$. Therefore only long-wavelength phonons can be excited. In the calculations $q_{\max} = 1.5\,\mathrm{nm}^{-1}$ is taken as an upper bound, which lies at about thirteen percent on the way from the Γ point to the Brillouin zone boundary.

1.3.4 Full Hamiltonian

With this, the model Hamiltonian that will be used throughout this work is complete. In short, it consists of

- the Hamiltonian of non-interacting charge carriers and phonons (LO branch only, as in our model all other branches are uncoupled),

$$H_0 = \sum_{i,\boldsymbol{k}} \varepsilon_{i,\boldsymbol{k}}^{\mathrm{e}} c_{i,\boldsymbol{k}}^{\dagger} c_{i,\boldsymbol{k}} + \sum_{j,\boldsymbol{k}} \varepsilon_{j,\boldsymbol{k}}^{\mathrm{h}} d_{j,\boldsymbol{k}}^{\dagger} d_{j,\boldsymbol{k}} + \sum_{\boldsymbol{q}} \hbar\omega_{\mathrm{LO}}\, b_{\boldsymbol{q}}^{\dagger} b_{\boldsymbol{q}}, \tag{1.16}$$

- the Coulomb interaction H_{Cb} between charge carriers (1.8),
- the interaction with the laser field H_{opt} (1.10),
- and the Fröhlich interaction H_{Fr} coupling the electronic and phononic subsystems (1.13).

The full Hamiltonian can also be found in concise form in the appendix (section 5.2).

2 Driving coherent phonons

2.1 State of the art

There is quite a large body of literature about the excitation of coherent phonons. Except for long-wavelength coherent acoustic phonons, which are simply sound waves, coherent phonons are usually generated by exciting the material with light pulses [15, 43]. Attempts to build an electrically driven device based on stimulated emission, i.e., a phonon laser, have so far not been successful, although recently amplification of coherent acoustic phonons in a GaAs/AlAs superlattice has been achieved [7].

A long-known technique that is still important today in time-resolved spectroscopy is coherent anti-Stokes Raman scattering (CARS). Two laser pulses with their difference frequency matched to a phonon mode are mixed within the material; if additional selection rules are fulfilled, this mode is coherently driven [8, 59]. The excitation can then be detected as an anti-Stokes sideband of a third laser pulse, which gives CARS its name. The excitation process itself without detection is sometimes called coherent Raman excitation. By its nature, in CARS both excitation and detection have limited temporal resolution: the laser pulses cannot be too short because they need to have well-defined energies. Individual oscillations of the lattice therefore cannot be resolved [34].

A better time resolution can be obtained by exciting with a laser pulse shorter than a phonon oscillation period (114 fs for the GaAs LO modes). The laser pulse excites the electronic subsystem and induces changes on a timescale that is almost instantaneous from the viewpoint of the lattice with its much larger inertia. Then the lattice reacts to the changes of its electronic surroundings and will in most cases start to oscillate. The oscillation can be detected by measuring the reflectivity with another weaker laser pulse, the probe pulse; by measuring emitted terahertz radiation; or by time-resolved x-ray diffraction.

Before going into the details of the excitation process, we will briefly discuss the detection of the lattice oscillation. The reflectivity of the material is affected by lattice distortions. In polar crystals, an important contribution to this effect comes from the polarization connected to the distortion, which is imprinted on the reflectivity via the electro-optic effect; it also leads to the emission of terahertz radiation. The small changes in reflectivity can be observed in a pump-probe experiment [16, 37], and in a similar way the terahertz radiation can be detected with an optically-gated antenna [47, 49]. These methods achieve a good time resolution, and they can detect even minute lattice distortions. However, because they are also sensitive to the electronic subsystem, it is difficult to reliably extract the absolute position of the lattice and the phase of its oscillation [36]. X-ray diffraction is better at probing the actual position of the lattice because it is mostly sensitive to the inner electron shells. Lattice oscillations are seen as small changes in the strength of certain weak Bragg reflexes. The downside of this technique is its lower sensitivity: it only works for relatively large oscillation amplitudes, e.g., in the order of 10^{-4} of the lattice constant in a GaAs/AlGaAs superlattice [4]. All of these detection methods

suffer from a rather low spatial resolution and therefore can see long-wavelength phonons only.

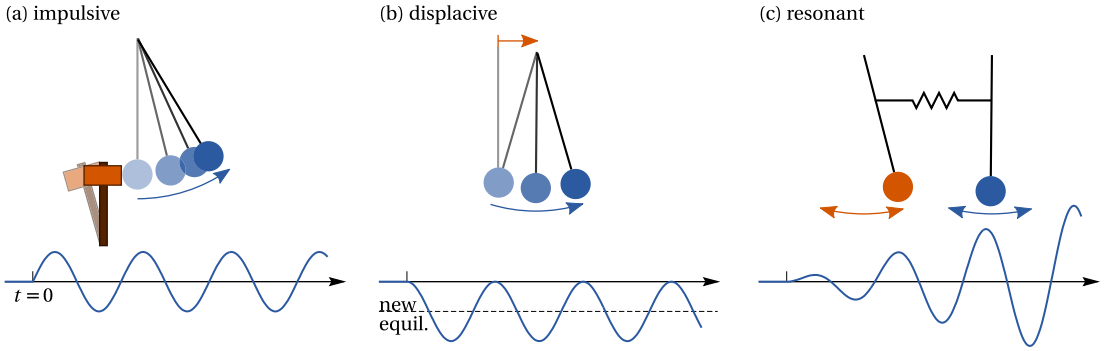

Figure 2.1: Sketches of (a) impulsive, (b) displacive, and (c) resonant excitation of lattice oscillations in a simple pendulum picture. Plotted below is the position of the pendulum as a function of time.

The excitation of coherent phonons by short laser pulses is usually described separately for transparent and opaque excitation conditions. In the transparent case, the photon energy lies within the band gap of the material. During the pulse, electron-hole pairs briefly come into existence only to be coherently destroyed almost immediately afterward. Hence the lattice feels an impulsive force and starts to oscillate, as sketched in figure 2.1(a). The oscillation takes place around the lattice equilibrium position and is sine-like, i.e., at the time $t = 0$ when the pulse hits, it starts with a non-vanishing slope from the equilibrium position. The process can be described by impulsive stimulated Raman scattering (ISRS), which assumes a direct coupling between light field and lattice displacement by the Raman tensor. The ISRS mechanism explains selection rules and the dependence on pump polarization for a wide range of materials [39, 43].

If the material is opaque to the laser pulse, electronic excitations are created which remain after the pulse and shift the equilibrium position of the lattice (figure 2.1(b)). The lattice therefore starts to oscillate around its new equilibrium; the oscillation is cosine-like, i.e., at $t = 0$ it starts with vanishing slope from the old equilibrium position towards the new one. In this picture we neglect any influence of the dynamics of the electronic subsystem after the pulse. The mechanism is called displacive excitation of coherent phonons (DECP) [10, 61]. Only modes that preserve the symmetry of the lattice can be excited via DECP. The DECP mechanism was introduced phenomenologically, but it has also been derived from a microscopic model of a semiconductor, showing that because the laser excitation is essentially homogeneous in space, only optical phonons with wave vector $q = 0$ are excited [35]. In bulk GaAs, the DECP mechanism has to be amended: Coherent optical phonons are in that case generated close to the surface by a fast switch-off of a surface space-charge field. The field results from charged surface states pinning the Fermi level; after optical excitation, electrons and holes are separated by the field and screen it [16, 36, 50].

There is an ongoing discussion on whether DECP should be seen as a special case of the ISRS mechanism, possibly augmented by a second Raman tensor for phonon generation [56]. Experiments show that at least in some cases the ISRS selection rules also apply for opaque excitation conditions [20, 29]. Other measurements have revealed features of coherent phonon generation that support the DECP mechanism [5, 42]. Because both mechanisms are based on rather simple assumptions, they should be seen as explanations that work well in many cases

but do not cover all situations.

So far the dynamics of the electronic subsystem after the laser pulse have played no role in the excitation process. Actually, a particularly strong excitation of coherent phonons can be achieved if the electronic system oscillates with the phonon frequency, as depicted in figure 2.1(c). This resonant phonon generation (RPG) mechanism has been demonstrated in a GaAs/AlGaAs superlattice, which permits Bloch oscillations: The coherent phonon amplitude is resonantly enhanced when the frequency of a Bloch oscillation is tuned to the LO phonon energy with the help of a static electric field [14]. Accompanying theoretical calculations using a microscopic model confirmed the interpretation [22]. The same effect has been observed in a GaAs/AlAs quantum well structure where the driving force is an intraband quantum beat: Two subband levels, whose splitting is tuned via the quantum confined Stark effect (QCSE), are simultaneously excited by a short laser pulse; the resulting quantum beat between those levels carries a polarization that drives the lattice oscillation [30, 47]. The resonant condition can also be met by manufacturing the quantum well to the correct width [48, 49].

The model used in this work accounts for the coherent dynamics of the full coupled electron-phonon system in a quantum well, and therefore encompasses the idealized concepts of impulsive, displacive and resonant excitation of coherent phonons as well as everything in between. It will be used to study coherent phonon generation by each of those mechanisms, with a special emphasis on the very efficient resonant case. Most of the simulations in this chapter therefore make use of quantum well parameters modeled after the experiments of Ref. [30].

Microscopic models similar to the one used in this work have been used to theoretically describe, e.g., the DECP mechanism [35] or the resonant excitation by Bloch oscillations [22], but the dynamics were calculated on a lower level that, for example, excluded the effects of incoherent phonons. Recently, an ab initio approach to simulate coherent phonon excitation has been explored [55]: Time-dependent density functional theory (TDDFT) is shown to reproduce ISRS- and DECP-like processes in bulk silicon. The drawback is that the lattice is treated classically in this theory, so incoherent phonon generation is excluded and non-classical phenomena like squeezed states cannot be described. Finally, there is a purely phenomenological description of coherent phonon generation that lays special emphasis on the modeling of experimental signals: electronic and phononic subsystem are represented by electronic circuits, which are connected to each other and driven by electric pulses [38].

2.2 Quantum kinetic calculations: Correlation expansion

2.2.1 Density matrix formalism with correlation expansion

In this work the density matrix formalism is employed to calculate the dynamics of the model system. This method has successfully been applied to a wide variety of dynamical phenomena in semiconductors [53]. It works by setting up the equations of motion for the expectation values of the relevant observables via

$$\mathrm{i}\hbar\frac{\mathrm{d}}{\mathrm{d}t}\langle A\rangle = \mathrm{i}\hbar\frac{\mathrm{d}}{\mathrm{d}t}\mathrm{Tr}(\rho A) = \mathrm{Tr}(\rho[A,H]) = \langle[A,H]\rangle\,, \tag{2.1}$$

where A is one of the observables, H is the Hamiltonian of the system, and $[A,H]$ is their commutator. In the intermediate steps of (2.1), the density matrix ρ is introduced and the

Heisenberg equation is used for the time derivative of A; obviously, the same result is obtained in the Schrödinger picture where the time derivative of ρ is described by the von Neumann equation.

In many cases, the commutator on the right hand side yields new operators whose time-dependent expectation values have again to be calculated with the help of (2.1). In this way an infinite hierarchy of more and more complicated equations of motion is obtained. In order to calculate the dynamics, the hierarchy is usually truncated by some approximation. For this purpose we will here use correlation expansion, which assumes that correlations between a certain minimum number of particles can be neglected. Other truncation schemes will be discussed in chapter 3, where a method different from correlation expansion is needed.

As an example, we consider the electronic density matrix $\langle c^\dagger_{i\boldsymbol{k}} c_{i'\boldsymbol{k}'}\rangle$, from which quantities like the position-dependent electron density can be derived. Due to the Fröhlich interaction, its equation of motion depends on phonon-assisted matrices of the form $\langle c^\dagger_{i_1\boldsymbol{k}_1} c_{i_2\boldsymbol{k}_2} b_{\boldsymbol{q}}\rangle$. These are expanded into a sum of their factorization and a correlation part, the latter being defined by the expansion:

$$\langle c^\dagger_{i_1\boldsymbol{k}_1} c_{i_2\boldsymbol{k}_2} b_{\boldsymbol{q}}\rangle = \langle c^\dagger_{i_1\boldsymbol{k}_1} c_{i_2\boldsymbol{k}_2}\rangle\langle b_{\boldsymbol{q}}\rangle + \delta\langle c^\dagger_{i_1\boldsymbol{k}_1} c_{i_2\boldsymbol{k}_2} b_{\boldsymbol{q}}\rangle \tag{2.2}$$

In what will be called first-order calculations, this correlation part of phonon-assisted matrices is neglected. Because the equation of motion for the coherent phonon amplitude $\langle b_{\boldsymbol{q}}\rangle$ depends only on the electron and hole densities and $\langle b_{\boldsymbol{q}}\rangle$ itself, we gain a closed system of equations of motion (apart from correlations arising through Coulomb interaction, which we ignore for a moment). In first order, only coherent phonons can be excited because the incoherent phonon populations $\delta\langle b^\dagger_{\boldsymbol{q}} b_{\boldsymbol{q}}\rangle$ are driven by the phonon-assisted correlations $\delta\langle c^\dagger_{i\boldsymbol{k}} c_{i'\boldsymbol{k}'} b_{\boldsymbol{q}}\rangle$ and $\delta\langle d^\dagger_{j\boldsymbol{k}} d_{j'\boldsymbol{k}'} b_{\boldsymbol{q}}\rangle$. If incoherent phonons are to be included, we therefore cannot truncate the hierarchy at this level.

In a second-order calculations, the phonon-assisted correlations are kept. They in turn depend on double-phonon assisted matrices $\langle c^\dagger_{i_1\boldsymbol{k}_1} c_{i_2\boldsymbol{k}_2} b_{\boldsymbol{q}_1} b_{\boldsymbol{q}_2}\rangle$, whose correlation expansion is

$$\begin{aligned}\langle c^\dagger_{i_1\boldsymbol{k}_1} c_{i_2\boldsymbol{k}_2} b_{\boldsymbol{q}_1} b_{\boldsymbol{q}_2}\rangle = {}& \delta\langle c^\dagger_{i_1\boldsymbol{k}_1} c_{i_2\boldsymbol{k}_2} b_{\boldsymbol{q}_1}\rangle\langle b_{\boldsymbol{q}_2}\rangle + \delta\langle c^\dagger_{i_1\boldsymbol{k}_1} c_{i_2\boldsymbol{k}_2} b_{\boldsymbol{q}_2}\rangle\langle b_{\boldsymbol{q}_1}\rangle \\ & + \langle c^\dagger_{i_1\boldsymbol{k}_1} c_{i_2\boldsymbol{k}_2}\rangle\,\delta\langle b_{\boldsymbol{q}_1} b_{\boldsymbol{q}_2}\rangle + \langle c^\dagger_{i_1\boldsymbol{k}_1} c_{i_2\boldsymbol{k}_2}\rangle\langle b_{\boldsymbol{q}_1}\rangle\langle b_{\boldsymbol{q}_2}\rangle \\ & + \delta\langle c^\dagger_{i_1\boldsymbol{k}_1} c_{i_2\boldsymbol{k}_2} b_{\boldsymbol{q}_1} b_{\boldsymbol{q}_2}\rangle.\end{aligned} \tag{2.3}$$

The general rule for correlation expansion is to sum over all factorizations and call what is left the correlation part. If two fermionic operators have to be swapped in order to reach a certain factorization, this term changes its sign. In each factor, fermion operators can only appear in pairs; otherwise, the sign would be ambiguous. In this way the correlation expansion of four-carrier matrices, which also turn up in the equation of motion for phonon-assisted correlations, yields

$$\begin{aligned}\langle c^\dagger_{i_1\boldsymbol{k}_1} c^\dagger_{i_2\boldsymbol{k}_2} c_{i_3\boldsymbol{k}_3} c_{i_4\boldsymbol{k}_4}\rangle = {}& \langle c^\dagger_{i_1\boldsymbol{k}_1} c_{i_4\boldsymbol{k}_4}\rangle\langle c^\dagger_{i_2\boldsymbol{k}_2} c_{i_3\boldsymbol{k}_3}\rangle - \langle c^\dagger_{i_1\boldsymbol{k}_1} c_{i_3\boldsymbol{k}_3}\rangle\langle c^\dagger_{i_2\boldsymbol{k}_2} c_{i_4\boldsymbol{k}_4}\rangle \\ & + \delta\langle c^\dagger_{i_1\boldsymbol{k}_1} c^\dagger_{i_2\boldsymbol{k}_2} c_{i_3\boldsymbol{k}_3} c_{i_4\boldsymbol{k}_4}\rangle.\end{aligned} \tag{2.4}$$

Factorizations with density matrices consisting of two electron creation or two annihilation

operators are not included because they are zero as long as the state of the system has a definite number of electrons (counting both conduction and valence band). This will always be the case as we start with an initial state with this property and the Hamiltonian also conserves the total number of electrons.

We truncate the hierarchy in the second-order calculations by omitting double-phonon assisted correlations and four-carrier correlations.

2.2.2 Dynamical variables and the in-plane homogeneity

Obviously the most important dynamical variable for modeling coherent phonon generation is the coherent phonon amplitude $\langle b_{\boldsymbol{q}} \rangle$. Because the quantum well structure is homogeneous in in-plane direction and the optical excitation is assumed not to break this symmetry, the lattice can only be displaced in z-direction and the displacement field depends on the z-coordinate only, i.e., $\boldsymbol{u}(\boldsymbol{r}) = u(z)\boldsymbol{e}_\mathrm{z}$. Therefore $\langle b_{\boldsymbol{q}} \rangle$ vanishes if $\boldsymbol{q}$ has an in-plane component (see (1.2)), and we can define

$$B_{q_\mathrm{z}} = \left\langle b_{q_\mathrm{z}\boldsymbol{e}_\mathrm{z}} \right\rangle. \tag{2.5}$$

More generally, the translational invariance in in-plane directions gives a simple rule in the k-space representation we are using: Expectation values vanish if their operator breaks conservation of in-plane momentum, i.e., if the sum over in-plane wave vectors at creation operators does not match the sum at annihilation operators. In addition, the system is isotropic in the x-y-plane and hence expectation values have to be invariant under rotation of the frame of reference around the z-axis.

This tells us that electronic variables like $\left\langle c^\dagger_{i\boldsymbol{k}} c_{i'\boldsymbol{k}'} \right\rangle$ always have diagonal in-plane wave vectors ($\boldsymbol{k} = \boldsymbol{k}'$) and depend on the length k only. We define the electron and hole density matrices f^e and f^h and the interband polarization p as

$$f^\mathrm{e}_{ii'\boldsymbol{k}} = \left\langle c^\dagger_{i\boldsymbol{k}} c_{i'\boldsymbol{k}} \right\rangle, \qquad f^\mathrm{h}_{jj'\boldsymbol{k}} = \left\langle d^\dagger_{j-\boldsymbol{k}} d_{j'-\boldsymbol{k}} \right\rangle, \qquad p_{ji\boldsymbol{k}} = \left\langle d_{j-\boldsymbol{k}} c_{i\boldsymbol{k}} \right\rangle. \tag{2.6}$$

The diagonal terms $f^\mathrm{e}_{ii\boldsymbol{k}}$ and $f^\mathrm{h}_{jj\boldsymbol{k}}$ are electron and hole population numbers, whereas the off-diagonal terms are inter-subband coherences. In the same way the phonon-assisted correlations are written as (with $\boldsymbol{q} = \boldsymbol{k}' - \boldsymbol{k} + q_\mathrm{z}\boldsymbol{e}_\mathrm{z}$):

$$\delta s^{\mathrm{e}\,ii'}_{\boldsymbol{k}\boldsymbol{k}'q_\mathrm{z}} = \delta\left\langle c^\dagger_{i\boldsymbol{k}'} c_{i'\boldsymbol{k}} b_{\boldsymbol{q}} \right\rangle = \left\langle c^\dagger_{i\boldsymbol{k}'} c_{i'\boldsymbol{k}} b_{\boldsymbol{q}} \right\rangle - \left\langle c^\dagger_{i\boldsymbol{k}'} c_{i'\boldsymbol{k}} \right\rangle \left\langle b_{\boldsymbol{q}} \right\rangle = \left\langle c^\dagger_{i\boldsymbol{k}'} c_{i'\boldsymbol{k}} b_{\boldsymbol{q}} \right\rangle - \delta_{\boldsymbol{k}\boldsymbol{k}'} f^\mathrm{e}_{ii'\boldsymbol{k}} B_{q_\mathrm{z}} \tag{2.7a}$$

$$\delta s^{\mathrm{h}\,jj'}_{\boldsymbol{k}\boldsymbol{k}'q_\mathrm{z}} = \left\langle d^\dagger_{j-\boldsymbol{k}} d_{j'-\boldsymbol{k}'} b_{\boldsymbol{q}} \right\rangle - \delta_{\boldsymbol{k}\boldsymbol{k}'} f^\mathrm{h}_{jj'\boldsymbol{k}} B_{q_\mathrm{z}} \tag{2.7b}$$

$$\delta s^{\mathrm{he}\,ji}_{\boldsymbol{k}\boldsymbol{k}'q_\mathrm{z}} = \left\langle d_{j-\boldsymbol{k}'} c_{i\boldsymbol{k}} b_{\boldsymbol{q}} \right\rangle - \delta_{\boldsymbol{k}\boldsymbol{k}'} p_{ji\boldsymbol{k}} B_{q_\mathrm{z}} \tag{2.7c}$$

$$\delta s^{\mathrm{hek}\,ji}_{\boldsymbol{k}\boldsymbol{k}'q_\mathrm{z}} = \left\langle d_{j-\boldsymbol{k}} c_{i\boldsymbol{k}'} b^\dagger_{\boldsymbol{q}} \right\rangle - \delta_{\boldsymbol{k}\boldsymbol{k}'} p_{ji\boldsymbol{k}} B^*_{q_\mathrm{z}} \tag{2.7d}$$

Although it has not been made explicit in the definition, it suffices to know the direction of $\boldsymbol{k}'$ relative to $\boldsymbol{k}$ instead of the absolute directions of both vectors.

Finally, we have the two-phonon correlations, which determine the number of incoherent

phonons and the uncertainty of the lattice displacement:

$$\delta n_{\boldsymbol{k}q_z q_z'} = \delta\langle b^\dagger_{\boldsymbol{k}+q_z\boldsymbol{e}_z} b_{\boldsymbol{k}+q_z'\boldsymbol{e}_z}\rangle = \langle b^\dagger_{\boldsymbol{k}+q_z\boldsymbol{e}_z} b_{\boldsymbol{k}+q_z'\boldsymbol{e}_z}\rangle - \delta_{\boldsymbol{k},0} B^*_{q_z} B_{q_z'} \tag{2.8a}$$

$$\delta b_{\boldsymbol{k}q_z q_z'} = \delta\langle b_{\boldsymbol{k}+q_z\boldsymbol{e}_z} b_{-\boldsymbol{k}+q_z'\boldsymbol{e}_z}\rangle = \langle b_{\boldsymbol{k}+q_z\boldsymbol{e}_z} b_{-\boldsymbol{k}+q_z'\boldsymbol{e}_z}\rangle - \delta_{\boldsymbol{k},0} B_{q_z} B_{q_z'} \tag{2.8b}$$

Together the equations of motion of these variables form a closed system within the approximation discussed in the previous section.

2.2.3 Qualitative explanation for driving mechanisms

The excitation of coherent phonons can be understood qualitatively by looking at the equation of motion for the coherent phonon amplitude. It is given by

$$\mathrm{i}\hbar\frac{\mathrm{d}}{\mathrm{d}t}B_{q_z} - \hbar\omega_{\mathrm{LO}} B_{q_z} = 2^* \sum_{i_1 i_2 \boldsymbol{k}_1} g^{*i_1 i_2}_{q_z} f^{\mathrm{e}}_{i_2 i_1 \boldsymbol{k}_1} - 2^* \sum_{j_1 j_2 \boldsymbol{k}_1} g^{*j_2 j_1}_{q_z} f^{\mathrm{h}}_{j_2 j_1 \boldsymbol{k}_1}. \tag{2.9}$$

(Factors of two written as 2^* indicate that they originate from implicit spin sums.) This is the equation of motion of a quantum harmonic oscillator that is driven by the electronic populations and coherences on the right hand side.

If we assume a simple time dependence of the driving terms, we can solve (2.9) analytically. The right hand side of this equation is abbreviated as $D_{q_z}(t)$. Because of the special form of the driving terms, we have $D_{q_z}(t) = -D^*_{-q_z}(t)$. The lattice displacement is determined via (see (1.2))

$$u(z) = \sqrt{\frac{\hbar}{2NM\omega_{\mathrm{LO}}}} \sum_{q_z} \frac{q_z}{|q_z|} \left(\mathrm{e}^{\mathrm{i}q_z z} B_{q_z} + \mathrm{e}^{-\mathrm{i}q_z z} B^*_{q_z}\right). \tag{2.10}$$

Impulsive driving. In the case of impulsive driving the laser energy lies within the band gap and electronic excitations exist for a very brief time only. Let us assume that $D_{q_z}(t) = A_{q_z}\delta(t)$. Then the analytical solution yields

$$B_{q_z}(t) = \frac{A_{q_z}}{\mathrm{i}\hbar}\mathrm{e}^{-\mathrm{i}\omega_{\mathrm{LO}}t}\theta(t) \qquad \text{and} \qquad u(z,t) \propto \sin(\omega_{\mathrm{LO}}t)\,\theta(t), \tag{2.11}$$

where $\theta(t)$ is the Heaviside step function. So we indeed get a sine-like oscillation of the lattice displacement.

Displacive driving. When the semiconductor is excited above the band gap, electrons and holes remain after the pulse. We model this by $D_{q_z}(t) = A_{q_z}\theta(t)$, which leads to

$$B_{q_z}(t) = \frac{A_{q_z}}{\hbar\omega_{\mathrm{LO}}}\left(\mathrm{e}^{-\mathrm{i}\omega_{\mathrm{LO}}t} - 1\right)\theta(t) \qquad \text{and} \qquad u(z,t) \propto \left(\cos(\omega_{\mathrm{LO}}t) - 1\right)\theta(t). \tag{2.12}$$

The lattice oscillation is cosine-like and its center is shifted.

Resonant driving. Resonant driving of the lattice oscillation can be achieved by setting $D_{q_z}(t) = A_{q_z}\mathrm{e}^{-\mathrm{i}\omega_{\mathrm{LO}}t}\theta(t)$. In this case we have

$$B_{q_z}(t) = \frac{A_{q_z}}{\mathrm{i}\hbar}\mathrm{e}^{-\mathrm{i}\omega_{\mathrm{LO}}t}\,t\,\theta(t) \qquad \text{and} \qquad u(z,t) \propto \sin(\omega_{\mathrm{LO}}t)\,t\,\theta(t), \tag{2.13}$$

i.e., the amplitude of the oscillation increases linearly with time.

In fact, the time-dependence of the electronic driving terms of course is more complicated: The optical excitation does not happen instantaneously, the phonons act back on the electronic subsystem, and Coulomb interaction also plays its role. In order to include these effects, the full system of equations of motion has to be solved numerically.

2.2.4 Equations of motion

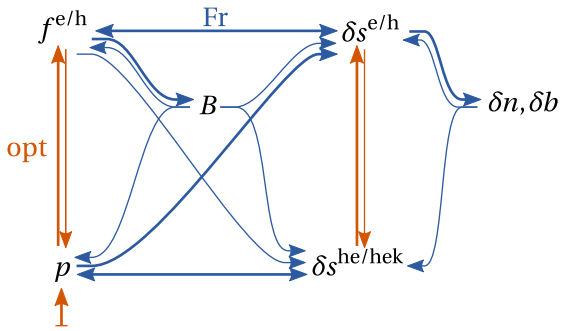

Figure 2.2: Schematic of the equations of motion without Coulomb interaction. Thick lines indicate primary driving terms (minimal order in optical driving field), higher orders are shown as thin lines.

The system of equations of motion is rather large and instead of showing it here in full it is discussed with the help of the schematic in figure 2.2. The equations can be found in the appendix (section 5.3). In the schematic, arrows indicate how the dynamical variables influence each other. Vertical orange arrows represent interactions mediated by the optical driving, blue arrows that start and end horizontally are due to Fröhlich interaction. For clarity, Coulomb interaction and short circuits are not included in this picture. Thick arrows mean that this is a primary influence on the dynamical variable, i.e., it is of the lowest non-vanishing order in the strength of the laser field (this is determined independently for each variable). The thin lines show higher orders, which are less important and for weak excitation conditions can even be ignored completely. The schematic makes a small simplification by equating the roles of δs^{he} and δs^{hek}, which is only warranted if there is an initial (thermal) phonon population.

The initial state for most of the simulations will be the ground state of the system. As the energetically lowest excitation in our model is an optical phonon, which still lies at 36.3 meV, this is a very good approximation at low temperatures. From the ground state, only the polarization can be directly driven by optical excitation, as symbolized by the arrow pointing up to p that starts from nowhere. At the same time, with the help of p electron and hole states are populated. The back-action of $f^{e/h}$ on p controls phase-space filling of the electronic subsystem. The phonon-assisted correlations $\delta s^{e/h}$ and $\delta s^{he/hek}$ are affected by optical driving analogously to their non-assisted counterparts $f^{e/h}$ and p.

As we have already seen, the coherent phonon amplitude B is only driven by f^{e} and f^{h}. In the same way, the only influence on the two-phonon coherences is by the corresponding phonon-assisted correlations δs^{e} and δs^{h}. The phonon-assisted correlations are closely coupled to the purely electronic variables. This describes, for example, the renormalization of electronic energies by polaron formation. To a lesser extent, the phonons act back on the electronic subsystem (directly affected by coherent phonons only) and on the phonon-assisted correlations (both coherent phonons and two-phonon correlations).

2.2.5 Coulomb interaction and mean-field approximation

The Coulomb interaction also drives density matrices with four carrier operators. Those are factorized as already described and four-carrier correlations are omitted. Doing so excludes carrier-carrier scattering and dynamical screening [53]. At low carrier densities, these effects are of little importance. Still included are exciton binding and Coulomb enhancement.

A cruder approximation is obtained by performing the factorization directly in the Coulomb interaction Hamiltonian. This is called a mean-field approximation because electronic operators are substituted by their expectation values. In this sense, the term also applies to the above-mentioned factorization of the density matrices, but it will only be used here if the Hamiltonian itself is approximated. The mean-field approximation reduces the Hamiltonian (1.8) to

$$\begin{aligned} H_{\mathrm{Cb\,MF}} = &\sum_{i_1 i_2 \boldsymbol{k}_1} \mathscr{E}^{\mathrm{Ce}}_{i_1 i_2 \boldsymbol{k}_1} c^\dagger_{i_1 \boldsymbol{k}_1} c_{i_2 \boldsymbol{k}_1} + \sum_{j_1 j_2 \boldsymbol{k}_1} \mathscr{E}^{\mathrm{Ch}}_{j_1 j_2 \boldsymbol{k}_1} d^\dagger_{j_1 -\boldsymbol{k}_1} d_{j_2 -\boldsymbol{k}_1} \\ &+ \sum_{i_1 j_1 \boldsymbol{k}_1} \mathscr{U}^{\mathrm{C}}_{i_1 j_1 \boldsymbol{k}_1} c^\dagger_{i_1 \boldsymbol{k}_1} d^\dagger_{j_1 -\boldsymbol{k}_1} + \sum_{i_1 j_1 \boldsymbol{k}_1} \mathscr{U}^{\mathrm{C}*}_{i_1 j_1 \boldsymbol{k}_1} d_{j_1 -\boldsymbol{k}_1} c_{i_1 \boldsymbol{k}_1}. \end{aligned} \tag{2.14}$$

The variables $\mathscr{E}^{\mathrm{Ce}}$, $\mathscr{E}^{\mathrm{Ch}}$ and $\mathscr{U}^{\mathrm{C}}$ consist of the electronic expectation values f^{e}, f^{h}, and p together with the Coulomb interaction matrix element. Their exact definitions can be found in section 5.3.2.

The mean-field Hamiltonian no longer produces four-carrier density matrices in the equations of motion, so no further factorization of the Coulomb terms is necessary. It also heavily reduces the complexity of the numerical calculations and is used in most of the simulations. In the equations of motion in the appendix (section 5.3), terms that also exist on the mean-field level are labeled H_{Cb} (MF); terms beyond the mean-field Hamiltonian are labeled H_{Cb} (>MF).

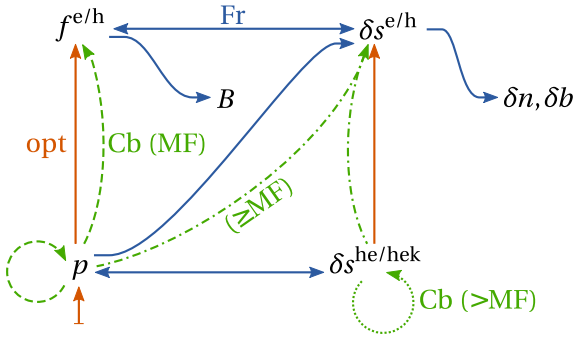

Figure 2.3: Schematic of the equations of motion including Coulomb interaction. Only primary driving terms (minimal order in optical driving field) are shown.

In order to better understand the implications of this approximation, we take a look at the diagram in figure 2.3, which now includes Coulomb interaction (green broken lines) but is restricted to the lowest non-vanishing orders in the driving field. The arrow connecting p with itself and p with $f^{\mathrm{e/h}}$ are the effects of the Coulomb interaction on the electronic subsystem, most prominently the excitonic effects. They are fully included even by the mean-field Hamiltonian. However, some of the corresponding terms for the phonon-assisted correlations go beyond the mean-field approximation. In particular the Coulomb terms renormalizing the energy of $\delta s^{\mathrm{he/hek}}$ vanish if the mean-field approximation is applied to the Hamiltonian. Still, the mean-field approximation often is quite good, as we will later see by a comparison of calculations with and without this approximation (section 2.5.4).

2.2.6 The spin degree of freedom

None of the interactions in our model act on the spins of electrons and holes. The consequences of the fact that electron and hole operators have an additional spin quantum number can therefore be included in quite a simple way, namely by putting factors of two in the appropriate places in the equations of motion. These factors will be designated 2^*, in order to show that they are there because of implicit spin indices.

But how can we determine in which places to insert the factors of two? Let us start with the optical excitation process. We assume that the laser pulse is linearly polarized. This means that electron-hole pairs with the spin configurations e↑h↓ and e↓h↑ are created in equal numbers (the spin directions of electron and hole are opposite because electrons have $\frac{1}{2}$ spins and heavy holes have $\frac{3}{2}$ spins, giving a total spin of $\pm\frac{1}{2} \mp \frac{3}{2} = \mp 1$ as it should be). Therefore we can use a single variable for the polarization:

$$\left\langle d_{j-\boldsymbol{k}\uparrow} c_{i\boldsymbol{k}\downarrow} \right\rangle = \left\langle d_{j-\boldsymbol{k}\downarrow} c_{i\boldsymbol{k}\uparrow} \right\rangle = p_{ji\boldsymbol{k}} \tag{2.15}$$

The polarizations with diagonal spin indices, $\left\langle d_{j-\boldsymbol{k}\uparrow} c_{i\boldsymbol{k}\uparrow} \right\rangle$ and $\left\langle d_{j-\boldsymbol{k}\downarrow} c_{i\boldsymbol{k}\downarrow} \right\rangle$, are never excited and stay zero for all times. In the same way we can write

$$\left\langle c^\dagger_{i\boldsymbol{k}\uparrow} c_{i'\boldsymbol{k}\uparrow} \right\rangle = \left\langle c^\dagger_{i\boldsymbol{k}\downarrow} c_{i'\boldsymbol{k}\downarrow} \right\rangle = f^{\mathrm{e}}_{ii'\boldsymbol{k}}\,, \tag{2.16}$$

while off-diagonal spin combinations vanish. This definition is extended to the phonon-assisted correlations. Consequently, variables like the electron/hole sheet density $\rho^{\mathrm{e/h}}_{\mathrm{int}}$ have to be multiplied by two because both spin up and spin down electrons are to be counted:

$$\rho^{\mathrm{e/h}}_{\mathrm{int}} = 2^* \frac{1}{A} \sum_{n\boldsymbol{k}} f^{\mathrm{e/h}}_{nn\boldsymbol{k}} \tag{2.17}$$

The spin selection rules in the Fröhlich coupling only make sure that no spin flip occurs as a result of the interaction. Because phonons are driven by either spin configuration, this leads to a factor of two in the electronic driving terms in the equations of motion for B, δn and δb.

The situation is more complicated for the Coulomb interaction, although the spin selection rules are similar in the sense that they also forbid spin flips. Carefully tracing the spin indices reveals the general rule that Hartree-like terms (those in which only $V_{k=0}$ can occur) do gain a factor of two while Fock-like terms do not. This can be understood in the following way: Hartree terms can be classically explained by the interaction of a charge carrier with the mean field of all other charge carriers; the mean field of course contains contributions from all carriers regardless of their spin. Fock terms arise only in a quantum treatment (they constitute an exchange interaction), and naturally are sensitive to all quantum numbers including spin. For example, one of the Coulomb interaction terms that enters as a factor in many of the equations of motion (see section 5.3) is given by

$$\mathscr{E}^{\mathrm{Ce}}_{ii'\boldsymbol{k}} = 2^* \sum_{i_1 i_2} V_0^{i i_1 i_2 i'} \sum_{\boldsymbol{k_1}} f^{\mathrm{e}}_{i_1 i_2 \boldsymbol{k_1}} - 2^* \sum_{j_1 j_2} V_0^{i j_2 j_1 i'} \sum_{\boldsymbol{k_1}} f^{\mathrm{h}}_{j_1 j_2 \boldsymbol{k_1}} - \sum_{i_1 i_2 \boldsymbol{k_1}} V^{i i_1 i' i_2}_{\boldsymbol{k_1}} f^{\mathrm{e}}_{i_1 i_2 \boldsymbol{k}+\boldsymbol{k_1}}\,, \tag{2.18}$$

where the first two addends are Hartree terms and the last is a Fock term.

2.2.7 Decoherence processes: Spin relaxation and phonon decay

This simple treatment of the spin degree of freedom assumes that no spin relaxation takes place. Spin relaxation times in GaAs quantum wells are generally large enough to justify this assumption: Heavy hole relaxation times are as short as 4 ps and increase to 1 ns for holes close to the zone center; electron spins relax on a time of about 100 ps and above [23]. In the calculations shown in this work, the maximum simulation time is in the range of 1 ps or shorter.

Another process that destroys the coherence of the optically excited state is phonon decay. Due to lattice anharmonicities, the phonon modes are not fully decoupled and a LO phonon in the zone center can, for example, decay into a pair of one transverse acoustic (TA) and another LO phonon at the zone boundary. The LO decay time in GaAs at low temperatures is about 9 ps [59], which is also large enough to neglect this process. Indeed, including a phenomenological decay with this time constant into the calculations produced differences that were barely noticeable.

2.2.8 Singularity in the Coulomb coupling matrix

The Coulomb coupling matrix element $V_{\boldsymbol{k}}^{n_1 n_2 n_3 n_4}$ contains a factor $1/k$ and therefore has a singularity at $k = 0$ (see (1.9)). For non-diagonal subband indices, i.e., if $n_1 \neq n_4$ or $n_2 \neq n_3$, the singularity is reduced to a removable discontinuity because the integral over the wave functions goes to zero.

For diagonal indices, an infinite discontinuity remains. It is lifted in the equations of motion in one of two ways: In Hartree terms, where $V_{\boldsymbol{k}=0}$ enters, there always is another infinite discontinuity with the opposite sign. For example, the singularities of the first two addends in (2.18) exactly cancel each other because of the charge neutrality condition $\rho^{\mathrm{e}}_{\mathrm{int}} = \rho^{\mathrm{h}}_{\mathrm{int}}$, or

$$\sum_{i\boldsymbol{k}} f^{\mathrm{e}}_{ii\boldsymbol{k}} = \sum_{j\boldsymbol{k}} f^{\mathrm{h}}_{jj\boldsymbol{k}}. \tag{2.19}$$

In Fock terms, the singularity can only be dealt with by substituting the sum over $\boldsymbol{k}$ by an integral. The two-dimensional integral is well defined in spite of the singularity. As was already mentioned, this becomes necessary because a similar substitution of a sum by an integral has been made in the derivation of the Coulomb matrix element.

2.2.9 Singularity in the Fröhlich coupling matrix

The Fröhlich coupling matrix element $g_{\boldsymbol{q}}^{n_1 n_2}$ also has a singularity at $q = 0$. In most cases, it cancels itself in the equations of motion because of charge neutrality just as the Coulomb singularity does.

However, in the second-order calculations this does not hold true in all cases. It turns out that correlation expansion makes an approximation that prevents the removal of the singularity. This will be discussed in more detail in the next chapter (section 3.3.1), because it also necessitates the use of a truncation scheme other than correlation expansion for the calculation of the lattice uncertainties. In the calculations in this chapter, the singularity is removed by canceling the relevant terms in the equations of motion before making the correlation expansion approximation. However, this is only possible at the exact point of the singularity ($q = 0$).

This concludes our discussion of the quantum kinetic calculations. We will now turn to simulation results obtained by numerically solving the equations of motion.

2.3 Absorption spectra and the quantum confined Stark effect

In experiments, the electronic states and their energies are not as directly accessible as in the theoretical model. One of the most commonly used methods to obtain information about these is to measure the spectrally-resolved absorption. Peaks in the absorption spectrum, for example, correspond to transitions between two energy levels.

In our simulations, the linear absorption spectrum can be derived by calculating the time-dependent polarization $P(t)$ induced by a short and weak laser pulse. From the Fourier transforms of the polarization, $P(\omega)$, and of the electric field of the laser pulse, $E(\omega)$, follows the electric susceptibility

$$\chi(\omega) = \frac{P(\omega)}{\varepsilon_0 E(\omega)}. \tag{2.20}$$

The absorption coefficient α is approximately proportional to the imaginary part of χ if the spectral range considered is small and absorption is not too strong [18]. All absorption spectra in this work therefore show $\mathrm{Im}\,\chi(\omega)$.

The macroscopic polarization is determined by the polarization density matrix p_{jik} via

$$\boldsymbol{P} = 2\,\mathrm{Re}\sum_{ijk} \boldsymbol{M}^*_{ij} p_{jik}, \tag{2.21}$$

where $\boldsymbol{M}^*_{ij}$ is the interband dipole matrix element. Here only interband contributions are considered, as intraband terms oscillate much slower than optical frequencies and hence cannot influence the optical spectrum. As $\boldsymbol{P}$ in this model always has the direction of the bulk dipole term $\boldsymbol{M_0}$, its vector properties are discarded.

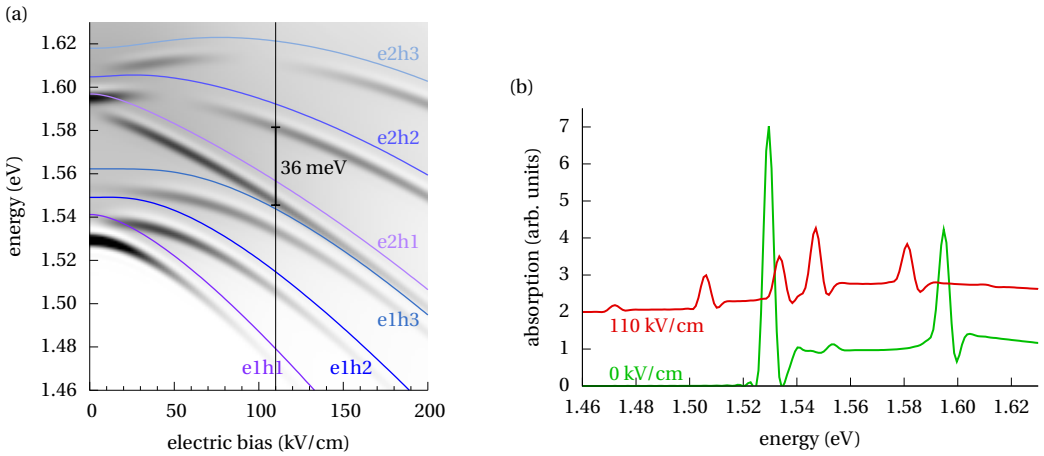

Figure 2.4: Absorption spectra for different values of the electric bias field. In (a), each vertical cut corresponds to an absorption spectrum for a fixed field strength, color-coded with black meaning strong absorption. The colored lines show transition energies between subband levels. In (b) two such vertical cuts are shown; the red line is shifted upwards by two units. [parameter set A_s w/o phonons]

Figure 2.4 shows absorption spectra calculated in this way. Phonons are not included in these calculations; including them would only slightly shift the spectra to lower energies due to polaron formation. In the left part, absorption is plotted as a function of photon energy

and electric bias, with darker shades meaning stronger absorption. Excitons are visible as dark lines, bent because of the energy shift introduced by the bias field. The strength of the lines also varies in a wide range, a consequence of changes in the wave functions that enter into the transition matrix elements. Both effects are subsumed under the name quantum confined Stark effect (QCSE). The exciton lines lie a bit below the transition energies between subband edges, which are plotted as colored lines; the energy difference is the exciton binding energy. Transitions involving the continuum part of the subbands are visible as a blurry background at higher energies. The parameters of our model have been chosen to reflect the properties of the quantum well structure used in Ref. [30]; indeed the simulated spectral map agrees quite well with the spectral photo-current measurements, except for the transitions involving light holes, which are missing in our model.

In the right part of the figure the absorption spectrum for two special values of the electric bias is shown. The exciton energies are visible as sharp peaks. Because the polarization does not decay in these calculations, the line width is not a feature of the model but only depends on the simulation time $t_{\max}$. With no electric bias, there are only two very distinct peaks resulting from the e1h1 and the e2h2 transitions. The e1h3 transition is very weak, all other transitions are parity forbidden. At higher electric fields, the other transitions become active, too. We take a closer look at the conditions at 110 kV/cm, which is indicated by a vertical line in part (a) of the figure and also depicted in part (b). Here the splitting between e2h1 and e2h2 is approximately 36 meV. If both transitions are simultaneously driven by a coherent laser pulse overlapping both energies, a quantum beat between is excited whose frequency coincides with the LO phonon frequency. This is the condition necessary for resonant coherent phonon generation. We will come to that presently, but first discuss non-resonant driving conditions.

2.4 Non-resonant coherent phonon generation

2.4.1 Impulsive driving

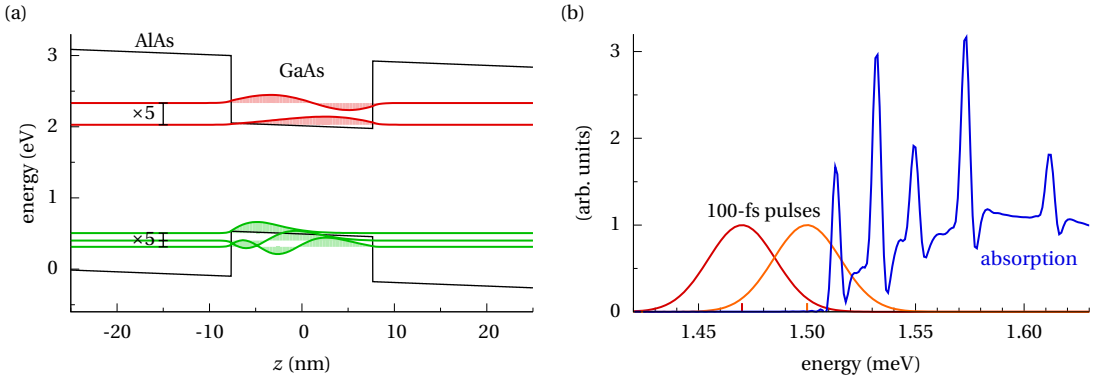

Figure 2.5: (a) Subband structure at $E_s = 50$ kV/cm and (b) corresponding absorption spectrum. The two Gaussians in (b) are the spectra of pulses with a FWHM of 100 fs centered at different energies. [parameter set A_s w/o phonons]

For the discussion of non-resonant driving we set the electric bias field to $E_s = 50$ kV/cm. The resulting subband structure and the absorption spectrum is shown in figure 2.5. The lowest

exciton line lies at about 1.51 eV. We begin with an excitation below the band gap with a Gaussian laser pulse centered at 1.47 eV and with a FWHM of 100 fs. Its spectrum, i.e., the modulus of the Fourier transform of the electric field of the laser pulse, is also shown in part (b) of the figure (the left pulse). There is only negligible overlap of the laser spectrum with the absorption lines.

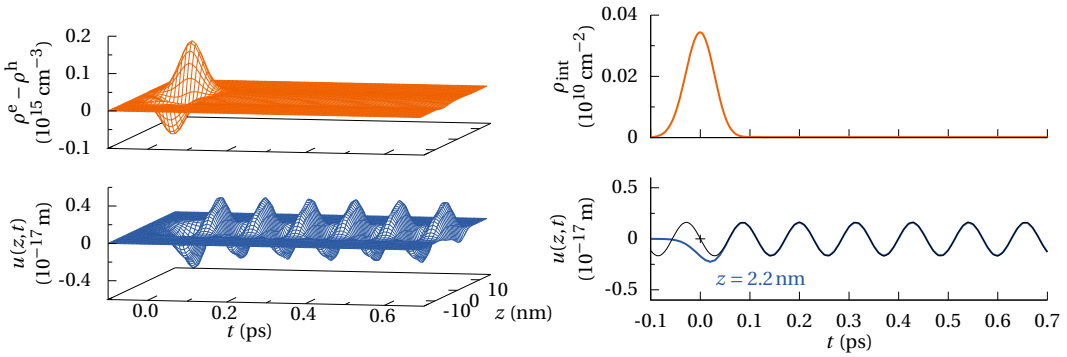

Figure 2.6: Impulsive excitation dynamics (1.47 eV photon energy, bias 50 kV/cm). The upper parts show the carrier density: the difference between electron and hole densities (left) and the integrated electron or hole density (right). In the lower part, the lattice displacement field is plotted as a function of position (left) and for a fixed position (right). The thin black line in the lower right diagram is a fit. [parameter set A]

Figure 2.6 shows the dynamics induced by this laser pulse, which will now be discussed in some detail. The vanishing spectral overlap between pulse and electronic states means that electron-hole pairs can only be excited for a short time during the pulse. This is demonstrated in the upper right part of the figure, which shows the sheet density of electron-hole pairs. At $t = 0$, where the pulse amplitude reaches its peak, the carrier density is also maximal. Almost all electron-hole pairs are gone after the pulse.

For driving lattice oscillations, more important than the density of electrons and holes is their spatial separation. When they are not separated, there is no polarization that the lattice can attempt to compensate; consequently, no coherent phonons are generated. The charge separation is achieved by the electric bias. Due to this bias, electrons generally tend towards larger z-values, where they experience a smaller potential, whereas holes are pushed towards smaller values of z. This is especially true for the lowest states, as seen in figure 2.5 (a). The difference between position-dependent electron and hole density is shown in the upper left part of figure 2.6. The densities are calculated via

$$\rho^{\mathrm{e/h}}(z) = \frac{2^*}{A} \sum_{nn'\boldsymbol{k}} \phi_n^{\mathrm{e/h}*}(z)\, \phi_{n'}^{\mathrm{e/h}}(z)\, f_{nn'\boldsymbol{k}}^{\mathrm{e/h}}. \tag{2.22}$$

Obviously charges are separated during the pulse, and after the pulse the polarization vanishes again. We also see that the charges are confined to the quantum well as they should be.

The short-lived polarization acts as an impulsive force on the lattice, which starts to oscillate. This is visible in the lattice displacement plotted in the lower part of figure 2.6, position-resolved on the left side, and for a maximum-amplitude position on the right hand side. Just like the carrier densities, the lattice displacement stays within the quantum well: the driving charges exist inside the well only, and due to the vanishing group velocity of the LO phonons the phonon

wave packet neither moves nor spreads. The absolute value of the lattice displacement is tiny, but this is to be expected; details will be discussed in the section on resonant coherent phonon generation (section 2.5).

The oscillation of the lattice can very well be fitted with a sine-like function (free parameters: amplitude, frequency, phase, and central value). This is shown in the lower right part of the figure, where the fitted curve is the thin black line. Only the interval from 0.1 ps to 0.7 ps has been used for the fit in order to exclude the dynamics before and during the pulse. Not only does the sine function match lattice oscillation very well, we also obtain a period that is almost exactly equal to the phonon period $T_{\mathrm{LO}} = 114\,\mathrm{fs}$, the phase shift is only $-1°$, and the oscillation is perfectly centered around the equilibrium position $z = 0$. So the generated lattice oscillation is very close to what the pendulum model (figure 2.1) and the simple analysis in section 2.2.3 suggest for impulsive driving.

2.4.2 Displacive driving

Displacive excitation conditions can only be realized imperfectly for this quantum well. Ideally, charge carriers should be rapidly excited without any ongoing dynamics after the excitation. As was already mentioned, exciting more than one exciton line at the same time leads to a beating between the different energy levels. Hence for purely displacive driving, only a single exciton line should be excited, preferably the lowest one so that relaxation processes are excluded. This can easily be done at zero electric field, where only two energetically well-separated optical transitions exist (see figure 2.4). However, in this case there is almost no charge separation, and accordingly the lattice is not affected at all. Therefore the electric bias is again set to 50 kV/cm. Now the different transitions lie close to each other; a 100-fs pulse cannot selectively only drive the lowest transition, as shown in figure 2.5 (b). We set the laser central energy to 1.50 eV, which is slightly below the lowest transition energy and keeps the excitation of the second-lowest transition e1h2 reasonably small. In principle, the spectral width of the laser pulse could be reduced in order to better focus on a single transition. This would obviously require increasing the temporal width of the pulse, which even now is not much shorter than the LO phonon period of 114 fs. Yet the longer the pulse compared to the phonon period, the smaller is the lattice oscillation because the lattice can follow the electronic dynamics adiabatically.

These considerations of course also apply to experiments, and what looks like displacive driving in an experiment will often involve some electronic dynamics after the pulse. But as long as the frequency of the electronic dynamics does not coincide with a preferred lattice frequency, it has no considerable effect on the amplitude of the lattice oscillations, as we will now see.

The dynamics under the excitation conditions just discussed is depicted in figure 2.7. The number of electron-hole pairs (upper right) goes slightly down after reaching its peak. The break-down into the different subband contributions reveals that this is due to the second-lowest hole subband; the laser energy falls short of the e1h2 transition energy and so the subband population peaks during the pulse, leaving behind only a small residual population. The subband populations also oscillate weakly due to the Coulomb interaction.

The total carrier density reached is larger by a factor of about five compared to the peak density in the impulsive case where the laser was fully off-resonant (the laser field envelope is the same in both cases). In the differential electron-hole density (upper left) oscillating changes are visible; this is the quantum beat between the two lowest transitions. Its period of about

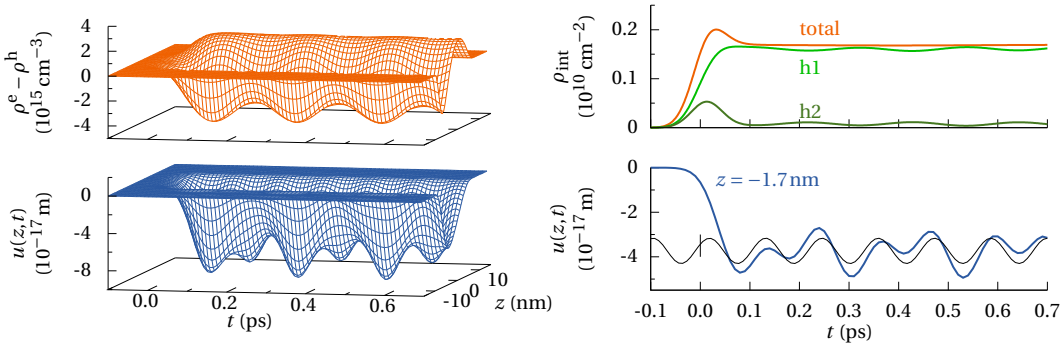

Figure 2.7: Displacive excitation dynamics (photon energy 1.50 eV, bias 50 kV/cm). The same quantities as in figure 2.6 are plotted, but note that the vertical axes have different scales. In the upper right plot, the contributions from the lowest two hole subbands to the total carrier density are shown separately. [parameter set A]

0.22 ps is almost twice the period of the LO phonon. It clearly modulates the oscillation of the lattice displacement (lower parts): the faster free lattice oscillation is superimposed with the slower quantum beat.

Still the general behavior is as expected. The lattice equilibrium position is displaced by the excitation of electron-hole pairs, and an oscillation centered around the new equilibrium sets in. The amplitude of this oscillation is significantly smaller than the total shift, simply because the displacement does not happen instantaneously but takes some time. In the case of an even slower displacement of the equilibrium, the lattice would adapt to the new situation without any ensuing oscillation. A cosine-like function fits reasonably well to the oscillation (thin black line in lower right plot). Its frequency is the LO phonon frequency, but the phase compared to a cosine is almost −60°, i.e., it is actually closer to a sine function. Several factors are responsible: the driving is not purely displacive but has an impulsive component; it is not instantaneous; and there is the quantum beat modulating the oscillation.

Although the quantum beat modulates the lattice oscillation, the amplitude of the oscillation does not increase with time. Because the quantum beat is off-resonant with regard to the LO phonon, energy transfer into the lattice oscillation is not possible (more precisely, it averages out over time). When the quantum beat vanishes, for example because of dephasing in the electronic subsystem, the unmodulated lattice oscillation will stay behind.

2.5 Resonant coherent phonon generation

2.5.1 Time-dependent picture

The situation changes completely when the quantum beat frequency coincides with the frequency of the LO phonon. Such conditions are shown in figure 2.8. Here the electric bias is 110 kV/cm, at which point the energy splitting between the e2h1 and the e2h2 transition is equal to the LO phonon energy, and the laser is centered at 1.571 eV so that its spectrum overlaps with both transitions (see figure 2.4). The position-dependent excess density (upper left of figure 2.8) exhibits oscillations with a frequency matched to the LO phonon. The electronic subsystem

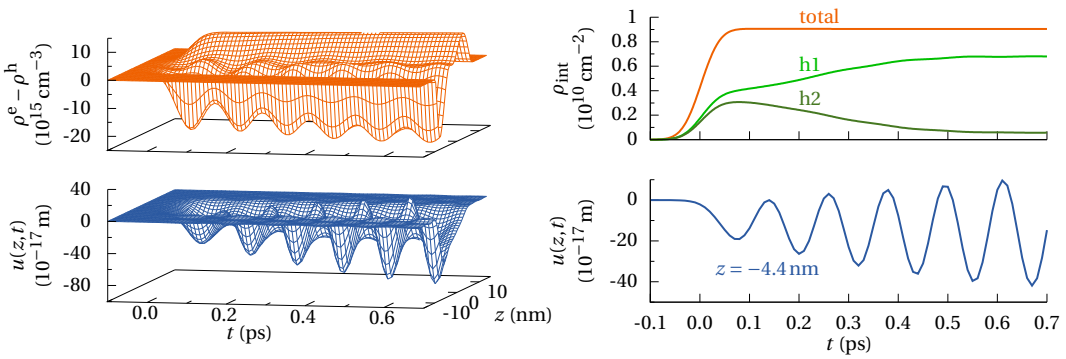

Figure 2.8: Resonant excitation dynamics (photon energy 1.57 eV, bias 110 kV/cm). Again the vertical axes have been rescaled compared to figure 2.6 and 2.7. [parameter set A]

now drives the lattice resonantly: The lattice oscillation intensifies with time (lower part of the figure), and even accounting for the higher carrier density, the oscillation amplitude achieved is much larger than it was for non-resonant driving conditions.

However, the electronic oscillation diminishes over time, a consequence of a rather fast relaxation of electrons from the second-lowest hole subband (h2) to the h1 subband. The relaxation process can be observed more clearly in the integrated number of charge carriers (upper right of figure 2.8). The total number of carriers is a smoothed-out step function, but internally the population is redistributed from the h2 subband to the h1 subband under emission of incoherent LO phonons. This process is very efficient because the resonance condition requires that the subbands have an energy splitting equal to the LO phonon energy. One could be tempted to ascribe the energy loss to the driving of coherent phonons, but this is not correct. Artificially switching off incoherent phonons in the calculations completely forestalls the relaxation, while coherent phonons are still driven. This is the first indication that energy transfer to the lattice is strongly dominated by incoherent phonons, and that the quota going into coherent phonons is all but negligible.

The absolute value of the lattice displacement under resonant driving conditions is still tiny; the oscillation amplitude at 0.7 ps of approximately 0.25 fm is six orders of magnitude smaller than the lattice constant a. Such small values are not implausible: The lattice is very tightly bound so that a displacement of $10^{-3}a$ means a huge distortion [35]. Here we have applied moderately low excitation densities and accordingly get a moderate lattice displacement. The reason that such small absolute values of displacement can still be detected in an experiment without being completely drowned in thermal or zero-point fluctuations is that spatial averaging diminishes the fluctuations, as will be discussed in chapter 3.

2.5.2 Characteristics of the RPG mechanism

In order to reveal the characteristics of the resonant phonon generation (RPG) mechanism and also to compare coherent and incoherent phonon generation, we take a look at the energy transferred to the lattice. The energetical sheet density of phonons is defined as $\langle H_{\mathrm{ph}} \rangle / A$ and

can be divided into contributions by coherent and incoherent phonons (cf. section 1.1.1):

$$D_{\mathrm{ph}} = \frac{1}{A}\langle H_{\mathrm{ph}}\rangle = \frac{\hbar\omega_{\mathrm{LO}}}{A}\sum_{\boldsymbol{q}}\left[\langle b_{\boldsymbol{q}}^{\dagger}\rangle\langle b_{\boldsymbol{q}}\rangle + \delta\langle b_{\boldsymbol{q}}^{\dagger} b_{\boldsymbol{q}}\rangle\right] = D_{\mathrm{ph,coh}} + D_{\mathrm{ph,inc}} \tag{2.23}$$

The coherent part $D_{\mathrm{ph,coh}}$ by this definition is roughly proportional to the square of the amplitude of the lattice oscillation.

This alone does not account for all of the energy leaving the electronic subsystem; the interaction part of the Hamiltonian also carries its share, and it therefore is included into the total phonon energy density

$$T_{\mathrm{ph}} = D_{\mathrm{ph}} + \frac{1}{A}\langle H_{\mathrm{Fr}}\rangle . \tag{2.24}$$

The interaction energy $\langle H_{\mathrm{Fr}}\rangle$ can become negative; for example, it provides the energy set free by polaron formation. It can be partitioned into a coherent and an incoherent part along the same lines as D_{ph}: Terms which contain the coherent phonon amplitude $\langle b_{\boldsymbol{q}}\rangle$ are added to the coherent part $T_{\mathrm{ph,coh}}$, and the remaining terms containing phonon-assisted density matrices are included into the incoherent part $T_{\mathrm{ph,inc}}$.

The energy densities $T_{\mathrm{ph,coh}}$ and $T_{\mathrm{ph,inc}}$ as functions of time in many cases have an oscillatory behavior. In order to compare the energy going into phonons under different excitation conditions we take the temporal averages up to 0.7 ps after the pulse maximum. The result is displayed in figure 2.9.

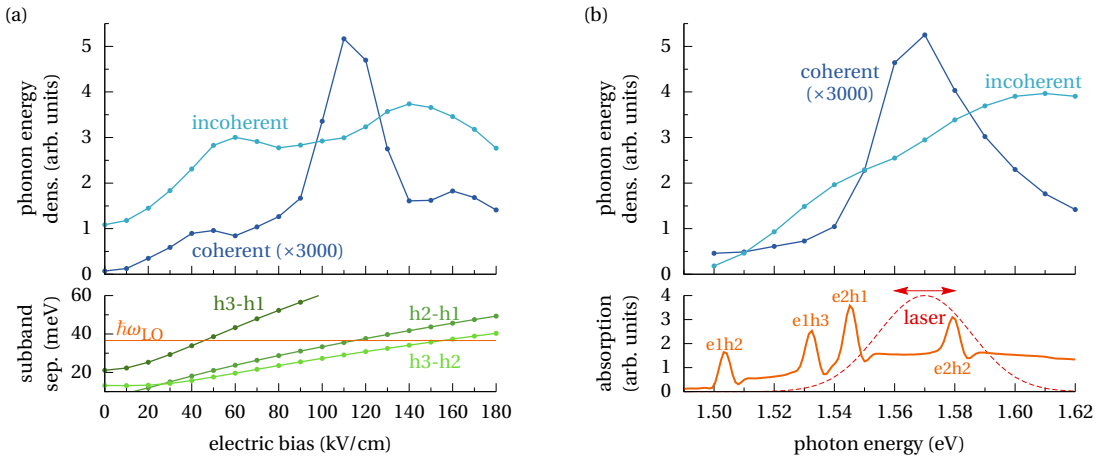

Figure 2.9: Energy transferred into coherent and incoherent phonons as a function of (a) electric field and (b) laser central energy. Plotted in the upper parts are the energy densities of coherent and incoherent phonons averaged over time. In (a), the laser central energy is fixed at 1.571 eV; the lower part shows the energetical separation of hole subbands. In (b), the electric bias is fixed at 110 kV/cm; the lower part shows the absorption spectrum and the spectral width of the laser pulse. [parameter set A (spectrum: A_s)]

The tell-tale signs of the RPG mechanism are resonant peaks of the lattice oscillation amplitude as a function of both electric bias and laser central energy. The first resonance can be clearly seen in figure 2.9 (a), where the coherent energy density $T_{\mathrm{ph,coh}}$ (averaged over time) peaks at about 110 kV/cm. This is exactly where the splitting of the h1 and h2 subbands approaches the LO phonon energy, as depicted in the lower part of the figure. Away from resonance coherent

phonon generation is much weaker. Two small humps are visible at the points where the energetical separations between h3/h1 and h3/h2 cross the LO phonon energy. These resonances are much weaker because transitions involving the h3 subband are far away from the photon energy of the laser.

The same reasoning explains the resonance in the photon energy, shown in part (b) of the figure. Coherent phonon generation is strongest when the photon energy is about 1.57 eV, which lies between the e2h1 and e2h2 exciton lines (see absorption spectrum in lower part). The quantum beat driving the lattice oscillation typically is largest if its two components are equally strong. The resonance is a little bit to right of the middle of the two transitions because the higher-energy absorption line is somewhat weaker.

Both resonances have been observed in the experiments of Ref. [30]. The results shown above agree very well with the experimental data. This even includes the absolute position of the resonances and the small shift to larger energies in the photon-energy resonance. The quantum well parameters have been chosen according to the experiment, but no further adaptations have been made.

2.5.3 The role of incoherent phonons

Figure 2.9 also shows the energy flowing into incoherent phonons. Under all excitation conditions considered, the bulk of the energy transferred to the lattice is lost to incoherent phonons. Only a small fraction actually drives the lattice oscillation; the coherent phonon energy has been multiplied by a factor of 3000 in order to make it fit into the same plot. Incoherent phonon generation cannot be avoided if coherent phonons are to be driven resonantly: In order to have a quantum beat oscillating with the LO phonon frequency, two electronic energy levels with a splitting equal to the LO phonon energy have to be excited simultaneously. This also permits relaxation from the upper to the lower level under emission of incoherent LO phonons. Evidently, the relaxation process is rather efficient.

In most experiments, incoherent phonons are invisible. Incoherent phonon generation is usually only seen indirectly, for example by measuring carrier relaxation. When observing lattice oscillations, the mean value of the lattice position is fully determined by coherent phonons, while incoherent phonons only raise the uncertainty. The uncertainties of lattice displacement and momentum are the subject of the following chapter and will be discussed in full detail there.

In figure 2.9 (a) we see that even without electric bias a significant number of incoherent phonons is created, although basically only the e1h1 transition is excited. Emission of incoherent phonons is still possible because electrons and holes are created in states high enough above the e1 and h1 subband edges and can relax downwards within their subband. At higher bias fields, more optical transitions become active, allowing inter-subband relaxation and further increasing the generation of incoherent phonons. For fields above 140 kV/cm incoherent phonons drop down again because most optical transitions included in the calculation are now shifted away from the laser energy and become weaker so that the total number of electrons and holes becomes smaller. As a function of laser energy (figure 2.9 (b)), incoherent phonon generation rises monotonically. This is to be expected as higher-energy photons excite carriers in higher subbands or at higher energies within the subbands, allowing more relaxation processes which emit LO phonons. For very high photon energies the energy density of incoherent phonons again decreases a bit; this is a numerical artifact resulting from a lack of electronic states at the

far end of the energy scale.

The large ratio between incoherent and coherent phonon generation can in principle be lowered by going to higher excitation densities: Both the coherent phonon amplitude $B_{\boldsymbol{q}}$ and the incoherent phonon population $\delta\langle b_{\boldsymbol{q}}^\dagger b_{\boldsymbol{q}}\rangle$ are driven by terms that in lowest order are proportional to the laser intensity. Because $B_{\boldsymbol{q}}$ enters quadratically into the coherent phonon energy, this energy is approximately proportional to the square of the intensity, whereas the number of incoherent phonons grows only linearly with the intensity. However, the density of photo-excited carriers cannot be increased to arbitrarily large values because of phase space filling. Under resonant conditions with the present excitation parameters, the electron-hole pair density stays below the relatively low value of $10^{10}\,\mathrm{cm}^{-2}$ (figure 2.8); the hole population $f^{\mathrm{h}}_{j\boldsymbol{k}}$ has a maximum of 0.025 at a certain point in time and k-space for the h2 subband and of 0.01 for the h1 subband. This means the carrier densities cannot be increased by a factor larger than, say, 50 before Pauli blocking becomes a major issue. Therefore, even though the RPG mechanism is the most effective one for generating coherent phonons, incoherent phonon generation will always dominate the energy transfer to the lattice for resonant or near-resonant excitation conditions.

2.5.4 Effects of the Coulomb mean-field approximation

In all simulations that have been discussed so far the Coulomb Hamiltonian had been replaced by its mean-field approximation. We now compare calculations with and without this approximation in order to check its validity. As the calculations with the full Coulomb Hamiltonian are computationally much more expensive, the model system has to be reduced to the subbands relevant for coherent phonon generation, i.e., to the e2, h1, and h2 subbands.

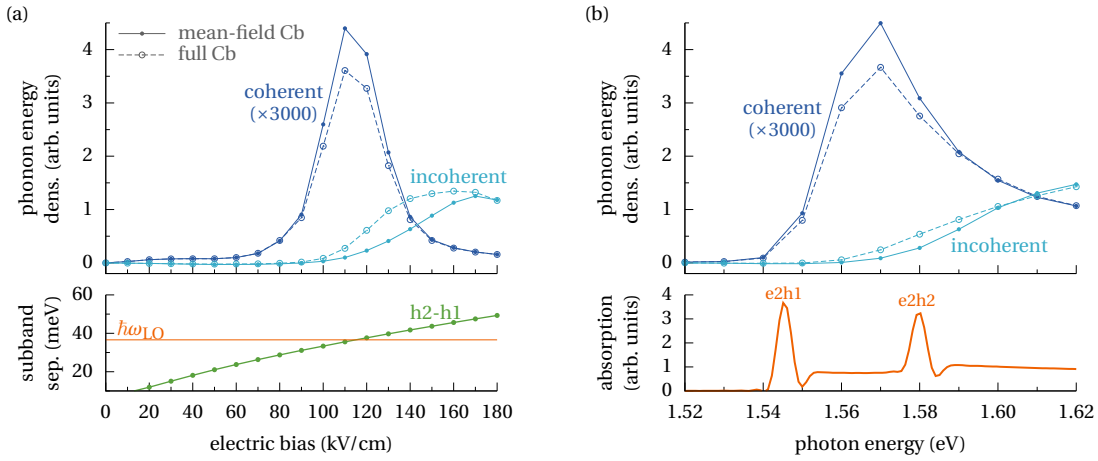

Figure 2.10: Phonon generation characteristics as in figure 2.9 for a model reduced to the most relevant subbands. The dashed lines and open circles show simulations in which the Coulomb Hamiltonian has not as usual been replaced by its mean-field approximation. [parameter set $\mathrm{A_r}$ (spectrum: $\mathrm{A_{r+s}}$)]

Figure 2.10 again shows the two resonances that are characteristic for the RPG mechanism. The coherent phonon generation as a function of the electric bias field plotted in part (a) no longer has the small side peaks that we observed previously (figure 2.9) because the h3 subband is missing. In addition, almost no incoherent phonons are generated in the region in which the subband splitting is smaller than the optical phonon energy because the relaxation of holes

under emission of incoherent phonons is energetically forbidden; relaxation of electrons to the e1 subband is not possible because it is not included in the reduced model. For the same reason, incoherent phonon generation as a function of the laser central energy (part (b)) only sets in when the energy of photons is sufficient to excite holes in the higher subband.

The simulations with the full Coulomb Hamiltonian are indicated by dashed lines, solid lines were obtained with the mean-field (MF) approximated version. The data for coherent phonons agrees reasonably well, but in particular at the resonance points coherent phonon generation is overestimated by the MF calculation. Quite to the contrary, incoherent phonon generation is too small in the MF approximation. As a result, the quantum beat is not damped as fast, which explains the larger number of coherent phonons. The deviations for incoherent phonons are larger than for coherent phonons, but there still are no qualitative differences. In view of the substantial numerical simplification that the MF approximation provides, this justifies the use of the MF Coulomb Hamiltonian in the simulations.

2.5.5 RPG in a different quantum well

In order to rule out the possibility that the good agreement between the simulations and the experiment is coincidental, we take a look at simulations modeled after a second experiment. Mizoguchi et al. [47] have traced the generation of coherent phonons in a quantum well by measuring the emitted terahertz radiation. In comparison to the previous parameters, the quantum well is a bit thinner and the laser pulse is shorter, but similar characteristics of the generation of coherent phonons have been observed. However, there is one important difference: The peak when varying the central frequency of the laser is not in between the two exciton lines which are responsible for the quantum beat, but instead lies almost directly on the higher-energy exciton line.

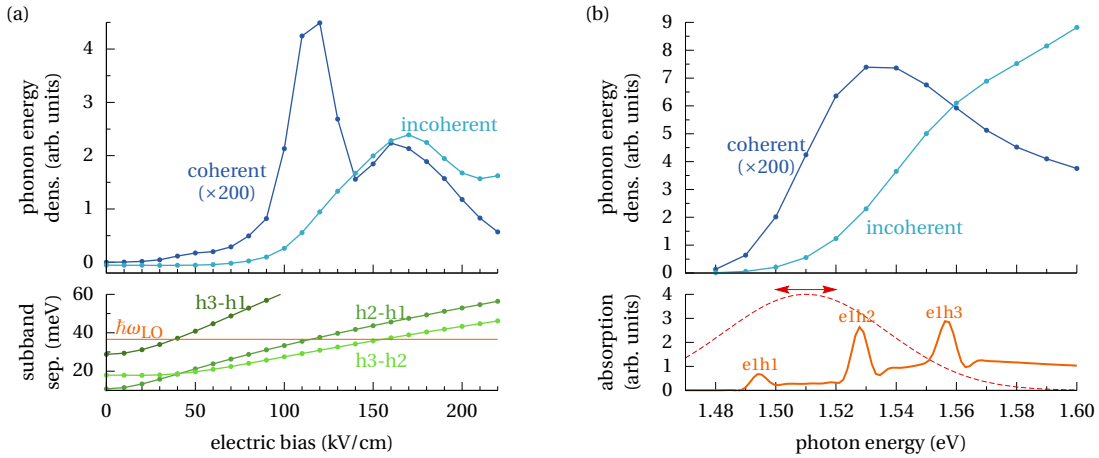

Figure 2.11: Coherent and incoherent phonon generation as in figure 2.9, but with quantum well parameters modeled after the experiment of Ref. [47]. In (a), the photon energy is 1.510 eV; in (b), the electric bias is fixed at 110 kV/cm. [parameter set B (spectrum: B_s)]

Figure 2.11 shows the characteristics of coherent and incoherent phonon generation. The optical driving strength is again set to a fixed value that creates an electron population of $10^{10}\,\mathrm{cm}^{-2}$ at 1.510 eV photon energy under an electric bias field of 110 kV/cm. In part (a) we see

coherent phonon generation peak at the point where the splitting between the e1h1 and the e1h2 exciton lines is equal to the optical phonon energy; a smaller second peak is visible where e1h2 and e1h3 fulfill the resonance condition. The experiment revealed a very similar structure, although coherent phonon generation did not go down as much at higher electric fields due to some transitions not included in our model.

Incoherent phonons are created mainly on the right hand side of the resonance because in this case there is no lower electron subband into which carrier relaxation is possible. Also as a function of the photon energy (part (b)), incoherent phonon generation is small until the e1h2 transition becomes driven. The ratio between the energies flowing into incoherent and into coherent phonons is still large, but not as large as it was for the parameters considered previously. The main reasons are the lack of a lower electron subband and the shorter laser pulse that drives coherent phonons more efficiently.

The peak of coherent phonon generation as a function of the photon energy is indeed shifted to the right so that it coincides with the e1h2 exciton. There are two reasons: First, the continuum parts of the transitions also contribute to the quantum beat, and second, at higher energies the quantum beat involving the e1h3 exciton also drives coherent phonons although it is not exactly in resonance. The simulations hence successfully reproduce the main aspects of the experimental data, including the at first sight strange position of the resonance in the photon energy.

3 Squeezed phonon states

In the preceding chapter, we have looked at the mean value of the lattice displacement field and oscillations thereof. Although the simulations were performed quantum-kinetically, the quantum nature of the lattice nuclei has so far been of no great importance; quite to the contrary, the driving mechanisms for the coherent lattice oscillations could be understood within a classical picture.

The quantum nature of the lattice becomes apparent when we look not only at the mean value of the displacement field but also at its uncertainty. According to the Heisenberg uncertainty principle, the product of the uncertainties of lattice displacement and momentum is subject to a lower bound; in other words, position and momentum cannot be arbitrarily well defined at the same time. Therefore even at zero temperature, i.e., in the ground state of the lattice, the uncertainties do not vanish. However, in principle it is possible to further lower the uncertainty of either position or momentum if at the same time the uncertainty of the other variable is increased so that the uncertainty principle is still fulfilled. Such a state, in which one of the uncertainties is smaller than its zero-temperature value, is called a squeezed state.

3.1 State of the art

Squeezed states have first been realized in light fields and are rapidly becoming an indispensable tool for optical experiments [17, 40]. Instead of position and momentum the two conjugate variables here are amplitude and phase of the electric field. By using squeezed photons, the noise of an interferometric measurement has been lowered by a factor of 18 compared to the shot noise limit achieved by usual coherent laser beams [17].

The great advances in the field of quantum optics have spawned the effort to realize squeezed states in other bosonic systems. An obvious candidate is the crystal lattice and its bosonic excitation quanta, the phonons. One of the first proposals on how to excite squeezed phonon states makes use of lattice anharmonicities, which allow one phonon to decay into a pair of two phonons of another branch [24]. This process is similar to a well-established method for creating squeezed light, namely the down-conversion of photons in a non-linear medium. However, quantum kinetic simulations of spatially-localized phonon decay have pointed out a significant difference to the optical process: The acoustic phonons created within a quantum dot by the decay of LO phonons are squeezed, but they leave behind the squeezing effect when traveling out of the dot; the reason is that the k-vector selection rules are different compared to the optical case [13]. Squeezing by phonon decay has so far not been demonstrated in an experiment.

In an experiment that shows strong indications of phonon squeezing, phonons have been excited optically via second-order Raman scattering in a potassium tantalate ($KTaO_3$) crystal [21]. The lattice uncertainty was measured also by second-order Raman scattering of a probe

pulse, revealing an oscillation with twice the phonon frequency as it is characteristic for a squeezed state. The absolute value of the uncertainty could not be established independently, but because incoherent phonon generation can be ruled out for energetical and symmetry reasons, it is plausible that at some time during the oscillation the uncertainty falls below the zero-temperature level.

The Raman model assumes an effective direct coupling between the light of the driving laser and the lattice. In $KTaO_3$, the Raman tensor of first order in the lattice displacement vanishes. Optical excitation via the second-order Raman tensor always creates pairs of phonons; in this way, it is similar to the phonon decay process discussed above. Quite generally, having a pair of phonon creation operators in the Hamiltonian within a simple approximation almost automatically leads to squeezed states, both for continuous and pulsed excitation [25, 26]. However, the assumption of direct light-phonon coupling is a rather strong simplification, in particular if the optical excitation does not fall into the band gap: Simulations of a quantum dot have shown that a single optical pulse resonant with the fundamental exciton line does not produce any phonon squeezing, in stark contrast to expectations guided by the Raman model [54]. The lattice uncertainty still oscillates with twice the phonon frequency, which has sometimes been used as a sign of squeezing, but never falls below its zero-point values; at least two short pulses are needed within that model to obtain squeezed states. This means it is necessary to go beyond the Raman model in simulations involving the dynamics of the lattice uncertainty. The model used in this work does so by including the electronic subsystem and its coupling to both the lattice and the optical driving field.

In addition to second-order Raman scattering, two other experimental methods have been employed to measure the lattice uncertainty. First there is the direct approach of repeatedly measuring the lattice displacement and calculating the sample variance. This obviously requires that the noise added by the experimental setup is not too large and of reproducible strength. Delay-time dependent variances have been reported by one group for pump-probe reflectivity measurements on a variety of systems, including semimetals (Sb, Bi), semiconductors (GaAs, InSb) and a high-temperature superconductor ($YBa_2Cu_3O_{7-x}$) [44–46]. The mechanism that creates the oscillating uncertainty is unclear; on the other hand, such oscillations are more the norm than the exception, as can be seen in the Wigner representation of a single phonon mode: they appear in every state whose Wigner function does not have an exactly circular shape [52]. More recent experiments by another group, however, have not been able to reproduce the oscillating noise in very similar measurements on bismuth and gallium arsenide, suggesting that in the initial reports an artifact of the measurement technique might have been involved [27].

The second detection method is ultrafast x-ray diffraction. Via the Debye-Waller factor, the strength of diffraction peaks depends on the lattice displacement squared and in this way the displacement uncertainty can be determined. Such measurements have shown oscillating and increasing uncertainties after optical excitation in bismuth [28]. A very strong excitation has been applied; phonons are driven by mode softening due to a large number of excited charge carriers, and accordingly the uncertainty is driven upwards and does not break the zero-point limit. The detection technique has some advantages; most importantly, the absolute value of the lattice uncertainty can be established, and x-ray diffraction is insensitive to the dynamics of the valence electrons.

3.2 Lattice uncertainties and spatial averaging

3.2.1 Uncertainties and the Heisenberg uncertainty principle

The uncertainty of an observable $\hat{A}$ is defined as

$$(\Delta A)^2 = \left\langle (\hat{A} - \langle \hat{A} \rangle)^2 \right\rangle. \tag{3.1}$$

Experimentally, it is reflected in the fluctuations of measurements: Assume that $\hat{A}$ is measured many times, either by measuring it in each of an ensemble of identically prepared systems, or, equivalently, by repeatedly measuring $\hat{A}$ in one system that before each measurement is returned to the same state. Neglecting any errors introduced by the measuring device, the uncertainty $(\Delta A)^2$ then is the variance of the set of measured values (more precisely, it is the expectation value of the unbiased sample variance).

The Heisenberg uncertainty principle gives a lower bound for the product of the uncertainties of two observables that do not commute. In any given state the uncertainties of the observables $\hat{A}$ and $\hat{B}$ with commutator $[\hat{A}, \hat{B}]$ fulfill the inequality

$$(\Delta A)^2 (\Delta B)^2 \geq \frac{1}{4} \left| \left\langle [\hat{A}, \hat{B}] \right\rangle \right|^2. \tag{3.2}$$

The right hand side in general depends on the state in question, but it can also be constant. This is the case for the most prominent pair of non-commuting observables, position $\hat{\boldsymbol{x}}$ and momentum $\hat{\boldsymbol{p}}$ of a single (point-like) particle. Here we have $[\hat{x}_i, \hat{p}_j] = \mathrm{i}\hbar\delta_{i,j}$ and accordingly

$$(\Delta x_i)^2 (\Delta p_i)^2 \geq \frac{\hbar^2}{4}. \tag{3.3}$$

A very similar result is obtained for the lattice displacement and momentum fields,

$$\hat{\boldsymbol{u}}(\boldsymbol{r}) = \sqrt{\frac{\hbar}{2NM}} \sum_{\alpha \boldsymbol{q}} \frac{1}{\sqrt{\omega_\alpha}} \boldsymbol{e}_{\alpha,\boldsymbol{q}} \left(\mathrm{e}^{\mathrm{i}\boldsymbol{q}\cdot\boldsymbol{r}} b_{\alpha,\boldsymbol{q}} + \mathrm{e}^{-\mathrm{i}\boldsymbol{q}\cdot\boldsymbol{r}} b^\dagger_{\alpha,\boldsymbol{q}} \right) \quad \text{and} \tag{3.4a}$$

$$\hat{\boldsymbol{p}}(\boldsymbol{r}) = -\mathrm{i}\sqrt{\frac{\hbar M}{2N}} \sum_{\alpha \boldsymbol{q}} \sqrt{\omega_\alpha} \boldsymbol{e}_{\alpha,\boldsymbol{q}} \left(\mathrm{e}^{\mathrm{i}\boldsymbol{q}\cdot\boldsymbol{r}} b_{\alpha,\boldsymbol{q}} - \mathrm{e}^{-\mathrm{i}\boldsymbol{q}\cdot\boldsymbol{r}} b^\dagger_{\alpha,\boldsymbol{q}} \right), \tag{3.4b}$$

whose commutator and uncertainty inequality are

$$[\hat{u}_i(\boldsymbol{r}), \hat{p}_j(\boldsymbol{r'})] = \mathrm{i}\hbar\delta_{i,j}\delta_{\boldsymbol{r},\boldsymbol{r'}} \quad \text{and} \quad (\Delta u_i(\boldsymbol{r}))^2 (\Delta p_i(\boldsymbol{r}))^2 \geq \frac{\hbar^2}{4}. \tag{3.5}$$

For this result the transverse phonon branches are necessary: even though they are not coupled, they carry part of the zero-point uncertainties.

The lattice uncertainties are determined by the incoherent phonon variables via

$$(\Delta u_i)^2 = (\Delta u_i)^2_0 + \frac{\hbar}{M\omega_{\mathrm{LO}} N} \sum_{\boldsymbol{q}\boldsymbol{q'}} \frac{q_i q'_i}{q q'} \operatorname{Re}\left[\mathrm{e}^{-\mathrm{i}(\boldsymbol{q}-\boldsymbol{q'})\cdot\boldsymbol{r}} \delta \left\langle b^\dagger_{\boldsymbol{q}} b_{\boldsymbol{q'}} \right\rangle + \mathrm{e}^{\mathrm{i}(\boldsymbol{q}+\boldsymbol{q'})\cdot\boldsymbol{r}} \delta \left\langle b_{\boldsymbol{q}} b_{\boldsymbol{q'}} \right\rangle \right], \tag{3.6a}$$

$$(\Delta p_i)^2 = (\Delta p_i)_0^2 + \frac{\hbar M \omega_{\mathrm{LO}}}{N} \sum_{\boldsymbol{q}\boldsymbol{q}'} \frac{q_i q_i'}{q q'} \operatorname{Re}\left[\mathrm{e}^{-\mathrm{i}(\boldsymbol{q}-\boldsymbol{q}')\cdot\boldsymbol{r}} \delta\langle b_{\boldsymbol{q}}^\dagger b_{\boldsymbol{q}'} \rangle - \mathrm{e}^{\mathrm{i}(\boldsymbol{q}+\boldsymbol{q}')\cdot\boldsymbol{r}} \delta\langle b_{\boldsymbol{q}} b_{\boldsymbol{q}'} \rangle \right], \tag{3.6b}$$

where we have again used the fact that only longitudinal phonons (with $\boldsymbol{e}_{\mathrm{LO},\boldsymbol{q}} = \boldsymbol{q}/q$) are driven. The transverse branches only contribute to the zero-point uncertainties

$$(\Delta u_i)_0^2 = \frac{\hbar}{2MN} \sum_{\alpha\boldsymbol{q}} \frac{1}{\omega_\alpha} (\boldsymbol{e}_{\alpha,\boldsymbol{q}})_i^2 \quad \text{and} \quad (\Delta p_i)_0^2 = \frac{\hbar M}{2N} \sum_{\alpha\boldsymbol{q}} \omega_\alpha (\boldsymbol{e}_{\alpha,\boldsymbol{q}})_i^2. \tag{3.7}$$

In (3.6) we see that an incoherent phonon population $\delta\langle b_{\boldsymbol{q}}^\dagger b_{\boldsymbol{q}} \rangle$, which is always positive, increases both the displacement and the momentum uncertainty. Squeezed states therefore require exciting two-phonon coherences $\delta\langle b_{\boldsymbol{q}} b_{\boldsymbol{q}'} \rangle$ while avoiding incoherent phonon generation. This explains why having a two-phonon operator in the Hamiltonian leads to squeezed states so easily.

If LO and TO branches do not have the same phonon frequency, the product of the zero-point lattice uncertainties is larger than the minimal value mandated by the uncertainty principle:

$$(\Delta u_i)_0^2 (\Delta p_i)_0^2 = \frac{\hbar^2}{4} \left(\frac{1}{3\omega_{\mathrm{LO}}} + \frac{2}{3\omega_{\mathrm{TO}}} \right) \left(\frac{1}{3}\omega_{\mathrm{LO}} + \frac{2}{3}\omega_{\mathrm{TO}} \right) \tag{3.8}$$

For GaAs, the right hand side is equal to $1.0013\frac{\hbar^2}{4}$, so the effect is small. The optical phonon dispersions, which in reality are not completely flat, would further increase this value [13].

Because in our model transverse phonons are not coupled, the zero-point uncertainties are the only place where they can enter into the calculations. For practical reasons, LO-TO-splitting and the resulting small increase in the uncertainty product will be neglected by setting $\omega_{\mathrm{TO}} = \omega_{\mathrm{LO}}$. This allows us to define the dimensionless lattice variables

$$\hat{\tilde{\boldsymbol{u}}}(\boldsymbol{r}) = \frac{1}{\sqrt{N}} \sum_{\alpha\boldsymbol{q}} \boldsymbol{e}_{\alpha,\boldsymbol{q}} \left(\mathrm{e}^{\mathrm{i}\boldsymbol{q}\cdot\boldsymbol{r}} b_{\alpha,\boldsymbol{q}} + \mathrm{e}^{-\mathrm{i}\boldsymbol{q}\cdot\boldsymbol{r}} b_{\alpha,\boldsymbol{q}}^\dagger \right) \quad \text{and} \tag{3.9a}$$

$$\hat{\tilde{\boldsymbol{p}}}(\boldsymbol{r}) = \frac{-\mathrm{i}}{\sqrt{N}} \sum_{\alpha\boldsymbol{q}} \boldsymbol{e}_{\alpha,\boldsymbol{q}} \left(\mathrm{e}^{\mathrm{i}\boldsymbol{q}\cdot\boldsymbol{r}} b_{\alpha,\boldsymbol{q}} - \mathrm{e}^{-\mathrm{i}\boldsymbol{q}\cdot\boldsymbol{r}} b_{\alpha,\boldsymbol{q}}^\dagger \right). \tag{3.9b}$$

The zero-point uncertainties of the dimensionless variables are simply $(\Delta \tilde{u}_i)_0^2 = (\Delta \tilde{p}_i)^2 = 1$ and the uncertainty principle becomes $(\Delta \tilde{u}_i)^2 (\Delta \tilde{p}_i)^2 \geq 1$.

The dimensioned observables can be retrieved by simple multiplication (numerical values are for GaAs):

$$\hat{\boldsymbol{u}}(\boldsymbol{r}) = \hat{\tilde{\boldsymbol{u}}}(\boldsymbol{r}) \cdot \sqrt{\hbar/(2M\omega_{\mathrm{LO}})} = \hat{\tilde{\boldsymbol{u}}}(\boldsymbol{r}) \cdot 3.99\,\mathrm{pm} \tag{3.10a}$$

$$\hat{\boldsymbol{p}}(\boldsymbol{r}) = \hat{\tilde{\boldsymbol{p}}}(\boldsymbol{r}) \cdot \sqrt{\hbar M \omega_{\mathrm{LO}}/2} = \hat{\tilde{\boldsymbol{p}}}(\boldsymbol{r}) \cdot 1.32 \cdot 10^{-23}\,\frac{\mathrm{kg\,m}}{\mathrm{s}} \tag{3.10b}$$

From now on, the dimensionless lattice variables will be used.

3.2.2 Effects of limited spatial resolution

The uncertainty of the lattice displacement field is quite large even at zero temperature: The zero-point uncertainty is $(\Delta u_i)_0 = 3.99\,\mathrm{pm}$, which is almost one percent of the lattice constant.

This is an order of magnitude larger than the amplitude of very strong lattice distortions [35], and more than three orders of magnitude above the displacements we saw in the previous chapter (see figure 2.8).

The source of the large zero-point uncertainty is that every phonon mode contributes to the uncertainty of lattice displacement (see (3.7)). This is closely related to the case of quantum electrodynamics, where the zero-point uncertainty of the electric field $\boldsymbol{E}(\boldsymbol{r})$ is infinite because of the infinite number of modes in free space [12]. The observed uncertainties are of course finite. This seeming contradiction is resolved if we consider the limited spatial resolution of measurement: Any measurement will always average over a certain volume in space and thereby excludes modes with large wave vectors. In particular, the available techniques for measuring the lattice displacement do not achieve unit-cell resolution but average over a fairly large number of unit cells. For predicting experimental outcomes it is therefore important to include spatial averaging as it can dramatically lower the perceived uncertainties.

For this purpose we define Gaussian-weighted averages of the dimensionless lattice variables. The extent of averaging is $\sigma_\parallel$ in in-plane directions and σ_z in z-direction. With $G_\sigma(x) = \left(2\pi\sigma^2\right)^{-\frac{1}{2}} \exp\left(-\frac{x^2}{2\sigma^2}\right)$ we have

$$\hat{\boldsymbol{U}} = \int G_{\sigma_\parallel}(x)\, G_{\sigma_\parallel}(y)\, G_{\sigma_\mathrm{z}}(z)\, \hat{\tilde{\boldsymbol{u}}}(\boldsymbol{r})\, \mathrm{d}^3 r = \frac{1}{\sqrt{N}} \sum_{\alpha\boldsymbol{q}} \boldsymbol{e}_{\alpha,\boldsymbol{q}}\, \mathrm{e}^{-\frac{1}{2}\left(\sigma_\parallel^2 (q_\mathrm{x}^2+q_\mathrm{y}^2)+\sigma_\mathrm{z}^2 q_\mathrm{z}^2\right)} \left(b_{\alpha,\boldsymbol{q}} + b_{\alpha,\boldsymbol{q}}^\dagger\right), \quad (3.11a)$$

$$\hat{\boldsymbol{P}} = \int G_{\sigma_\parallel}(x)\, G_{\sigma_\parallel}(y)\, G_{\sigma_\mathrm{z}}(z)\, \hat{\tilde{\boldsymbol{p}}}(\boldsymbol{r})\, \mathrm{d}^3 r = \frac{-\mathrm{i}}{\sqrt{N}} \sum_{\alpha\boldsymbol{q}} \boldsymbol{e}_{\alpha,\boldsymbol{q}}\, \mathrm{e}^{-\frac{1}{2}\left(\sigma_\parallel^2 (q_\mathrm{x}^2+q_\mathrm{y}^2)+\sigma_\mathrm{z}^2 q_\mathrm{z}^2\right)} \left(b_{\alpha,\boldsymbol{q}} - b_{\alpha,\boldsymbol{q}}^\dagger\right). \quad (3.11b)$$

In the k-space representation we see that contributions from modes with large wave vectors are diminished by the exponential function.

The zero-point uncertainties of the averaged variables are

$$(\Delta U_i)_0^2 = (\Delta P_i)_0^2 = \frac{1}{32\sqrt{\pi^3}} \frac{a^3}{\sigma_\parallel^2 \sigma_\mathrm{z}}, \quad (3.12)$$

which obviously is much smaller than $(\Delta \tilde{u}_i)_0^2 = 1$ if the averaging extends over many unit cells. The uncertainty principle for these variables reads $(\Delta U_i)^2\,(\Delta P_i)^2 \geq (\Delta U_i)_0^2\,(\Delta P_i)_0^2$. The uncertainties are given by

$$(\Delta U_i)^2 = (\Delta U_i)_0^2 + \frac{2}{N} \sum_{\boldsymbol{k} q_\mathrm{z} q_\mathrm{z}'} \frac{q_i q_i'}{q q'}\, \mathrm{e}^{-\sigma_\parallel^2 k^2 - \frac{1}{2}\sigma_\mathrm{z}^2 (q_\mathrm{z}^2 + q_\mathrm{z}'^2)}\, \mathrm{Re}\left(\delta n_{\boldsymbol{k} q_\mathrm{z} q_\mathrm{z}'} + \delta b_{\boldsymbol{k} q_\mathrm{z} q_\mathrm{z}'}\right), \quad (3.13a)$$

$$(\Delta P_i)^2 = (\Delta P_i)_0^2 + \frac{2}{N} \sum_{\boldsymbol{k} q_\mathrm{z} q_\mathrm{z}'} \frac{q_i q_i'}{q q'}\, \mathrm{e}^{-\sigma_\parallel^2 k^2 - \frac{1}{2}\sigma_\mathrm{z}^2 (q_\mathrm{z}^2 + q_\mathrm{z}'^2)}\, \mathrm{Re}\left(\delta n_{\boldsymbol{k} q_\mathrm{z} q_\mathrm{z}'} - \delta b_{\boldsymbol{k} q_\mathrm{z} q_\mathrm{z}'}\right). \quad (3.13b)$$

$\boldsymbol{k}$ is an in-plane wave vector and the in-plane projection of both $\boldsymbol{q}$ and $\boldsymbol{q'}$, i.e., $\boldsymbol{q} = \boldsymbol{k} + q_\mathrm{z}\boldsymbol{e}_\mathrm{z}$ and $\boldsymbol{q'} = \boldsymbol{k} + q_\mathrm{z}'\boldsymbol{e}_\mathrm{z}$. The phonon correlations are defined by $\delta n_{\boldsymbol{k} q_\mathrm{z} q_\mathrm{z}'} = \delta\langle b_{\boldsymbol{q}}^\dagger b_{\boldsymbol{q'}}\rangle$ and $\delta b_{\boldsymbol{k} q_\mathrm{z} q_\mathrm{z}'} = \delta\langle b_{\boldsymbol{q}} b_{-\boldsymbol{k}+q_\mathrm{z}'\boldsymbol{e}_\mathrm{z}}\rangle$.

We now make a small approximation that allows us to account for the extent of the spatial average by an analytical expression and at the same time greatly reduces the numerical complexity of the simulations. In short, the approximation exploits the fact that only phonon variables with small q contribute to the uncertainties by substituting them with an appropriately defined limit

for $q \to 0$.

We begin by noting that the Gaussian factors in (3.13) for realistic values of $\sigma_\parallel$ and σ_z exclude all phonon variables which do not have very small indices k, q_z and q'_z: For example, even if we assume a very high spatial resolution of $\sigma_z = 20\,\mathrm{nm}$, the corresponding Gaussian in k-space has a standard deviation of $\sigma_q = 1/\sigma_z = 0.05\,\mathrm{nm}^{-1}$, which is actually smaller than the discretization step used in the calculations ($0.1\,\mathrm{nm}^{-1}$, see figure 1.3). In particular for the in-plane directions, a resolution of $\sigma_\parallel = 5\,\mu\mathrm{m}$ is much more realistic as it is limited by, e.g., the laser spot size.

On these small wave-vector scales the phonon variables almost exactly obey the following limiting behavior:

$$\delta n_{\boldsymbol{k} q_z q'_z} \approx \frac{1}{q q'} \left(C_{1z} q_z q'_z + C_{1\parallel} k^2 \right) \qquad \delta b_{\boldsymbol{k} q_z q'_z} \approx \frac{1}{q q'} \left(C_{2z} q_z q'_z + C_{2\parallel} k^2 \right) \tag{3.14}$$

where the $C_{\dots}$ are constants that depend on the phonon state. This behavior can be derived strictly with the help of the equations of motion, which will be discussed in section 3.4. It is a consequence of the q-dependence of the phonon coupling element $g_{\boldsymbol{q}}$, which obviously governs the q-dependence of the phonon variables.

Inserting the limiting behavior into the uncertainties (3.13) yields

$$(\Delta U_z)^2 = (\Delta U_z)_0^2 + 2\,\mathrm{Re}\left(C_{1z} + C_{2z}\right) \cdot S(\sigma_\parallel, \sigma_z) \qquad \text{and} \tag{3.15a}$$

$$(\Delta P_z)^2 = (\Delta P_z)_0^2 + 2\,\mathrm{Re}\left(C_{1z} - C_{2z}\right) \cdot S(\sigma_\parallel, \sigma_z) \qquad \text{with} \tag{3.15b}$$

$$S(\sigma_\parallel, \sigma_z) = \frac{1}{N} \sum_{\boldsymbol{k} q_z q'_z} \frac{{q_z}^2 {q'_z}^2}{q^2 q'^2} \, \mathrm{e}^{-\sigma_\parallel^2 k^2 - \frac{1}{2}\sigma_z^2 ({q_z}^2 + {q'_z}^2)} \tag{3.15c}$$

Here we again consider only the z-component of the lattice variables because lattice displacement is restricted to this direction (section 2.2.2). The lattice uncertainties of course also have in-plane components, and those can be different from their zero-point values without breaking the symmetry, but as changing the uncertainty seems more interesting in the direction in which coherent displacement is possible, we will not further consider the other directions. However, calculating those is perfectly possible with the method described here; in that case, $C_{1\parallel}$ and $C_{2\parallel}$ determine the uncertainties.

The spatial averaging hence reduces the relevant phonon variables to those in the limit of vanishing wave vectors; the dynamics of the other phonon modes only influences the uncertainties indirectly. In this sense the $q = 0$ phonon mode fully determines the experimentally accessible lattice uncertainties. In what follows, $q = 0$ in any phonon variable refers to the limit $q \to 0$ with $\boldsymbol{q} = q_z \boldsymbol{e}_z$ and $q_z > 0$. For example, this allows us to write $C_{1z} = \delta \langle b_0^\dagger b_0 \rangle$.

The uncertainties depend on the extent of averaging only via the function $S(\sigma_\parallel, \sigma_z)$. By substituting the sums by integrals it can be calculated analytically. A rather long calculation yields

$$S(\sigma_\parallel, \sigma_z) = (\Delta U_z)_0^2 \left(\frac{N}{4}\right)^{\frac{1}{3}} \frac{a}{\sigma_z} F(\sigma_\parallel / \sigma_z) \quad \text{with} \tag{3.16}$$

$$F(r) = \frac{r^2 \left[r^2 - 1 + \frac{\pi}{2} - \frac{2r^2}{\sqrt{2r^2-1}} \arctan\left(\sqrt{2r^2-1}\right) \right]}{\pi^{\frac{1}{2}} (r^2-1)^2}. \tag{3.17}$$

The singularities in the definition of $F(r)$ are removable discontinuities; the function is also defined (and real) for values smaller than $1/\sqrt{2}$ as $\arctan(\mathrm{i}y) = \mathrm{i}\,\mathrm{artanh}(y)$. As can be seen in figure 3.1, $F(r)$ is a monotonic function that asymptotically approaches $1/\sqrt{\pi}$.

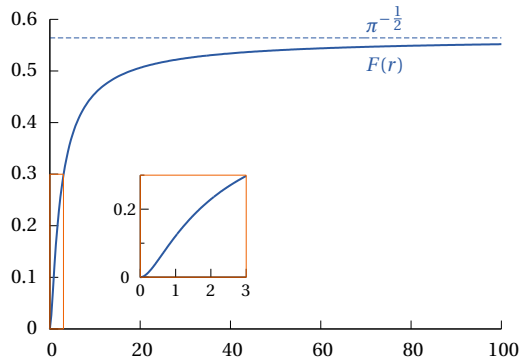

Figure 3.1: The function $F(r)$ that determines the dependence of the uncertainties on the aspect ratio of the averaging extent, $r = \sigma_\parallel/\sigma_z$.

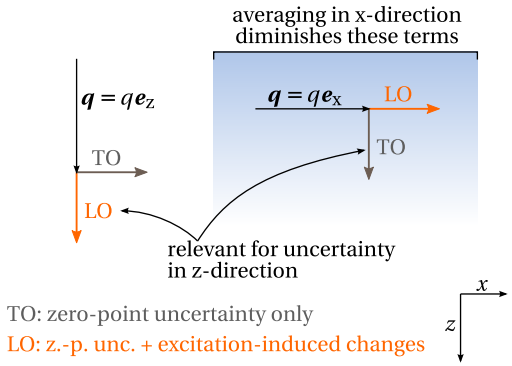

Figure 3.2: Contributions to the lattice uncertainties in z-direction from LO and TO phonons for $\boldsymbol{q}$-vectors in different directions.

The physical interpretation of the behavior of $S(\sigma_\parallel, \sigma_z)$ is as follows: Averaging over a larger volume naturally decreases the uncertainty of measurement; this does not only affect the zero-point uncertainties, but the uncertainties as a whole, and hence S includes the factor $(\Delta U_z)_0^2$ (remember that this factor is proportional to $(\sigma_\parallel^2 \sigma_z)^{-1}$ via (3.12)). The additional factor $1/\sigma_z$ is there because the quantum well has a certain limited width; increasing σ_z beyond that width diminishes the signal from the quantum well in favor of the constant signal from the barrier. The factor $F(r)$ means that the optically-induced changes of the uncertainties in z-direction are increased when the averaging volume is deformed to be larger in in-plane directions than in z-direction. This is explained in figure 3.2: If $\sigma_\parallel$ is large, this reduces the effect of phonons whose wave-vector points in an in-plane direction (see (3.13)); those phonons do not contribute excitation-induced changes to the uncertainties in z-direction. For large ratios $r = \sigma_\parallel/\sigma_z \gg 1$, LO phonons account for almost all of the uncertainties, at which point it becomes futile to further increase the ratio; this is reflected in the asymptotic behavior of $F(r)$.

For an experimental observation of changes in the uncertainties it is therefore beneficial to have a large ratio $\sigma_\parallel/\sigma_z$ and to keep σ_z as small as possible. Such a small averaging extent in z-direction could be achieved by a detection technique that is primarily sensitive to the well material, e.g., an optical pump-probe measurement where the probe pulse has an energy between the band gap energies of well and barrier. σ_z still has to be larger than the width of the quantum well as otherwise the approximation (3.14) is no longer valid. For definiteness, $\sigma_z = 20\,\mathrm{nm}$ and $\sigma_\parallel = 5\,\mu\mathrm{m}$ have been chosen for the simulations in this work. Different parameters can easily be applied with the equations just shown.

Finally, we take a look at the effects of spatial averaging on the coherent phonon variables, lattice displacement and momentum, which are only trivially affected:

$$U_z = 2\,\mathrm{Re}\,\tilde{B}_0 \cdot \left(\frac{4}{N}\right)^{\frac{1}{6}} \frac{1}{\sqrt{8\pi}} \frac{a}{\sigma_z}, \qquad P_z = 2\,\mathrm{Im}\,\tilde{B}_0 \cdot \left(\frac{4}{N}\right)^{\frac{1}{6}} \frac{1}{\sqrt{8\pi}} \frac{a}{\sigma_z}, \tag{3.18}$$

where $\tilde{B}_0 = \lim_{q_z \to 0} \operatorname{sgn}(q_z) \langle b_{q_z} \rangle$. As expected, the averaging in in-plane directions has no effect because the system is homogeneous in these directions. The variables are proportional to $1/\sigma_z$ because of the limited size of the quantum well: again a large σ_z means averaging mostly over barrier material, which decreases the contribution from the quantum well to the average.

3.3 Quantum kinetics: Why we need a new method

In principle we should now be able to calculate the lattice uncertainties after optical excitation with the same quantum kinetic simulations that have been used in the previous chapter. However, it turns out that density matrix theory with correlation expansion produces some problems when it comes to calculating the lattice uncertainties.

3.3.1 The problem with divergent terms

In the second-order correlation expansion calculations, the equations of motion possess divergent terms that do not cancel each other. The modulus of the phonon coupling element $g_{\boldsymbol{q}}$ tends to infinity for $q \to 0$, a consequence of the long-range Coulomb interaction that brings forth the Fröhlich interaction. In an overall charge-neutral system, these divergences should balance out each other. They do so in first-order correlation expansion (in which all uncertainties stay on their zero-point level for all times), but in second order some divergent terms remain in the equation of motion for the phonon-assisted variables. This is clearly unphysical and particularly alarming because the phonon variables in the limit $q \to 0$, as we have just seen, fully determine the experimentally accessible lattice uncertainties.

Let us take a closer look at how the divergent terms emerge. The critical part of the equation of motion for the phonon-assisted variable δs^{e} is this (full equation on p. 75):

$$\mathrm{i}\hbar \frac{\mathrm{d}}{\mathrm{d}t} \delta s^{\mathrm{e}\, i i'}_{\boldsymbol{k}\boldsymbol{k}' q_z} = \sum_{i_1 i_2} f^{\mathrm{e}}_{i i_1 \boldsymbol{k}'} g^{* i_1 i_2}_{\boldsymbol{q}} (\delta_{i_2 i'} - f^{\mathrm{e}}_{i_2 i' \boldsymbol{k}}) - \sum_{j_1 j_2} g^{* j_2 j_1}_{\boldsymbol{q}} p^{*}_{j_2 i \boldsymbol{k}'} p_{j_1 i' \boldsymbol{k}} + \ldots \tag{3.19}$$

$|g^{i_1 i_2}_{\boldsymbol{q}}|$ tends to infinity for small $q = |\boldsymbol{k}' - \boldsymbol{k} + q_z \boldsymbol{e}_z|$ if the subband indices are diagonal ($i_1 = i_2$). In some cases the two divergent terms in the equation cancel each other, but consider a state like

$$|\psi\rangle = \alpha c^{\dagger}_{i\boldsymbol{k}'} d^{\dagger}_{j\boldsymbol{k}} b^{\dagger}_{\boldsymbol{q}} |0\rangle + \beta |0\rangle \quad \text{with} \quad |\alpha|^2 + |\beta|^2 = 1. \tag{3.20}$$

Physically, such a state develops when an optical excitation creates a superposition of the ground state and an electron-hole pair, which then is scattered at the lattice, emitting a phonon. In this state, there is an electronic population f^{e} (unless $\alpha = 0$), but the polarization p vanishes. Consequently, the second term in (3.19) vanishes, leaving behind the divergence in the first term. A closer look at the equations of motion confirms that situations similar to this simplified case actually do arise in the second-order calculations.

The offending term in (3.19) originates from the following non-factorized part of the equation of motion:

$$\sum_{i_1 \boldsymbol{k}_1} \langle c^{\dagger}_{i\boldsymbol{k}} c^{\dagger}_{i_1 \boldsymbol{k}_1} c_{i_1 \boldsymbol{k}_1} c_{i'\boldsymbol{k}} \rangle - \sum_{j_1 \boldsymbol{k}_1} \langle c^{\dagger}_{i\boldsymbol{k}} d^{\dagger}_{j_1 \boldsymbol{k}_1} d_{j_1 \boldsymbol{k}_1} c_{i'\boldsymbol{k}} \rangle + \langle c^{\dagger}_{i\boldsymbol{k}} c_{i'\boldsymbol{k}} \rangle = C^{i i'}_{\boldsymbol{k}} \tag{3.21}$$

Actually, $C^{ii'}_{\boldsymbol{k}}$ vanishes at all times. This can be seen by inserting the operator of the total number of electrons,

$$\hat{N} = N_0 + \sum_{i\boldsymbol{k}} c^\dagger_{i\boldsymbol{k}} c_{i\boldsymbol{k}} - \sum_{j\boldsymbol{k}} d^\dagger_{j\boldsymbol{k}} d_{j\boldsymbol{k}}\,, \tag{3.22}$$

where N_0 is the number of valence band states that are filled in the electron-hole vacuum state; holes are counted negatively because they represent an annihilated valence band electron. The vanishing $C^{ii'}_{\boldsymbol{k}}$ eliminates the divergent terms. However, when it is factorized during correlation expansion, it turns into

$$C^{ii'}_{\boldsymbol{k}} \approx \sum_{i_1} f^{\mathrm{e}}_{ii_1\boldsymbol{k}} \left(\delta_{i_1 i'} - f^{\mathrm{e}}_{i_1 i'\boldsymbol{k}}\right) - \sum_{j_1} p^*_{j_1 i\boldsymbol{k}} p_{j_1 i'\boldsymbol{k}}, \tag{3.23}$$

which does not vanish in all cases as shown above and hence leaves behind divergent terms.

So in short, due to the correlation expansion certain integrals of motion ($C^{ii'}_{\boldsymbol{k}}$ and similar terms) are replaced with their factorization that is not conserved, which provokes divergences in the equations of motion. The physical reason is that even though an electron-hole pair is still fully correlated after scattering with a phonon, this correlation cannot be perceived correctly by the down-factorized electronic variables. Although both f^{e} and p originate from the same non-factorized term, their view of the same state is, in a sense, inconsistent. A related effect introduced by the factorization has been observed in calculations concerned with the terahertz emission of optically excited superlattices: In correlation expansion, the terahertz spectrum contains unphysical frequencies when dephasing of the electronic variables is included [2].

The problem of divergent terms can be circumvented in the following way: We go back to the equations of motion before they are factorized by correlation expansion and cancel all divergent terms with the help of charge neutrality. Only then the factorization procedure is applied. As long as we focus on uncertainties in z-direction, this boils down to replacing the phonon coupling element $g_{q=0}$ with the zeroth term of the Laurent series of $g_{q_z \boldsymbol{e}_z}$ about the point $q_z = 0$; the divergence, in case it arises, is contained in the minus-first term. Explicitly this means

$$g^{n_1 n_2}_{q_z \boldsymbol{e}_z} \overset{q_z \approx 0}{=} \operatorname{sgn}(q_z) \sqrt{\frac{e^2 \hbar \omega_{\mathrm{LO}}}{2\varepsilon_0 V} \left(\frac{1}{\varepsilon_\infty} - \frac{1}{\varepsilon_s}\right)} \int \phi^*_{n_1}(z)\, z\, \phi_{n_2}(z) \mathrm{d}z. \tag{3.24}$$

The sign function is dealt with by including it into the phonon variables, which results in a finite and definite value for $g_{q=0}$. This procedure has been followed in all simulations (also in the preceding chapter).

3.3.2 Unphysical uncertainties

Even when the divergent terms are corrected, another issue comes up. The dynamics of the lattice uncertainties obtained by simulations with correlation expansion shows dubious and in some cases downright unphysical behavior. An example is presented in figure 3.3, which shows the lattice uncertainties after impulsive excitation (the data is from the same simulation as discussed in section 2.4.1). Thick lines are from second-order correlation expansion; for comparison, the thin dashed lines show a more physical behavior obtained with a different

hierarchy-truncation scheme called order separation that will be explained later.

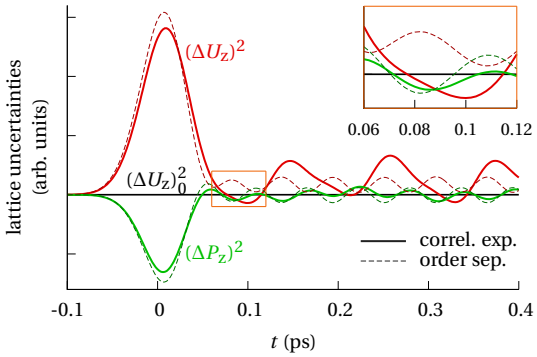

Figure 3.3: Lattice uncertainties after impulsive excitation. Thick solid lines show simulations using correlation expansion, thin dashed lines are obtained by order separation. [parameters as in figure 2.6]

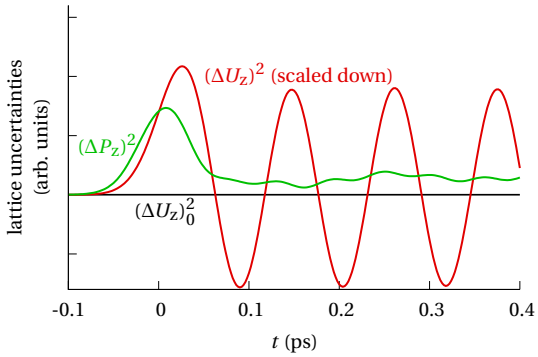

Figure 3.4: Situation identical to figure 3.3, but with $z = 0$ at the left hand side of the quantum well instead of in its center. The distance of $(\Delta U_z)^2$ to the zero-point level is scaled down by a factor of seven.

At some times (for example around 0.09 ps), lattice and momentum uncertainty simultaneously fall below their zero-point level, in violation of the uncertainty principle. The deviations from the correct behavior shown by the dashed lines are not too large for the momentum uncertainty, but are much worse for the displacement uncertainty. (Why order separation produces the "correct" dynamics will be argued later.) It is known that correlation expansion sometimes produces symptoms like negative population numbers, but those deviations are usually small and only occur after some time. Here they turn up very fast and are rather substantial.

In order to understand where the problem comes from and how it can be fixed, we take a look at a strongly simplified version of the equations of motion that permits an analytical solution. This will also rule out the possibility that the unphysical uncertainties are an artifact caused by a numerical or implementation error.

The equations of motion from second-order correlation expansion are reduced by (a) including only terms of lowest non-vanishing order in the excitation density, (b) including only one electron and one hole subband and setting all wave vectors to zero (this requires eliminating the singularity in $g_{\boldsymbol{q}}$ as described above), and (c) not considering Coulomb interaction and driving by the laser field. This leaves us with the following set of equations:

$$\mathrm{i}\hbar\frac{\mathrm{d}}{\mathrm{d}t}p = \left(\varepsilon^{\mathrm{e}} + \varepsilon^{\mathrm{h}}\right)p + \left(g^{\mathrm{e}} - g^{\mathrm{h}}\right)\delta s^{\mathrm{he}} \tag{3.25a}$$

$$\mathrm{i}\hbar\frac{\mathrm{d}}{\mathrm{d}t}\delta s^{\mathrm{he}} = \left(\varepsilon^{\mathrm{e}} + \varepsilon^{\mathrm{h}} + \hbar\omega_{\mathrm{LO}}\right)\delta s^{\mathrm{he}} + \left(g^{\mathrm{e}*} - g^{\mathrm{h}*}\right)p \tag{3.25b}$$

$$\mathrm{i}\hbar\frac{\mathrm{d}}{\mathrm{d}t}\delta s^{\mathrm{e/h}} = \hbar\omega_{\mathrm{LO}}\delta s^{\mathrm{e/h}} \pm g^{\mathrm{e/h}*} f^{\mathrm{e/h}} \mp g^{\mathrm{h/e}*}|p|^2 \tag{3.25c}$$

$$\mathrm{i}\hbar\frac{\mathrm{d}}{\mathrm{d}t}\delta n = 2\mathrm{i}\,\mathrm{Im}\left(-g^{\mathrm{e}}\delta s^{\mathrm{e}} + g^{\mathrm{h}}\delta s^{\mathrm{h}}\right) \tag{3.25d}$$

The electronic populations f^{e} and f^{h} are constant in this simplification as the terms with $\delta s^{\mathrm{e/h}}$ in their equations of motion balance out. As initial conditions we set all variables to zero except for $p(t=0) = p_0$ and $f^{\mathrm{e}} = f^{\mathrm{h}} = |p_0|^2 \ll 1$. This corresponds to an ultrafast optical excitation at

$t = 0$ that creates some electronic populations while leaving the slower phonon subsystem in its ground state. Normally we would have $|p_0|^2 = f^{\mathrm{e}}(1 - f^{\mathrm{e}})$, but since the model is restricted to the lowest non-vanishing order in the excitation strength, the quadratic term is removed.

The analytical solution for the number of incoherent phonons yields

$$\delta n(t) = 2\frac{|g^{\mathrm{e}}|^2 f^{\mathrm{e}} + |g^{\mathrm{h}}|^2 f^{\mathrm{h}} - \mathrm{Re}(g^{\mathrm{e}} g^{\mathrm{h}*})|p_0|^2}{\hbar^2 \omega_{\mathrm{LO}}^2}(1 - \cos(\omega_{\mathrm{LO}} t)) - \frac{2\,\mathrm{Re}(g^{\mathrm{e}} g^{\mathrm{h}*})|p_0|^2}{\hbar^2 \Omega^2}(1 - \cos(\Omega t)) \qquad \text{with} \qquad \Omega = \frac{1}{\hbar}\sqrt{4|g^{\mathrm{e}} - g^{\mathrm{h}}|^2 + (\hbar\omega_{\mathrm{LO}})^2}. \quad (3.26)$$

This expression can acquire values smaller than zero, for example when the first term is close to zero while the second is negative. A negative number of incoherent phonons is of course unphysical and it immediately leads to a violation of the uncertainty principle. In addition, the solution is not invariant to an addition of the same constant to both g^{e} and g^{h}; physically, that should change nothing, because it is equivalent to a shift of the point of origin of the z-coordinate, as can be seen in (3.24).

The following observation guides us to the source of the problem: Both issues would be nonexistent if ω_{LO} and Ω were equal (since $|g^{\mathrm{e}}|^2 + |g^{\mathrm{h}}|^2 - 2\,\mathrm{Re}(g^{\mathrm{e}} g^{\mathrm{h}*}) = |g^{\mathrm{e}} - g^{\mathrm{h}}|^2 \geq 0$). Ω is a renormalized phonon energy; it first turns up in the analytical solutions for p and δs^{he}. The renormalization is due to the electron-phonon interaction. Apparently correlation expansion is mixing some terms that have renormalized energies with others that are not renormalized, causing the observed problems. In some way this is similar to the non-vanishing divergences discussed in the previous subsection: In that case the problem arose because a variable that is sensitive to phonon scattering was mixed with another one that is not. A possible solution therefore would be to do some record-keeping that prevents differently renormalized terms (i.e., terms of different order in the electron-phonon interaction) from being mixed up. A method based on this idea will be introduced in the next section.

In order to check whether the identification of the source of the problem can be extended from the simplified equations to the full simulations, we can change the point of origin of the z-coordinate. The analytical solution suggests that this should noticeably affect the results for the lattice uncertainties. It indeed does so, as can be seen in figure 3.4, where the origin of the z-coordinate has been moved to the left hand side of the quantum well: Both displacement and momentum uncertainty are completely different to the case where $z = 0$ lies in the center of the quantum well (figure 3.3). In particular the displacement uncertainty acquires values far below the zero-point level that are not compensated for by an increased momentum uncertainty.

These problems of correlation expansion might be taken as an indication that the simulations of the previous chapter cannot be trusted. However, those results are physically plausible and, to the degree where experimental data exists, they agree very well with that data; moreover, the simulations with order separation shown above are in almost perfect agreement with correlation expansion when the dynamics of lattice displacement and momentum are considered. In order to check whether the results for incoherent phonon generation also are reliable, the simulations have been redone with the same shift in the z-coordinate as discussed above. For both coherent and incoherent phonon energy densities this produced almost no difference. Correlation expansion is therefore perfectly well-suited to study coherent phonon generation and also the energy flow into incoherent phonons, but for calculating lattice uncertainties a

different method is needed.

The reduced system of equations (3.25) can be understood as a model of a quantum dot. Assuming that electron and hole can only be created and annihilated as a pair, there are only two energy levels: the ground state without electron and hole, and the excited state where both the electron and the hole state are populated. In this case the Fock space of the model can be reduced by substituting hole operators by electron operators via the identity $c^\dagger c = d^\dagger d$ [31]. Doing so before correlation expansion is applied also eliminates the problems we have discussed. However, this obviously only works for a quantum dot modeled as a two-level system.

3.4 Quantum kinetics: Order separation

Order separation is built on a basic concept: The dynamical variables are expanded into orders of the Fröhlich coupling element g and the laser amplitude E, and contributions of different order are kept strictly separated. This will prevent any mixing of differently-renormalized energies and also guarantees the conservation of all integrals of motion. For any given order in g and E, a closed set of equations follows. The infinite hierarchy that is caused by the Fröhlich interaction is truncated because highly-correlated variables also are of high order in g (the exact relationship depends on the complexity of the initial state). The expansion in E for the same reason cuts off the hierarchy that arises due to the coupling to the laser field.

Order separation can directly be applied to density matrix theory. As long as the initial state is a pure state, an equivalent formulation exists that is based on an expansion of the state vector. The latter method has the advantage that the equations of motion are both easily derived and understood, and it can greatly reduce the numerical complexity in some special cases. Because it is also conceptually easier, we begin with that method.

3.4.1 State vector formulation

The state vector formulation is derived by setting up the equation of motion for the state of the system via the Schrödinger equation

$$\mathrm{i}\hbar\frac{\mathrm{d}}{\mathrm{d}t}\left|\psi\right\rangle = H\left|\psi\right\rangle. \tag{3.27}$$

We assume that the system initially is in its ground state $|0\rangle$. Because there are neither electrons nor holes, Coulomb and Fröhlich interaction have no effect on this state. Optical driving, however, excites electron-hole pairs:

$$H_{\mathrm{opt}}|0\rangle = \sum_{ij\boldsymbol{k}}\left(-\boldsymbol{E}\cdot\boldsymbol{M}_{ij}\right)c^\dagger_{i\boldsymbol{k}}d^\dagger_{j,-\boldsymbol{k}}|0\rangle \tag{3.28}$$

This state is of order E^1g^0 because it is reached by applying once the optical driving Hamiltonian H_{opt}, which is proportional to the strength of the laser field. The state of the system of the order E^1g^0 (abbreviated as (1,0)) is of the general form

$$\left|\psi^{\mathrm{cd}(1,0)}\right\rangle = \sum_{ij\boldsymbol{k}}\alpha^{\mathrm{cd}(1,0)}_{ij\boldsymbol{k}}c^\dagger_{i\boldsymbol{k}}d^\dagger_{j,-\boldsymbol{k}}|0\rangle. \tag{3.29}$$

Applying the Hamiltonian H to this state and omitting orders higher than $(1,0)$ yields

$$H\left|\psi^{\mathrm{cd}(1,0)}\right\rangle\Big|^{(1,0)} = \sum_{ijk}\left[\alpha^{\mathrm{cd}(1,0)}_{ijk}\left(\varepsilon^{\mathrm{e}}_{ik}+\varepsilon^{\mathrm{h}}_{j,-k}\right) - \sum_{i_1 j_1 k_1} V^{ij_1ji_1}_{k_1}\alpha^{\mathrm{cd}(1,0)}_{i_1 j_1 k-k_1}\right] c^\dagger_{ik} d^\dagger_{j,-k}|0\rangle\,, \tag{3.30}$$

which again is of the same form. This allows us to write down the equation of motion for the coefficient $\alpha^{\mathrm{cd}(1,0)}$:

$$\mathrm{i}\hbar\frac{\mathrm{d}}{\mathrm{d}t}\alpha^{\mathrm{cd}(1,0)}_{ijk} = -\boldsymbol{E}\cdot\boldsymbol{M}_{ij} + \alpha^{\mathrm{cd}(1,0)}_{ijk}\left(\varepsilon^{\mathrm{e}}_{ik}+\varepsilon^{\mathrm{h}}_{j,-k}\right) - \sum_{i_1 j_1 k_1} V^{ij_1ji_1}_{k_1}\alpha^{\mathrm{cd}(1,0)}_{i_1 j_1 k-k_1} \tag{3.31}$$

The interpretation is straight-forward. The first term describes the creation of electron-hole pairs by optical driving; the second term produces the phase oscillation that is determined by the free particle energy of the state; and the third term is the Coulomb attraction between electron and hole.

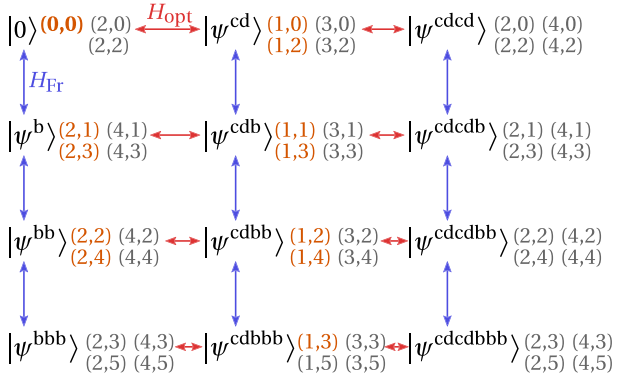

Figure 3.5: Components of the state vector. The pair (m,n) stands for the order $E^m g^n$. Orders actually used in the simulations are highlighted.

Several higher-order terms have been omitted in (3.30): In second order of the laser field the existing electron-hole pair can be deexcited via H_{opt}, which yields a contribution to the ground state coefficient $\alpha^{0(2,0)}$, or another electron-hole pair can be excited ($\alpha^{\mathrm{cdcd}(2,0)}$). Application of the Fröhlich Hamiltonian H_{Fr} produces combined electron-hole-phonon states ($\alpha^{\mathrm{cdb}(1,1)}$). By carrying on these considerations we arrive at the picture shown in figure 3.5, which shows the components of the state vector and the orders in which they can arise. A horizontal step requires applying the optical driving Hamiltonian H_{opt} and therefore increases the order in E by one, whereas a vertical step corresponds to an application of H_{Fr} and hence increases the order in g by one.

The equations of motion for the α-coefficients of the state components are derived essentially in the same way as demonstrated above: H_{Fr} is applied to the vertically neighbored components; H_{opt} is applied to the horizontal neighbors; and the rest of the Hamiltonian, $H_0 + H_{\mathrm{Cb}}$, is applied to the component itself. Now all contributions of the correct order are selected and by identification the equation of motion for the α-coefficient is found. This procedure is technically much easier than when correlation expansion is used because the equations of motion are less complex and they are fewer (for comparable levels of the hierarchy). The singularity in the Fröhlich coupling element $g_{\boldsymbol{q}}$ also is no problem; it can easily be seen that the singularities cancel each other in the equations of motion.

Time-dependent expectation values of the observables of interest can be directly calculated

from the state vector. Again care is taken to include only terms of certain orders. For example, the coherent phonon amplitude of the order $E^2 g^1$ (lower orders are zero) is

$$\begin{aligned}\left\langle b_{q_z \boldsymbol{e}_z}\right\rangle^{(2,1)} &= \left\langle 0\right| b_{q_z \boldsymbol{e}_z} \left|\psi^{\mathrm{b}(2,1)}\right\rangle + \left\langle \psi^{\mathrm{cd}(1,0)}\right| b_{q_z \boldsymbol{e}_z} \left|\psi^{\mathrm{cdb}(1,1)}\right\rangle \\ &= \alpha^{\mathrm{b}(2,1)}_{q_z} + \sum_{i_1 j_1 \boldsymbol{k_1}} \alpha^{\mathrm{cd}(1,0)*}_{i_1 j_1 \boldsymbol{k_1}} \alpha^{\mathrm{cdb}(1,1)}_{i_1 j_1 \boldsymbol{k_1} \boldsymbol{k_1} q_z}.\end{aligned} \tag{3.32}$$

(The exact definitions of state vector components and their coefficients are given in the appendix, section 5.4.)

We have seen in section 3.2 that the spatially averaged lattice uncertainties are fully determined by the phonon variables with vanishing wave vectors. This can be used to significantly reduce the numerical complexity of the simulations: Consider, for example, the coherent phonon amplitude in the next higher (non-vanishing) order $E^2 g^3$. Among others, it contains the term $\left\langle \psi^{\mathrm{cdb}(1,1)}\right| b_{q_z} \left|\psi^{\mathrm{cdbb}(1,2)}\right\rangle$. The state vector component $\left|\psi^{\mathrm{cdbb}(1,2)}\right\rangle$ has the general form

$$\left|\psi^{\mathrm{cdbb}(1,2)}\right\rangle = \sum_{i\,j\,\boldsymbol{k}\boldsymbol{k}'\boldsymbol{k}'' q_z q_z'} \alpha^{\mathrm{cdbb}(1,2)}_{i\,j\,\boldsymbol{k}\boldsymbol{k}'\boldsymbol{k}'' q_z q_z'} c^\dagger_{i\boldsymbol{k}} d^\dagger_{j\,-\boldsymbol{k}'} b^\dagger_{\boldsymbol{k}''+q_z \boldsymbol{e}_z} b^\dagger_{\boldsymbol{k}'-\boldsymbol{k}-\boldsymbol{k}''+q_z' \boldsymbol{e}_z} |0\rangle\,. \tag{3.33}$$

The α-coefficient depends on three two-dimensional wave vectors and two one-dimensional z-components of wave vectors. The in-plane symmetry allows us to arbitrarily choose the direction of one of the in-plane vectors, which leaves us with seven quasi-continuous degrees of freedom. Even with a rather modest discretization, the memory requirements for such matrices alone would be prohibitive. However, if only $\left\langle b_{q_z=0}\right\rangle$ is to be calculated, it suffices to know only those parts of the state vector component in which at least one of the phonon wave-vectors vanishes. We can therefore reduce it to

$$\left|\psi^{\mathrm{cdbb}(1,2)}\right\rangle = \sum_{i\,j\,\boldsymbol{k}\boldsymbol{k}' q_z} \alpha^{\mathrm{cdbb}(1,2)}_{i\,j\,\boldsymbol{k}\boldsymbol{k}' q_z} c^\dagger_{i\boldsymbol{k}} d^\dagger_{j\,-\boldsymbol{k}'} b^\dagger_{\boldsymbol{k}'-\boldsymbol{k}+q_z \boldsymbol{e}_z} b^\dagger_0 |0\rangle\,, \tag{3.34}$$

which has only four quasi-continuous degrees of freedom, just like the lower-order component $\left|\psi^{\mathrm{cdb}(1,1)}\right\rangle$ where the phonon wave vector is not restricted to $q = 0$. This basically means we get the next higher order in g almost without any additional numerical effort. In passing, this reduction also resolves the technical difficulty that the state in (3.33) does not unambiguously define its α-coefficient because of the interchangeability of the phonon operators.

In this way the coherent phonon amplitude $\left\langle b_{q_z=0}\right\rangle$ can be calculated up to the order $E^2 g^3$ and the lattice uncertainties up to the order $E^2 g^4$. The state vector components and their equations of motion can be found in the appendix (section 5.4).

3.4.2 Spin degree of freedom

So far the spin degree of freedom has been left out. We could in principle include it in the same way as in correlation expansion, i.e., by inserting factors of two in the appropriate places. As long as the calculations are restricted to second order in the laser field an easier alternative exists: In this case the two possible spin configurations e↑h↓ and e↓h↑ are not coupled and just exist side by side (any coupling would only be visible in observables of higher order). Therefore the electronic densities can simply be understood as the combined densities of both spin configurations and no changes to the equations of motions are necessary. This will of course no longer work if higher orders in E are considered.

3.4.3 Truncating the hierarchy

The hierarchy caused by the Fröhlich interaction is truncated by omitting terms above a certain order in the phonon coupling strength g. Whereas the expansion in the laser strength E can be justified by using only low driving strengths, the phonon coupling for a given material has a fixed strength that cannot easily be changed. However, we can check whether the chosen maximal order in g is sufficient by comparing to calculations with the next lower order; small differences are a good indication that higher orders would have negligible effects. In this way we will later see that in our model under the most relevant excitation conditions even the lowest non-vanishing order in g suffices.

The cut-off at a certain order in the laser strength E is necessary because the optical driving Hamiltonian also produces an infinite hierarchy: State vector components with n electron-hole pairs are connected to components with $n+1$ and $n-1$ (if $n \geq 1$) pairs. We limit observables to the order E^2, which means that only effects linear in the laser intensity are included. In particular this neglects Pauli blocking. No such approximation is necessary with correlation expansion, because optical driving does not lead to higher-order density matrices that would need to be factorized; hence effects like Pauli blocking are fully included in correlation expansion. Correlation expansion calculations for the electronic subsystem have been used to verify that the simulation parameters are within the linear driving regime.

The situation is exactly reversed for Coulomb interaction, which causes an infinite hierarchy in correlation expansion while it does not do so here: Because the Coulomb Hamiltonian preserves the number of electron-hole pairs, any state vector component is only connected to itself. Nevertheless, calculating the Coulomb effects takes the bulk of the time needed for the simulations, just as it does in correlation expansion when the Coulomb Hamiltonian is not replaced by its mean-field approximation. With order separation it does not make much sense to use that approximation: doing so would again create a hierarchy because the number of electron-hole pairs is no longer conserved. Even worse, truncating that hierarchy with the help of the expansion in E affects only some parts of the state vector but leaves other untouched. In particular the component $\left|\psi^{\mathrm{cdb}(1,1)}\right\rangle$ would not experience any Coulomb effects. Therefore in all calculations in this chapter the Coulomb Hamiltonian is used without the mean-field approximation. The numerical complexity still is manageable because only state vector components with at most one electron-hole pair are considered, so the Coulomb interaction is restricted to electron-hole attraction.

3.4.4 Comparison with other hierarchy-truncation schemes

The biggest disadvantage of order separation is that it is inherently bad at predicting the correct energies (or oscillation frequencies) of the states of the system as soon as some energy renormalization is involved. In our case energy renormalization occurs, for example, due to Fröhlich interaction and polaron formation. In correlation expansion, energy renormalization is expressed by the back-action of a density matrix on itself: the density matrix enters in its own equation of motion, and the so-called self-energy matrices that facilitate this back-action can be interpreted as an energy renormalization [53]. With order separation this is not possible: Because it is mediated by the Fröhlich interaction, the back-action equivalent term is of higher order and therefore enters only in the equation of motion of a higher-order variable, whose

back-action then again is imprinted on an even higher order. This means that rather high orders will be needed to correctly describe energy renormalization.

However, deviations from the correct energies become noticeable only after a time dictated by the energy-time uncertainty. We are interested in simulations on very short time-scales where the exact frequency of oscillations is of secondary importance. For the calculation of the time-dependent dynamics order separation hence still is a good choice.

Correlation expansion is not the only other hierarchy-truncation scheme. Dynamics-controlled truncation (DCT) is a similar approach in which care is taken to include all terms that are below a certain minimal order in the laser strength [3]. It ensures that the calculated response is exact up to the chosen order, but just like correlation expansion it also includes some higher-order terms. In order separation all results also are exact up to the chosen order, but higher orders are set to zero. In this sense, order separation carries the DCT scheme to its extreme, but on the way loses much of the ability to describe energy renormalization.

Another truncation scheme works by omitting states that have a certain minimum amount of (quasi-) particles [9]. The equations of motion are set up within density matrix theory in the usual way, but instead of correlations the full density matrices are used as dynamical variables. Similar to correlation expansion, matrices above a certain number of operators are then set to zero. The distinction is that in correlation expansion an arbitrarily large number of particles can exist, only their correlation is lost. If there are only few electronic states, this truncation scheme allows to derive a set of generalized equations of motion that applies to all orders simultaneously. Higher-order terms are included in this scheme unless they require density matrices above the particle limit. Similarly, order separation also enforces a limit to the maximum number of particles.

The main reason why order separation is used in this work is its ability to calculate the lattice uncertainties. The unphysical uncertainties we observed with correlation expansion, which have been traced back to the mixing-in of higher orders, are nonexistent with order separation. Also, no tricks are necessary to cancel the singularities originating from the phonon coupling element.

3.4.5 Density matrix formulation

The state vector formulation requires a pure state as the initial state. So far we have assumed that the initial state is the ground state, which for our system is a very good approximation at low temperatures; for example, the population number of optical phonons ($\hbar\omega_{\mathrm{LO}} = 36.3\,\mathrm{meV}$) at liquid Helium temperature (4 K) is $n_{\mathrm{B}} = 1.8 \cdot 10^{-46}$. At elevated temperatures, the initial state is a thermal state with some population of optical phonons. The state vector formulation could in principle still be used for thermal states by performing a separate simulation for each pure-state component of the mixed state, but this obviously would multiply the computational effort required. In such cases it is easier to apply order separation to the density matrix formulation, which will directly allow mixed states.

The equations of motions are derived from the usual ones from density matrix theory with correlation expansion, but without setting any correlations to zero. Each density matrix is furnished with an additional index that gives its order in E and g, and again only contributions to the equations of motion that are of the correct order are considered. For example, the equation

of motion for the coherent phonon amplitude B_{q_z} in the lowest non-vanishing order $E^2 g^1$ reads

$$\mathrm{i}\hbar\frac{\mathrm{d}}{\mathrm{d}t}B^{(2,1)}_{q_z} = \hbar\omega_{\mathrm{LO}}B^{(2,1)}_{q_z} + 2^*\sum_{i_1 i_2 \boldsymbol{k}_1} g^{*i_1 i_2}_{q_z} f^{\mathrm{e}(2,0)}_{i_2 i_1 \boldsymbol{k}_1} - 2^*\sum_{j_1 j_2 \boldsymbol{k}_1} g^{*j_2 j_1}_{q_z} f^{\mathrm{h}(2,0)}_{j_2 j_1 \boldsymbol{k}_1}. \tag{3.35}$$

In this case the equation of motion is the same as its equivalent in correlation expansion, just with additional order indices. In general the equations are very similar to correlation expansion, although many terms will be missing because their order is too high.

The initial thermal population of optical phonons enters into the equations of motion via the zeroth-order density matrix $\delta\langle b^\dagger_{\boldsymbol{q}} b_{\boldsymbol{q}'}\rangle^{(0,0)} = \delta_{\boldsymbol{q},\boldsymbol{q}'} n_{\mathrm{B}}$. For the phonon-assisted correlations, for example, this produces an additional driving term (with $\boldsymbol{q} = \boldsymbol{k}' - \boldsymbol{k} + q_{\mathrm{z}}\boldsymbol{e}_{\mathrm{z}}$):

$$\mathrm{i}\hbar\frac{\mathrm{d}}{\mathrm{d}t}\delta s^{\mathrm{e}(2,1)\,i i'}_{\boldsymbol{k}\boldsymbol{k}' q_z}\Big|^{H_{\mathrm{Fr}},\mathrm{th}} = n_{\mathrm{B}}\sum_{i_1}\left(g^{*i_1 i'}_{\boldsymbol{q}} f^{\mathrm{e}(2,0)}_{i i_1 \boldsymbol{k}'} - g^{*i i_1}_{\boldsymbol{q}} f^{\mathrm{e}(2,0)}_{i_1 i' \boldsymbol{k}}\right) \tag{3.36}$$

The full set of equations of motion for the lowest non-vanishing orders is given in the appendix (section 5.4.2). Higher orders are not considered because their derivation is rather involved in the density matrix formulation and we will see that the lowest non-vanishing orders in many cases are sufficient. The numerical simulations can again be simplified if only the phonon variables in the limit of vanishing wave vectors are calculated.

3.4.6 Decoherence

As in the previous chapter, the calculations do not account for additional decoherence processes like lattice anharmonicities or interaction with the quantized electromagnetic field. For coherent phonon states, the decoherence time is experimentally known to be an order of magnitude larger than the timescale of the simulations ($\approx 9\,\mathrm{ps}$ decay time in GaAs at 6 K) [59]. This can be taken as an indication that the decoherence time for squeezed states also is large enough to be neglected. However, coherent lattice oscillations are known to be relatively stable; for example, it has been shown for a harmonic chain that almost all states under quite general conditions eventually develop into generalized coherent states (states with a Gaussian Wigner function) [58]. In the language of einselection, coherent states are preferred states that are einselected by interaction with the environment [62]. Therefore squeezed states could possibly be more susceptible to decoherence, and experiments will be needed to ascertain the actual dephasing time of squeezed states.

3.5 Producing squeezed phonons

We now discuss under which excitation conditions squeezed phonon states are created. For that purpose, the squeezing factors S_U and S_P are defined as the relative change of the uncertainty with respect to its value in thermal equilibrium at $T = 0$:

$$S_U = \frac{(\Delta U_z)^2 - (\Delta U_z)_0^2}{(\Delta U_z)_0^2}, \qquad S_P = \frac{(\Delta P_z)^2 - (\Delta P_z)_0^2}{(\Delta P_z)_0^2} \tag{3.37}$$

If a squeezing factor becomes negative, this means the uncertainty is squeezed below its zero-point value; the lowest possible value is -1, which is only reached when the corresponding uncertainty vanishes. Positive values indicate an increased uncertainty.

The uncertainty principle for the squeezing factors reads $(S_U + 1)(S_P + 1) \geq 1$. We will see that the changes in the uncertainties are relatively small, i.e., $|S_U|$ and $|S_P|$ are much smaller than one. In this case the uncertainty principle can be approximated as

$$S_U + S_P \geq 0. \tag{3.38}$$

3.5.1 Effects of a single Gaussian pulse

Even a simple Gaussian pulse can, under certain conditions, induce squeezing. Figure 3.6 shows the minimum value of the squeezing factors between 0.2 ps and 0.6 ps after excitation with a Gaussian pulse with central energy and temporal width as indicated on the horizontal and the vertical axis, respectively. Blue shades signify squeezing, i.e., the uncertainty of lattice displacement (upper parts in the figure) or momentum (lower parts) drops below its zero-point level for some point in time. The strength of the pulse is adjusted (individually for each point) to produce a peak electron-hole pair density of $10^{10}\,\mathrm{cm}^{-2}$.

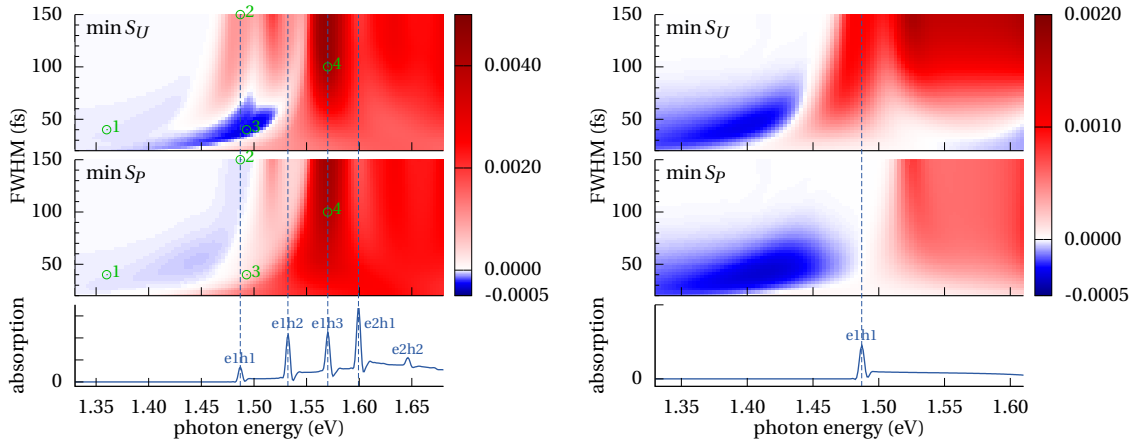

(a) full model with two electron and three hole subbands [parameter set C (spectrum: C_s)]

(b) reduced model with only two subbands [parameter set C_r (spectrum: C_{r+s})]

Figure 3.6: Minimum values of squeezing factors (color-coded) after excitation with a single optical pulse of varying photon energy (horizontal axis) and temporal width (vertical axis). The lower parts show the absorption spectrum for reference.

We first look at part (b) of the figure, which is easier to interpret as the model here has been reduced to one electron and one hole subband only. Short pulses below the band gap produce squeezed states. If the pulse is too long (but still below the band gap), the phonon subsystem can adapt adiabatically to the changes induced by the pulse and therefore returns to its ground state after the pulse, i.e., the uncertainties are neither reduced nor increased. If the photon energy is high enough, incoherent phonons are produced, which increases the uncertainties. This process is particularly efficient when the excitation occurs one LO phonon energy above the exciton line. For the momentum uncertainty, the threshold between squeezing and increased uncertainty lies approximately at the exciton line. For the displacement uncertainty, it is shifted to lower energies, approximately to the place where the pulse leaves behind some residual carriers that shift the lattice equilibrium position. The small blue-shaded area for very high photon energies visible in the S_U plot is a numerical artifact caused by the k-space cutoff and goes away when the cutoff is shifted to higher energies.

The general behavior is similar within the more complete model with two electron and three hole subbands, as shown in figure 3.6a. However, a new region of squeezed lattice displacement emerges for short pulses that extends almost to the e1h2 exciton line (around point 3 in the figure). In addition, lattice momentum becomes squeezed for long pulses on the lowest transition (point 2). Pulses centered on the e1h3 transition strongly increase both uncertainties (point 4). Squeezing by impulsive excitation (e.g., point 1) is smaller than in the reduced model because part of the carrier density is distributed to higher subbands which produces less charge separation. We will now discuss each of the points marked in the figure in more detail.

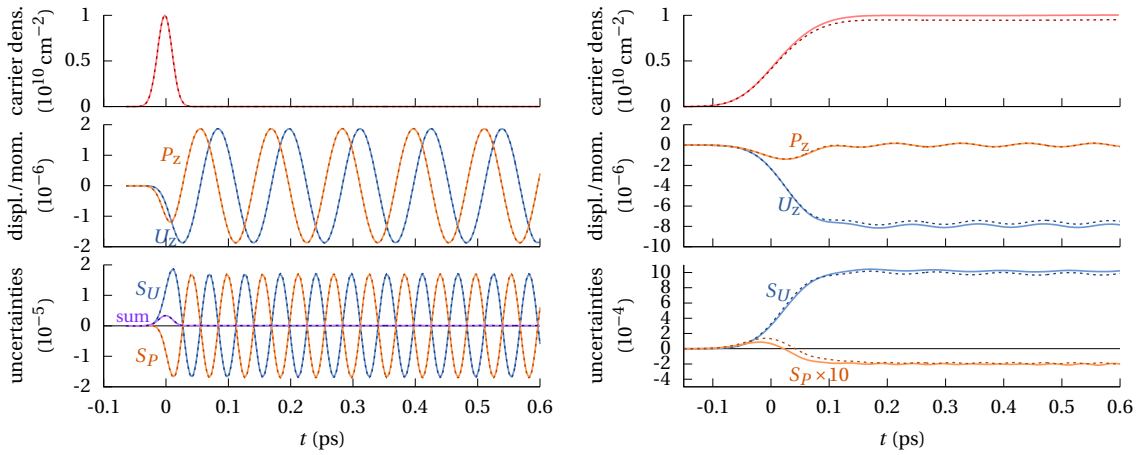

(a) Generation of a squeezed state by a short pulse below the band gap (point 1 in figure 3.6a: 40 fs, 1.360 eV).

(b) Continuously squeezed momentum after an energetically sharp pulse on the lowest exciton line (point 2: 150 fs, 1.487 eV).

Figure 3.7: Time-dependent dynamics after excitation with a single pulse. Both parts of this figure show the electron-hole pair density (top), the mean values of lattice displacement and momentum (center), and the squeezing factors (bottom). Overlaid are darker, dashed lines from a calculation of higher maximal order. [parameter set C]

In figure 3.7a the quantum well is impulsively excited by a short pulse below the band gap (point 1 in figure 3.6a). As we have already seen when discussing impulsive driving of coherent phonons (section 2.4.1), this yields a transient carrier density and a coherent lattice oscillation

around the unperturbed equilibrium position. The plot of the squeezing factors reveals that the state is squeezed. Lattice displacement and momentum uncertainty oscillate with twice the LO phonon energy and in turn fall below their zero-point levels. The sum $S_U + S_P$ after the pulse is almost zero, which means that the state has a minimal uncertainty product and hence is very similar to the prototypical squeezed state [40]. The carrier density vanishes again after the pulse, which experimentally is an advantage when measuring the lattice uncertainties because in particular optical measurements are also susceptible to changes in the electronic subsystem.

The plots show the results of a lower-order calculation with lines of lighter colors and a higher-order calculations with darker, dashed lines. Lower order means $E^2 g^0$ for the carrier density, $E^2 g^1$ for the mean values of lattice displacement and momentum, and $E^2 g^2$ for the squeezing factors. This level has also been used for the color-coded squeezing maps above. The higher-order calculation has maximal orders $E^2 g^2$, $E^2 g^3$, and $E^2 g^4$, respectively. Because the next higher orders vanish, the lowest orders not included for the squeezing variables are E^4 and g^6. For impulsive driving conditions, the agreement between lower and higher order is almost perfect.

An energetically sharp pulse centered on the lowest exciton line (point 2 in figure 3.6a) is able to squeeze lattice momentum for a continued time, as demonstrated in figure 3.7b: While the displacement uncertainty experiences a strong increase, the momentum uncertainty is lowered by a small amount below its zero-point value and stays there. Such an effect would clearly not be possible within a system of uncoupled harmonic modes (freely propagating light, for example). The reduced momentum uncertainty is sustained by the persistent changes induced by the displacive driving, which is also reflected in the carrier density left behind and in the shift of the lattice equilibrium position. There is a small impulsive part to the excitation due to the higher-energy transitions, which also is necessary to produce the squeezed state.

Again the higher-order calculation produces only small differences. Those are mainly caused by a small renormalization of the exciton energy, leading to a slightly smaller total carrier density.

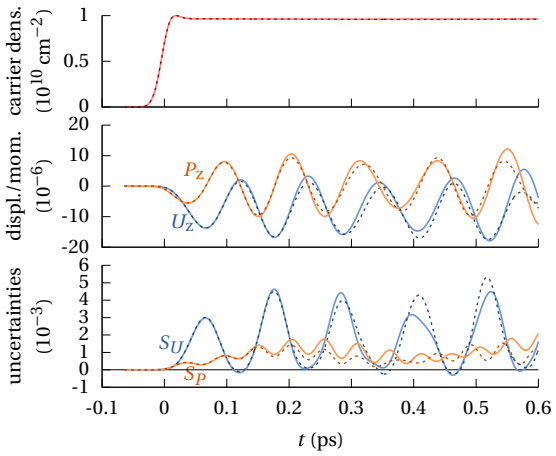

Figure 3.8: Transient displacement squeezing after a short pulse directly above the lowest exciton line (point 3: 40 fs, 1.493 eV).

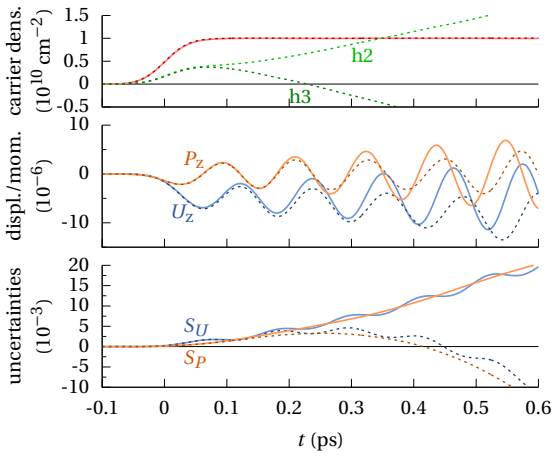

Figure 3.9: Large incoherent phonon generation after an energetically sharp excitation on the e1h3 exciton line (point 4: 100 fs, 1.570 eV).

The squeezing map of figure 3.6a suggests to look at short pulses around the lowest exciton line (point 3) when displacement squeezing is desired. The corresponding time-dependent

data is plotted in figure 3.8. We again see a mostly displacive excitation with a small impulsive component. The displacement uncertainty oscillates wildly and randomly dips below its zero-point level. Compared to the previous situations, the amplitude of the oscillation is much larger, and the seemingly small dips below zero are actually quite large when considering absolute values. However, the oscillation is rather irregular and the uncertainty in between points of squeezing reaches large values. Lower-order and higher-order calculation differ noticeably for some times larger than 0.2 ps, but they agree on the strength of squeezing that is achieved.

Incoherent phonon generation is very effective when the e1h3 line is excited (point 4 in figure 3.6a and figure 3.9) because the e1h2 transitions lies approximately one LO phonon energy below. Accordingly both uncertainties increase fast, and the coherent lattice variables show signs of resonant driving. The higher-order calculation develops very differently from the calculation of lower order and produces unphysical results: after 0.45 ps the uncertainty product violates the Heisenberg uncertainty principle, and even sooner the h3 subband population becomes negative. Evidently terms of higher order than included in the simulation would be needed to obtain reliable results. The reason is that down-relaxation of holes under emission of incoherent phonons is very efficient and therefore high orders in the phonon coupling g are quickly gaining importance. Here order separation clearly is not applicable, which is not too bad because obviously no squeezed state can be produced under these circumstances.

3.5.2 Two-pulse excitation

In simulations of a quantum dot driven by ultrashort laser pulses resonant with the lowest exciton transition, no squeezing was found after single-pulse excitation, but a sequence of two pulses in some cases produced squeezed states [54]. Therefore we will now investigate the applicability of two-pulse sequences for creating squeezed phonons in a quantum well.

The two-pulse sequence is modeled by the electric field (cf. (1.12))

$$\boldsymbol{E}(t) = \boldsymbol{E}_0 \cdot 2\,\mathrm{Re}\left[\mathrm{e}^{-4\ln(2)\,t^2/\tau^2}\mathrm{e}^{-\mathrm{i}\omega_0 t} + \mathrm{e}^{-4\ln(2)\,(t-t_0)^2/\tau^2}\mathrm{e}^{-\mathrm{i}(\omega_0 t+\varphi)}\right], \tag{3.39}$$

with the delay time t_0 and an additional phase φ. In this definition, a simple delay line would yield a phase of $\varphi = -\omega_0 t_0$. The FWHM of the pulses is in this section set to a fixed value of $\tau = 70$ fs. The central frequency is matched to the e1h1 exciton line, $\hbar\omega_0 = 1.487$ eV, and the amplitude E_0 is again chosen to create a peak carrier density of $10^{10}\,\mathrm{cm}^{-2}$.

The squeezing map for varying delay time and phase is shown in figure 3.10, where the color indicates the minimum values of the squeezing factors between 0.3 ps and 0.6 ps. In the reduced model in part (b) of the figure, displacement is never squeezed, but the map of the momentum uncertainty displays a checkered pattern of tiles with squeezed and with increased uncertainty. The pattern is approximately periodic with the LO phonon oscillation period $T_{\mathrm{LO}} = 114$ fs. The behavior of the momentum uncertainty is very similar to the quantum dot model [51, 54], and can be understood with the help of a Wigner function depiction [52]. However, in the quantum dot case the displacement uncertainty could also be squeezed. Including more subbands (figure 3.10a) primarily changes two things: the tiles in the map of momentum squeezing merge diagonally to form a striped pattern, and a new region of squeezed displacement develops.

The dynamics of momentum squeezing in the reduced model (point 3 in figure 3.10b) is shown in figure 3.11. Both pulses add to the carrier density and thereby displace the lattice

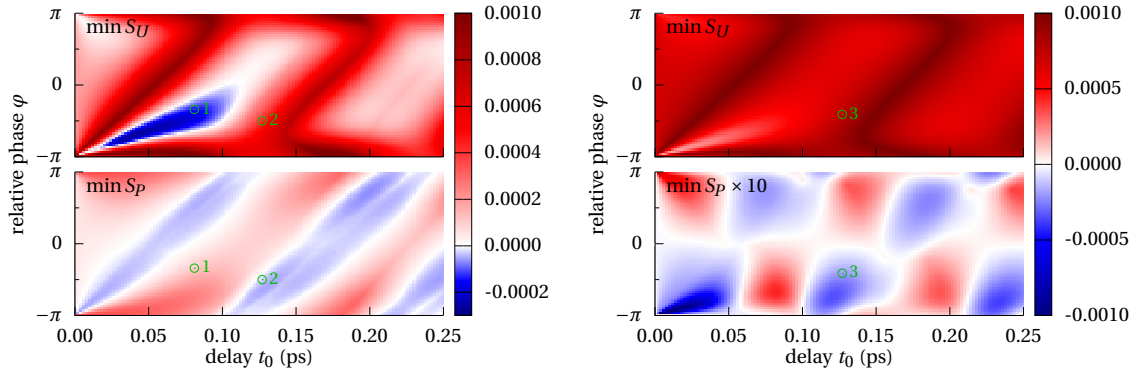

(a) two electron, three hole subbands [parameter set C]

(b) two subbands only [parameter set C_r]

Figure 3.10: Squeezing map for two-pulse excitation, with pulse delay on the horizontal axis and relative phase between pulses on the vertical axis. The 70-fs pulses are resonant with the lowest exciton line.

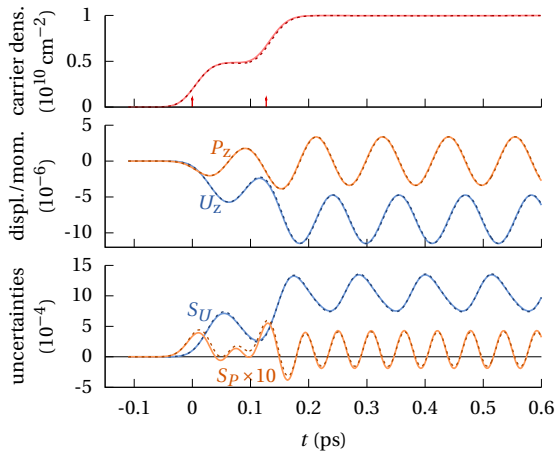

Figure 3.11: Squeezing of lattice momentum by a two-pulse excitation in the reduced model. Pulse delay is 127 fs, relative phase is -0.41π for the calculation of lower maximal order and -0.55π for the higher-order results (point 3 in figure 3.10b). [parameter set C_r]

equilibrium position. As a result, displacement uncertainty is strongly increased and oscillates above the zero-point limit. Momentum uncertainty oscillates with a much smaller amplitude (it is magnified by a factor of ten in the plot), but part of the oscillation breaks the zero-point limit. The frequency is the doubled phonon frequency, whereas the oscillation of the displacement uncertainty is dominated by the single phonon frequency.

Lower-order and higher-order calculations agree quite well, but the phase of the second pulse had to be modified. The reason is this: The exact solution of the quantum dot model tells us that the relevant phase is $\tilde{\varphi} = \varphi + \omega_0 t_0 - \omega_X t_0$, i.e., it has to be defined relatively to the phonon-renormalized exciton transition energy $\hbar\omega_X$ [54]. The laser frequency ω_0 has been set to the exciton frequency ω_X in the lower-order calculation, but in the higher-order calculation the exciton frequency is renormalized to a slightly smaller value ω'_X, which means that φ also has to be decreased to the new value $\varphi' = \varphi + (\omega'_X - \omega_X)\, t_0$. A good agreement between lower and higher order is obtained with $\varphi' - \varphi = -0.14\pi$, which corresponds to a shift of the exciton energy of $\hbar(\omega'_X - \omega_X) = -2.3\,\text{meV}$. That value for the energy renormalization has also been used for the subsequent calculations.

Momentum squeezing with more subbands included under similar excitation conditions

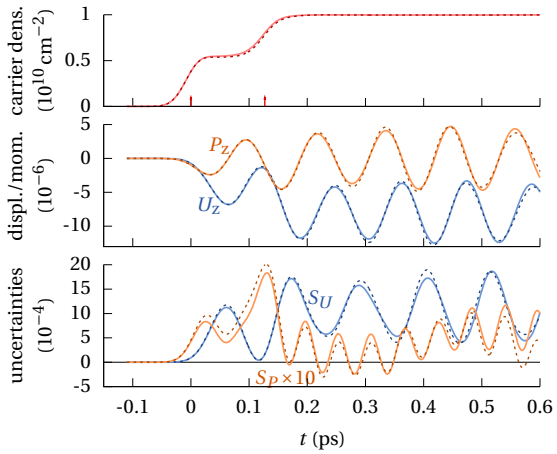

Figure 3.12: Momentum squeezing after two-pulse excitation (point 2 in figure 3.10a: delay 127 fs, phase -0.50π (higher order: -0.64π)).

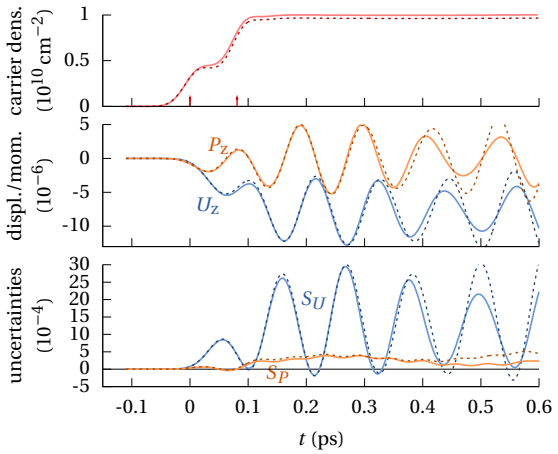

Figure 3.13: Short-time squeezing of lattice displacement induced by two-pulse excitation (point 1 in figure 3.10a: delay 81 fs, phase -0.34π (higher order: -0.43π)).

(point 2 in figure 3.10a) is displayed in figure 3.12. The general behavior is not very different and again momentum squeezing occurs, but it is restricted to short times after which the oscillation of S_P is shifted upwards. In the higher-order calculations, momentum squeezing returns at approximately 0.56 ps.

The rather strong squeezing of lattice displacement that is prominently visible in the two-pulse squeezing map (point 1 in figure 3.10a) bears similarities to the single-pulse situation. As seen in figure 3.13, lattice squeezing again is strong in absolute values for brief spaces of time, but it is accompanied by a large oscillation of the squeezing factor S_U that for most times lies far above the zero-point limit.

The agreement between lower and higher order is worse when more subbands are included than in the case with only one transition. The reason is that the correction of the phase is adjusted to the lowest transition only. However, especially for short times the deviations are not too large, which indicates that the higher-order calculations provide reliable results for the time-scale depicted in the plots.

3.5.3 Elevated temperatures

At temperatures above zero, there is an initial population of optical phonons determined by the Bose distribution

$$\left\langle b^\dagger_{\alpha,\boldsymbol{q}} b_{\alpha,\boldsymbol{q}} \right\rangle_{\mathrm{th}} = n_{\mathrm{B}} = \frac{1}{\exp\left[\frac{\hbar\omega_{\mathrm{LO}}}{kT}\right] - 1}, \tag{3.40}$$

where T is the absolute temperature and k is the Boltzmann constant. The uncertainties of lattice displacement and momentum are thereby raised to the new value

$$(\Delta U_z)^2_{\mathrm{th}} = (\Delta P_z)^2_{\mathrm{th}} = (1 + 2n_{\mathrm{B}})(\Delta U_z)^2_0. \tag{3.41}$$

The Bose temperature of the optical phonons is $\hbar\omega_{\mathrm{LO}}/k = 421\,\mathrm{K}$, and hence the temperature can be relatively high before it noticeably affects the results. For example, the squeezing map for

single-pulse excitation (figure 3.6a) looks almost exactly the same at $T = 80\,\mathrm{K}$ with $n_\mathrm{B} = 5.2 \cdot 10^{-3}$. In this section the temperature is therefore set to room temperature ($T = 293\,\mathrm{K}$), where the population of optical phonons is $n_\mathrm{B} = 0.31$ and the uncertainties are increased by a factor of 1.62 compared to the ground state. For comparison we use calculations with $T = 4\,\mathrm{K}$ ($n_\mathrm{B} = 1.8 \cdot 10^{-46}$), which are virtually identical to the results for zero temperature.

We have already seen that the reduction of uncertainty that can be achieved is much smaller than the thermal increase at higher temperatures, and hence we cannot expect to lower the uncertainties below their zero-point level when starting with the quantum well at room temperature. For this reason we define the thermal squeezing factors $\tilde{S}_U$ and $\tilde{S}_P$ relative to the uncertainties in thermal equilibrium:

$$\tilde{S}_U = \frac{(\Delta U_\mathrm{z})^2 - (\Delta U_\mathrm{z})^2_\mathrm{th}}{(\Delta U_\mathrm{z})^2_\mathrm{th}}, \qquad \tilde{S}_P = \frac{(\Delta P_\mathrm{z})^2 - (\Delta P_\mathrm{z})^2_\mathrm{th}}{(\Delta P_\mathrm{z})^2_\mathrm{th}} \tag{3.42}$$

Negative values indicate thermal squeezing, i.e., a reduction of the uncertainty below its value at equilibrium. At zero temperature this obviously coincides with the definition of the usual squeezing factors (3.37).

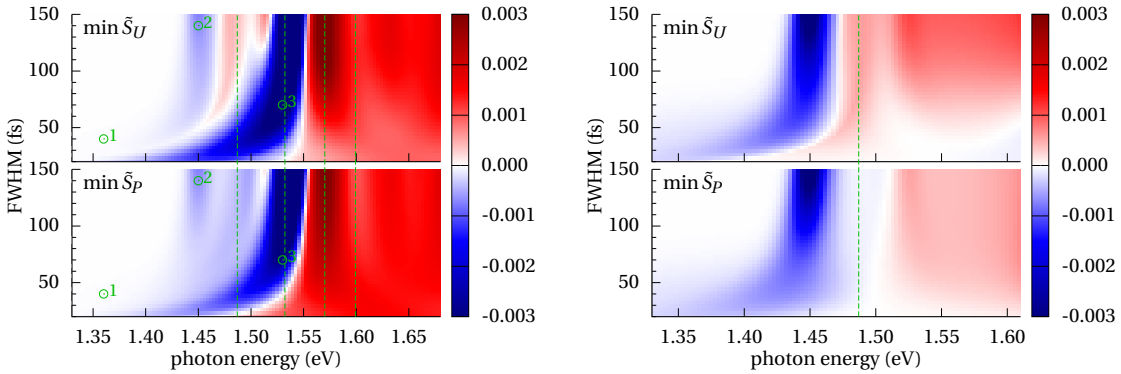

(a) two electron and three hole subbands [parameter set C]

(b) two subbands only [parameter set $\mathrm{C_r}$]

Figure 3.14: Thermal squeezing at 293 K after excitation with a single optical pulse of varying photon energy (horizontal axis) and temporal width (vertical axis). Green lines indicate the position of exciton transitions.

The squeezing map for single pulses in the reduced model at room temperature (figure 3.14b) is not dissimilar to its low-temperature equivalent (figure 3.6b). The main difference is a new region approximately one LO phonon energy below the exciton line (i.e., around the Stokes line) where both displacement and momentum become strongly squeezed; the squeezing is strongest with long pulses whose energy is well-defined. In this region the photon energy is too low to directly drive the exciton transition. Instead photon absorption can only take place when the missing energy is supplied by phonons. In this way incoherent thermal phonons are absorbed, which reduces the uncertainty of both lattice displacement and momentum. The same effect is also seen in the model with several subbands (figure 3.14a). However, here we have an additional region of even stronger squeezing around the e1h2 transition, which lies about one phonon energy below the e1h3 line.

Figure 3.15 shows the dynamics after an impulsive excitation below the band gap (point 1 in figure 3.14a). The differences to the low-temperature case are rather small. Actually, the

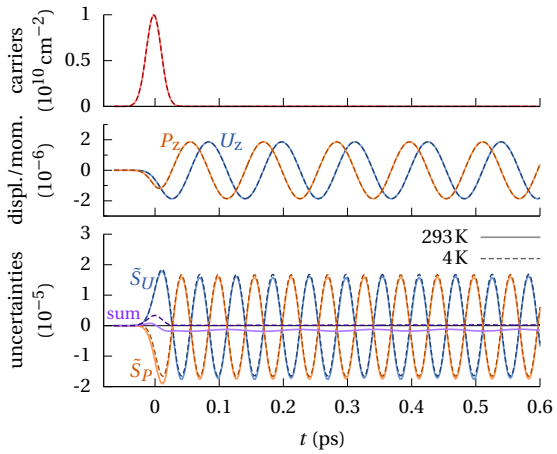

Figure 3.15: Thermal squeezing after impulsive excitation (point 1 in figure 3.14a: 1.360 eV, 40 fs).

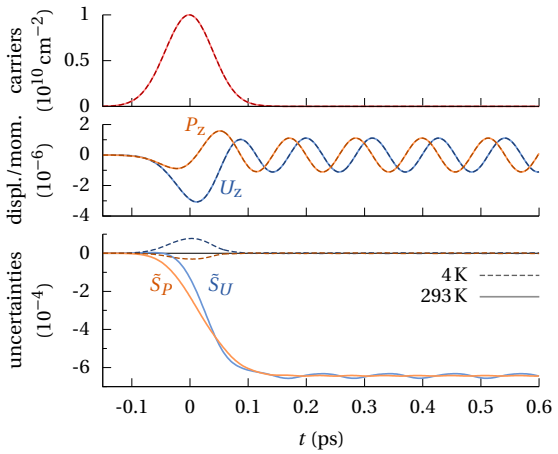

Figure 3.16: Absorbing incoherent phonons reduces the uncertainties (point 2: 1.450 eV, 140 fs).

uncertainties oscillate with a larger amplitude, but this is compensated by the increased thermal uncertainty in the squeezing factors (3.42). We also observe a small downward shift of the oscillation, which is best visible in the sum of the uncertainties. The sum is negative after the pulse, which means that the uncertainty product has been slightly reduced compared to its initial value.

In figure 3.16 the quantum well is excited with an energetically sharp pulse on the Stokes line (point 2 in Fig. 3.14a). At low temperatures, the system after the pulse returns to its ground state, except for a small coherent oscillation created by the impulsive driving. At room temperature, where a thermal population of optical phonons exists, some incoherent phonons are consumed to provide the missing energy for creating electron-hole pairs. Both uncertainties are reduced to approximately the same value and afterward oscillate faintly. We do not see any residual population of charge carriers after the pulse, although our interpretation of the squeezing process suggests that for each incoherent phonon absorbed an electron-hole pair should stay behind. The explanation is that the order $E^2 g^0$ in which the carrier population is calculated is obviously not sufficient to observe this effect, and even if higher orders were included it would still be too small to be visible in this plot.

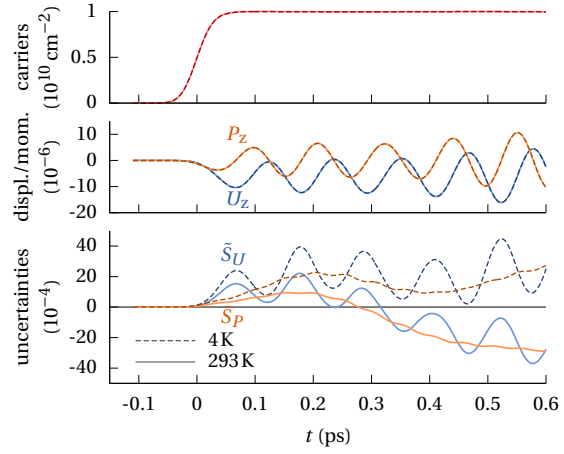

Figure 3.17: Thermal squeezing after excitation with a pulse of relatively high energy (point 3 in figure 3.14a: 1.530 eV, 70 fs).

The effect of strong squeezing after excitation close to the e1h2 transition (point 3 in figure 3.14a) can be seen in figure 3.17. The squeezing factors for cryogenic and room temperatures develop similarly, but for the higher temperature they are gradually shifted downwards. Squeezing is achieved only after the pulse has subsided. Obviously the h3 subband, whose energy difference to the h2 subband is about the optical phonon energy, is required for the squeezing effect; when it is switched off, the squeezing factors stay above zero. The initial increase of the uncertainties can in the same way be traced back to relaxation into the lower-lying h1 subband.

4 Conclusions

We have seen simulations of the lattice dynamics in a quantum well driven by short laser pulses; in particular, how the dynamics is calculated quantum-kinetically, how the simulations can be used to explain the excitation mechanisms of coherent lattice oscillations, and how squeezed phonon states can be generated.

The simulations are built upon a microscopic model of a GaAs/AlAs quantum well, consisting of all the different parts necessary to realistically describe the coupled electron-phonon dynamics: the electronic subband structure including Coulomb interaction between charge carriers, driving by a coherent laser field, and the longitudinal-optical (LO) phonon branch and its coupling to the electrons. For the calculations, two variants of density matrix theory have been used: Correlation expansion proved to be well-suited to calculate the generation of coherent and incoherent phonons and the energy transfer to the lattice. It experiences problems when lattice uncertainties are to be determined; this was traced back to the mixing of terms of different orders in the phonon coupling. The partial inclusion of higher orders is in many cases desirable because it, for example, allows to better estimate energy renormalizations, but here it also causes unphysical results for the uncertainties. Therefore another hierarchy truncation scheme was introduced that keeps different orders strictly separated and is able to calculate the lattice uncertainties. This scheme also has a state vector formulation, which is easier to derive than the density matrix formulation and permits a straightforward physical interpretation, but is limited to pure states.

Several mechanisms exist by which coherent phonons can be generated. A short pulse below the band gap creates a transient electronic population that exerts an impulsive force on the lattice, which starts to oscillate around its equilibrium with a sine-like phase. Pulses above the band gap shift the equilibrium position of the lattice, which if done fast enough also yields an oscillation of the lattice; the phase is not necessarily cosine-like as a simple model would suggest. Particularly strong lattice oscillations are generated by an electronic quantum beat whose frequency is matched to the LO phonon frequency. The quantum beat is between two exciton lines, whose splitting can be tuned by an external electric field via the quantum confined Stark effect. An oscillating charge distribution results that resonantly drives the lattice oscillation. The resonant generation mechanism is characterized by resonances in the strength of the external field and in the photon energy of the laser. The simulations successfully produce these characteristics that have also been seen in experiments. In addition they show that most of the energy transferred to the lattice does not go into coherent phonons but instead creates incoherent phonons, which are invisible in experiments that do not measure the uncertainties.

When calculating the lattice uncertainties it is important to take into account the spatial averaging that is inherent to any measurement. The extent of the averaging strongly influences the uncertainties; in fact, even relatively strong lattice oscillations would be completely drowned in zero-point fluctuations if the relative displacement of a single Ga-As pair was recorded and not an average over many. For realistic values of the averaging extent, the zero-wavevector mode alone determines the experimentally accessible uncertainties. Different excitation conditions

lead to differently squeezed states: An impulsive excitation below the band gap leaves behind a state that very much resembles the prototypical squeezed state; displacement and momentum uncertainty oscillate around their zero-point values and the uncertainty product is almost at its minimum. For an experimental verification, an additional advantage is that the carrier density after the pulse is very small and hence cannot act as a stray influence on the measurement of the uncertainties. Other single-pulse excitations produce a sustained squeezing of the momentum uncertainty, or an oscillation of the displacement uncertainty with a large amplitude and short-time squeezing. Two-pulse excitations evoke a behavior that in some respects is similar to what has been found for the model of a quantum dot. Here, too, squeezing is possible under the right circumstances. At elevated temperatures thermal noise increases the uncertainties. An impulsive excitation results in an oscillation of the uncertainties which is now centered around the thermal equilibrium, and whose amplitude is increased by the same factor as the thermal increase of the uncertainties. By exciting the quantum well with a laser pulse tuned to an energy that is below the band gap by one phonon energy, incoherent thermal phonons can be absorbed, which reduces the uncertainty of both lattice displacement and momentum.

The absolute value of the reduction of the uncertainties compared to their zero-point or thermal level is very small. It can be increased by going to higher carrier densities or by using a well material like ZnSe in which phonon coupling is stronger, but still it is apparent that a substantial reduction as achieved with squeezed light cannot be reached; for stronger squeezing it might be worthwhile to consider nano-mechanical oscillators, a field of study that lately has seen a lot of progress. The relatively small values of squeezing ultimately are a result of a rather weak coupling between lattice and electronic subsystem, and therefore it would also be interesting to model the measurement of the lattice uncertainties as a weak measurement.

5 Appendix

5.1 Parameters

5.1.1 Material parameters for GaAs/AlAs wells

parameter	value	source
GaAs (well)		
band gap (Γ point)	$E_g^A = 1.52\,\mathrm{eV}$	Adachi [1], p. 138
effective masses at Γ point (in units of the free electron mass m_0)		
electron	$m_e^A = 0.067\,m_0$	*ibid.*, p. 234
heavy hole	$m_h^A = 0.55\,m_0$	*ibid.*, p. 254
static dielectric constant	$\varepsilon_s = 12.69$	*ibid.*, p. 118
high-frequency dielectric constant	$\varepsilon_\infty = 10.89$	*ibid.*, p. 115
lattice constant	$a = 0.565\,\mathrm{nm}$	*ibid.*, p. 15
LO phonon frequency at Γ point	$\omega_{LO} = 36.3\,\mathrm{meV}$	*ibid.*, p. 92
reduced mass of relative Ga-As-motion	$M = 36.11\,\mathrm{u}$	derived from [60]
AlAs (barrier)		
gap at Γ point	$E_g^B = 3.10\,\mathrm{eV}$	Adachi [1], p. 138
(band gap is indirect: $X^c - \Gamma^v = 2.23\,\mathrm{eV}$)		
effective masses at Γ point		
electron	$m_e^B = 0.124\,m_0$	*ibid.*, p. 234
heavy hole	$m_h^B = 0.81\,m_0$	*ibid.*, p. 254

The band discontinuity in the quantum well is distributed 60-40 to conduction and valence band (cf. Adachi [1], section 8.2).

5.1.2 Structure and simulation parameters

The parameters given here apply as long as no other values are given in the plot or in the accompanying discussion.

A. Parameters modeled after Kojima experiment

These parameters are modeled after the experiments by Kojima et al. [30] on a GaAs/AlAs multiple quantum well structure. The model includes only a single well: in the experiment, the wells are almost completely uncoupled because of the strong separation by 4.5 nm thick AlAs barriers. Under the given conditions, the optical driving produces an electron population of approximately $10^{10}\,\mathrm{cm}^{-2}$.

A_s: For the calculation of absorption spectra, the probe pulse is shorter and weaker than the one used for pumping, so that its spectrum is broader and nonlinear effects are excluded.

A_r: In order to calculate the Coulomb interaction without a mean-field approximation in the Hamiltonian, the model is reduced to the most relevant subbands (e2, h1, and h2).

parameter	value		
	A	A_s	A_r
quantum well width	15.3 nm		
applied static electric field E_s	110 kV/cm		
number of subbands included (e+h)	2+3		1+2
FWHM of laser electric field τ	100 fs	40 fs	
laser central energy $\hbar\omega_0$	1.571 eV	1.550 eV	
optical driving strength $\boldsymbol{E}_0 \cdot \boldsymbol{M}_0$	0.69 meV	0.069 μeV	

B. Parameters modeled after Mizoguchi experiment

The experiment by Mizoguchi et al. [47] is similar to the Kojima experiment. The quantum well is a bit smaller and the coherent phonon oscillation is measured via its emitted terahertz radiation. The strength of optical driving again is chosen to create an electron population of $10^{10}\,\mathrm{cm}^{-2}$ under the given conditions.
B_s: Shorter and weaker pulse for calculating the absorption spectrum.

parameter	value	
	B	B_s
quantum well width	13.0 nm	
applied static electric field E_s	110 kV/cm	
number of subbands included (e+h)	1+3	
FWHM of laser electric field τ	57 fs	40 fs
laser central energy $\hbar\omega_0$	1.510 eV	1.540 eV
optical driving strength $\boldsymbol{E}_0 \cdot \boldsymbol{M}_0$	1.72 meV	0.06 μeV

C. Parameters for squeezing simulations

The quantum well width has been chosen to be small enough so that electronic states are well-separated, but not too small to inhibit charge separation, which is necessary to drive optical phonons. Charge separation is also increased by the relatively strong electric bias field.
C_s: Spectrum is calculated with a 30-fs pulse at 1.5 eV.
C_r: Model reduced to lowest electron and hole subband (e1 and h1).

parameter	value	
	C	C_r
quantum well width	11.3 nm	
applied static electric field E_s	170 kV/cm	
number of subbands included (e+h)	2+3	1+1
averaging extent in in-plane directions $\sigma_\parallel$	5 μm	
averaging extent in z-direction σ_z	20 nm	

5.1.3 Numerical parameters

parameter	value
dynamical calculations	
in-plane wave vector discretization	$\Delta k = 0.007\,\mathrm{nm}^{-1}$
... maximal value ($k \in [0, k_{\max}]$)	$k_{\max} = 0.45\,\mathrm{nm}^{-1}$
z-direction wave vector discretization	$\Delta q_z = 0.1\,\mathrm{nm}^{-1}$
... maximal value ($q_z \in [-q_{\max}, q_{\max}]$)	$q_{\max} = 1.5\,\mathrm{nm}^{-1}$
time step	$\Delta t = 2\,\mathrm{fs}$
spectra: max. time rel. to pulse peak	$t_{\max} = 1\,\mathrm{ps}$
subband structure calculation	
barrier width at each side	20 nm
real space discretization	$\Delta z = 0.018\,\mathrm{nm}$

5.2 Model Hamiltonian

non-interacting electrons, holes and phonons

$$H_0 = \sum_{i,\boldsymbol{k}} \varepsilon^{\mathrm{e}}_{i,\boldsymbol{k}} c^\dagger_{i,\boldsymbol{k}} c_{i,\boldsymbol{k}} + \sum_{j,\boldsymbol{k}} \varepsilon^{\mathrm{h}}_{j,\boldsymbol{k}} d^\dagger_{j,\boldsymbol{k}} d_{j,\boldsymbol{k}} + \sum_{\boldsymbol{q}} \hbar\omega_{\mathrm{LO}}\, b^\dagger_{\boldsymbol{q}} b_{\boldsymbol{q}}$$

Coulomb interaction

$$\begin{aligned} H_{\mathrm{Cb}} = &\frac{1}{2} \sum_{\substack{i_1 i_2 i_3 i_4 \\ \boldsymbol{k_1} \boldsymbol{k_2} \boldsymbol{k_3}}} V^{i_1 i_2 i_3 i_4}_{\boldsymbol{k_3}}\, c^\dagger_{i_1 \boldsymbol{k_1}+\boldsymbol{k_3}} c^\dagger_{i_2 \boldsymbol{k_2}-\boldsymbol{k_3}} c_{i_3 \boldsymbol{k_2}} c_{i_4 \boldsymbol{k_1}} + \frac{1}{2} \sum_{\substack{j_1 j_2 j_3 j_4 \\ \boldsymbol{k_1} \boldsymbol{k_2} \boldsymbol{k_3}}} V^{j_4 j_3 j_2 j_1}_{\boldsymbol{k_3}}\, d^\dagger_{j_1 \boldsymbol{k_1}+\boldsymbol{k_3}} d^\dagger_{j_2 \boldsymbol{k_2}-\boldsymbol{k_3}} d_{j_3 \boldsymbol{k_2}} d_{j_4 \boldsymbol{k_1}} \\ &- \sum_{\substack{i_1 i_2 j_1 j_2 \\ \boldsymbol{k_1} \boldsymbol{k_2} \boldsymbol{k_3}}} V^{i_1 j_2 j_1 i_2}_{\boldsymbol{k_3}}\, c^\dagger_{i_1 \boldsymbol{k_1}+\boldsymbol{k_3}} d^\dagger_{j_1 \boldsymbol{k_2}-\boldsymbol{k_3}} d_{j_2 \boldsymbol{k_2}} c_{i_2 \boldsymbol{k_1}} \end{aligned}$$

matrix element

$$V^{n_1 n_2 n_3 n_4}_{\boldsymbol{k}} = \frac{e^2}{2\varepsilon_0 \varepsilon_\infty A} \frac{1}{k} \iint \phi^*_{n_1}(z) \phi^*_{n_2}(z') \phi_{n_3}(z') \phi_{n_4}(z)\, \mathrm{e}^{-|z-z'|k}\, \mathrm{d}z\, \mathrm{d}z'$$

with symmetry $V^{n_1 n_2 n_3 n_4}_{\boldsymbol{k}} = V^{n_2 n_1 n_4 n_3}_{\boldsymbol{k}} = V^{*\,n_4 n_3 n_2 n_1}_{\boldsymbol{k}}$
Hamiltonian in mean-field approximation ($\mathscr{E}^{\mathrm{Ce}}$, $\mathscr{E}^{\mathrm{Ch}}$, and $\mathscr{U}^{\mathrm{C}}$ are defined in section 5.3.2)

$$\begin{aligned} H_{\mathrm{CbMF}} = &\sum_{i_1 i_2 \boldsymbol{k_1}} \mathscr{E}^{\mathrm{Ce}}_{i_1 i_2 \boldsymbol{k_1}} c^\dagger_{i_1 \boldsymbol{k_1}} c_{i_2 \boldsymbol{k_1}} + \sum_{j_1 j_2 \boldsymbol{k_1}} \mathscr{E}^{\mathrm{Ch}}_{j_1 j_2 \boldsymbol{k_1}} d^\dagger_{j_1 -\boldsymbol{k_1}} d_{j_2 -\boldsymbol{k_1}} \\ &+ \sum_{i_1 j_1 \boldsymbol{k_1}} \mathscr{U}^{\mathrm{C}}_{i_1 j_1 \boldsymbol{k_1}} c^\dagger_{i_1 \boldsymbol{k_1}} d^\dagger_{j_1 -\boldsymbol{k_1}} + \sum_{i_1 j_1 \boldsymbol{k_1}} \mathscr{U}^{\mathrm{C}*}_{i_1 j_1 \boldsymbol{k_1}} d_{j_1 -\boldsymbol{k_1}} c_{i_1 \boldsymbol{k_1}} \end{aligned}$$

coupling to laser field

$$H_{\mathrm{opt}} = \sum_{i_1 j_1 \boldsymbol{k_1}} \left[-\boldsymbol{E}\cdot\boldsymbol{M}_{i_1 j_1} c^\dagger_{i_1 \boldsymbol{k_1}} d^\dagger_{j_1 -\boldsymbol{k_1}} - \boldsymbol{E}\cdot\boldsymbol{M}^*_{i_1 j_1} d_{j_1 -\boldsymbol{k_1}} c_{i_1 \boldsymbol{k_1}} \right]$$

dipole matrix element ($\boldsymbol{E}_0 \cdot \boldsymbol{M}_0$ taken as parameter for driving strength)

$$\boldsymbol{M}_{ij} = \boldsymbol{M}_0 \int \phi_i^{\mathrm{e}*}(z)\phi_j^{\mathrm{h}}(z)\,\mathrm{d}z$$

Fröhlich interaction

$$\begin{aligned} H_{\mathrm{Fr}} = &\sum_{\substack{i_1 i_2 \\ \boldsymbol{k_1} \boldsymbol{k_2} q_{1z}}} \left[g_{\boldsymbol{q_1}}^{i_1 i_2} c_{i_1 \boldsymbol{k_2}}^\dagger c_{i_2 \boldsymbol{k_1}} b_{\boldsymbol{q_1}} + g_{\boldsymbol{q_1}}^{*\, i_1 i_2} c_{i_2 \boldsymbol{k_1}}^\dagger c_{i_1 \boldsymbol{k_2}} b_{\boldsymbol{q_1}}^\dagger \right] \\ &- \sum_{\substack{j_1 j_2 \\ \boldsymbol{k_1} \boldsymbol{k_2} q_{1z}}} \left[g_{\boldsymbol{q_1}}^{j_2 j_1} d_{j_1 \boldsymbol{k_2}}^\dagger d_{j_2 \boldsymbol{k_1}} b_{\boldsymbol{q_1}} + g_{\boldsymbol{q_1}}^{*\, j_2 j_1} d_{j_2 \boldsymbol{k_1}}^\dagger d_{j_1 \boldsymbol{k_2}} b_{\boldsymbol{q_1}}^\dagger \right] \end{aligned}$$

with $\boldsymbol{q_1} = \boldsymbol{k_2} - \boldsymbol{k_1} + q_{1z}\boldsymbol{e}_z$; coupling matrix element

$$g_{\boldsymbol{q}}^{n_1 n_2} = -\mathrm{i}\sqrt{\frac{e^2 \hbar \omega_{\mathrm{LO}}}{2\varepsilon_0 V}\left(\frac{1}{\varepsilon_\infty} - \frac{1}{\varepsilon_{\mathrm{s}}}\right)} \cdot \mathscr{F}_{q_z}^{n_1 n_2} \frac{1}{q}$$

form factor

$$\mathscr{F}_{q_z}^{n_1 n_2} = \int \phi_{n_1}^*(z)\phi_{n_2}(z)\mathrm{e}^{\mathrm{i}q_z z}\,\mathrm{d}z$$

with symmetry $\mathscr{F}_{q_z}^{n_1 n_2} = \mathscr{F}_{-q_z}^{*\, n_2 n_1}$

5.3 Correlation expansion

This is the system of equations for second-order calculations. First order is not given explicitly, but it can easily be derived from second order by setting all phonon-assisted correlations and all two-phonon correlations to zero. Factors of two that result from the implicit spin sums are denoted 2*. In these equations, the phonon wave vector $\boldsymbol{q}$ is defined as $\boldsymbol{q} = \boldsymbol{k'} - \boldsymbol{k} + q_z \boldsymbol{e}_z$.

5.3.1 Dynamical variables

electron populations and coherences; coherent phonon amplitude

$$f_{ii'\boldsymbol{k}}^{\mathrm{e}} = \langle c_{i\boldsymbol{k}}^\dagger c_{i'\boldsymbol{k}} \rangle \qquad f_{jj'\boldsymbol{k}}^{\mathrm{h}} = \langle d_{j-\boldsymbol{k}}^\dagger d_{j'-\boldsymbol{k}} \rangle \qquad p_{ji\boldsymbol{k}} = \langle d_{j-\boldsymbol{k}} c_{i\boldsymbol{k}} \rangle \qquad B_{q_z} = \langle b_{q_z \boldsymbol{e}_z} \rangle$$

phonon-assisted correlations

$$\begin{aligned} \delta s_{\boldsymbol{k}\boldsymbol{k'} q_z}^{\mathrm{e}\, ii'} &= \langle c_{i\boldsymbol{k'}}^\dagger c_{i'\boldsymbol{k}} b_{\boldsymbol{q}} \rangle - \delta_{\boldsymbol{k}\boldsymbol{k'}} f_{ii'\boldsymbol{k}}^{\mathrm{e}} B_{q_z} & \delta s_{\boldsymbol{k}\boldsymbol{k'} q_z}^{\mathrm{h}\, jj'} &= \langle d_{j-\boldsymbol{k}}^\dagger d_{j'-\boldsymbol{k'}} b_{\boldsymbol{q}} \rangle - \delta_{\boldsymbol{k}\boldsymbol{k'}} f_{jj'\boldsymbol{k}}^{\mathrm{h}} B_{q_z} \\ \delta s_{\boldsymbol{k}\boldsymbol{k'} q_z}^{\mathrm{he}\, ji} &= \langle d_{j-\boldsymbol{k'}} c_{i\boldsymbol{k}} b_{\boldsymbol{q}} \rangle - \delta_{\boldsymbol{k}\boldsymbol{k'}} p_{ji\boldsymbol{k}} B_{q_z} & \delta s_{\boldsymbol{k}\boldsymbol{k'} q_z}^{\mathrm{hek}\, ji} &= \langle d_{j-\boldsymbol{k}} c_{i\boldsymbol{k'}} b_{\boldsymbol{q}}^\dagger \rangle - \delta_{\boldsymbol{k}\boldsymbol{k'}} p_{ji\boldsymbol{k}} B_{q_z}^* \end{aligned}$$

two-phonon correlations

$$\begin{aligned} \delta n_{\boldsymbol{k} q_z q_z'} &= \langle b_{\boldsymbol{k}+q_z\boldsymbol{e}_z}^\dagger b_{\boldsymbol{k}+q_z'\boldsymbol{e}_z} \rangle - \delta_{\boldsymbol{k},0} B_{q_z}^* B_{q_z'} \\ \delta b_{\boldsymbol{k} q_z q_z'} &= \langle b_{\boldsymbol{k}+q_z\boldsymbol{e}_z} b_{-\boldsymbol{k}+q_z'\boldsymbol{e}_z} \rangle - \delta_{\boldsymbol{k},0} B_{q_z} B_{q_z'} \end{aligned}$$

5.3.2 Abbreviations for interaction terms

general

$$\delta S^{\mathrm{e}\,ii'}_{\boldsymbol{k}q_\mathrm{z}} = \sum_{\boldsymbol{k}_1} \delta s^{\mathrm{e}\,ii'}_{\boldsymbol{k}_1,\boldsymbol{k}_1+\boldsymbol{k},q_\mathrm{z}} \qquad \delta S^{\mathrm{h}\,jj'}_{\boldsymbol{k}q_\mathrm{z}} = \sum_{\boldsymbol{k}_1} \delta s^{\mathrm{h}\,jj'}_{\boldsymbol{k}_1,\boldsymbol{k}_1+\boldsymbol{k},q_\mathrm{z}}$$

Fröhlich interaction

$$\mathscr{E}^{\mathrm{Pe}}_{ii'} = \sum_{q_{1\mathrm{z}}} \left(g^{ii'}_{q_{1\mathrm{z}}} B_{q_{1\mathrm{z}}} + g^{*i'i}_{q_{1\mathrm{z}}} B^*_{q_{1\mathrm{z}}} \right)$$

$$\mathscr{E}^{\mathrm{Ph}}_{jj'} = -\sum_{q_{1\mathrm{z}}} \left(g^{j'j}_{q_{1\mathrm{z}}} B_{q_{1\mathrm{z}}} + g^{*jj'}_{q_{1\mathrm{z}}} B^*_{q_{1\mathrm{z}}} \right)$$

$$B^{\mathrm{P2e}\,ii'}_{\boldsymbol{k}q_\mathrm{z}} = \sum_{q_{1\mathrm{z}}} g^{*ii'}_{\boldsymbol{k}+q_{1\mathrm{z}}\boldsymbol{e}_\mathrm{z}} \left(\delta n_{\boldsymbol{k},q_{1\mathrm{z}},q_\mathrm{z}} - \delta b_{\boldsymbol{k},q_\mathrm{z},-q_{1\mathrm{z}}} \right)$$

$$B^{\mathrm{P2h}\,jj'}_{\boldsymbol{k}q_\mathrm{z}} = -\sum_{q_{1\mathrm{z}}} g^{*j'j}_{\boldsymbol{k}+q_{1\mathrm{z}}\boldsymbol{e}_\mathrm{z}} \left(\delta n_{\boldsymbol{k},q_{1\mathrm{z}},q_\mathrm{z}} - \delta b_{\boldsymbol{k},q_\mathrm{z},-q_{1\mathrm{z}}} \right)$$

Coulomb interaction (mean-field Hamiltonian)

$$\mathscr{E}^{\mathrm{Ce}}_{ii'\boldsymbol{k}} = 2^* \sum_{i_1 i_2} V_0^{ii_1 i_2 i'} \sum_{\boldsymbol{k}_1} f^{\mathrm{e}}_{i_1 i_2 \boldsymbol{k}_1} - 2^* \sum_{j_1 j_2} V_0^{ij_2 j_1 i'} \sum_{\boldsymbol{k}_1} f^{\mathrm{h}}_{j_1 j_2 \boldsymbol{k}_1} - \sum_{i_1 i_2 \boldsymbol{k}_1} V^{ii_1 i'i_2}_{\boldsymbol{k}_1} f^{\mathrm{e}}_{i_1 i_2 \boldsymbol{k}+\boldsymbol{k}_1}$$

$$\mathscr{E}^{\mathrm{Ch}}_{jj'\boldsymbol{k}} = 2^* \sum_{j_1 j_2} V_0^{j'j_2 j_1 j} \sum_{\boldsymbol{k}_1} f^{\mathrm{h}}_{j_1 j_2 \boldsymbol{k}_1} - 2^* \sum_{i_1 i_2} V_0^{i_1 j' j i_2} \sum_{\boldsymbol{k}_1} f^{\mathrm{e}}_{i_1 i_2 \boldsymbol{k}_1} - \sum_{j_1 j_2 \boldsymbol{k}_1} V^{j'j_2 j j_1}_{\boldsymbol{k}_1} f^{\mathrm{h}}_{j_1 j_2 \boldsymbol{k}+\boldsymbol{k}_1}$$

$$\mathscr{U}^{\mathrm{C}}_{ij\boldsymbol{k}} = -\sum_{i_1 j_1 \boldsymbol{k}_1} V^{ij_1 j i_1}_{\boldsymbol{k}_1} p_{j_1 i_1 \boldsymbol{k}+\boldsymbol{k}_1}$$

Coulomb interaction (additional terms beyond mean-field Hamiltonian)

$$\mathscr{E}^{\mathrm{Cse}}_{ii'\boldsymbol{k}\boldsymbol{k}'q_\mathrm{z}} = 2^* \sum_{i_1 i_2} V^{ii_1 i_2 i'}_{\boldsymbol{k}'-\boldsymbol{k}} \delta S^{\mathrm{e}\,i_1 i_2}_{\boldsymbol{k}'-\boldsymbol{k},q_\mathrm{z}} - 2^* \sum_{j_1 j_2} V^{ij_2 j_1 i'}_{\boldsymbol{k}'-\boldsymbol{k}} \delta S^{\mathrm{h}\,j_1 j_2}_{\boldsymbol{k}'-\boldsymbol{k},q_\mathrm{z}} - \sum_{i_1 i_2 \boldsymbol{k}_1} V^{ii_1 i'i_2}_{\boldsymbol{k}_1} \delta s^{\mathrm{e}\,i_1 i_2}_{\boldsymbol{k}+\boldsymbol{k}_1,\boldsymbol{k}'+\boldsymbol{k}_1,q_\mathrm{z}}$$

$$\mathscr{E}^{\mathrm{Csh}}_{jj'\boldsymbol{k}\boldsymbol{k}'q_\mathrm{z}} = 2^* \sum_{j_1 j_2} V^{j'j_2 j_1 j}_{\boldsymbol{k}'-\boldsymbol{k}} \delta S^{\mathrm{h}\,j_1 j_2}_{\boldsymbol{k}'-\boldsymbol{k},q_\mathrm{z}} - 2^* \sum_{i_1 i_2} V^{i_1 j' j i_2}_{\boldsymbol{k}'-\boldsymbol{k}} \delta S^{\mathrm{e}\,i_1 i_2}_{\boldsymbol{k}'-\boldsymbol{k},q_\mathrm{z}} - \sum_{j_1 j_2 \boldsymbol{k}_1} V^{j'j_2 j j_1}_{\boldsymbol{k}_1} \delta s^{\mathrm{h}\,j_1 j_2}_{\boldsymbol{k}+\boldsymbol{k}_1,\boldsymbol{k}'+\boldsymbol{k}_1,q_\mathrm{z}}$$

$$\mathscr{U}^{\mathrm{Cshe}}_{ij\boldsymbol{k}\boldsymbol{k}'q_\mathrm{z}} = -\sum_{i_1 j_1 \boldsymbol{k}_1} V^{ij_1 j i_1}_{\boldsymbol{k}_1} \delta s^{\mathrm{he}\,j_1 i_1}_{\boldsymbol{k}+\boldsymbol{k}_1,\boldsymbol{k}'+\boldsymbol{k}_1,q_\mathrm{z}}$$

$$\mathscr{U}^{\mathrm{Cshek}}_{ij\boldsymbol{k}\boldsymbol{k}'q_\mathrm{z}} = -\sum_{i_1 j_1 \boldsymbol{k}_1} V^{ij_1 j i_1}_{\boldsymbol{k}_1} \delta s^{\mathrm{hek}\,j_1 i_1}_{\boldsymbol{k}+\boldsymbol{k}_1,\boldsymbol{k}'+\boldsymbol{k}_1,q_\mathrm{z}}$$

5.3.3 Equations of motion

The text to the right indicates which part of the Hamiltonian is responsible.

$$
\begin{aligned}
\mathrm{i}\hbar\frac{\mathrm{d}}{\mathrm{d}t}f^{\mathrm{e}}_{ii'\boldsymbol{k}} = \quad & \left(\varepsilon^{\mathrm{e}}_{i'\boldsymbol{k}} - \varepsilon^{\mathrm{e}}_{i\boldsymbol{k}}\right) f^{\mathrm{e}}_{ii'\boldsymbol{k}} && \Big\rceil\ H_0 \\
& + \sum_{j_1}\left(- \boldsymbol{E}\cdot\boldsymbol{M}_{i'j_1} p^{*}_{j_1 i\boldsymbol{k}} + \boldsymbol{E}\cdot\boldsymbol{M}^{*}_{ij_1} p_{j_1 i'\boldsymbol{k}}\right) && \Big\rceil\ H_{\mathrm{opt}} \\
& + \sum_{i_1}\left(\mathscr{E}^{\mathrm{Pe}}_{i'i_1} f^{\mathrm{e}}_{ii_1\boldsymbol{k}} - \mathscr{E}^{\mathrm{Pe}}_{i_1 i} f^{\mathrm{e}}_{i_1 i'\boldsymbol{k}}\right) && \Big\rceil\ H_{\mathrm{Fr}}\ \text{(1st order)} \\
& + \sum_{i_1 \boldsymbol{k}_1 q_{1z}} \Big[\; g^{i'i_1}_{\boldsymbol{k}-\boldsymbol{k}_1+q_{1z}\boldsymbol{e}_z} \delta s^{\mathrm{e}\, i i_1}_{\boldsymbol{k}_1 \boldsymbol{k} q_{1z}} - g^{i_1 i}_{\boldsymbol{k}_1-\boldsymbol{k}+q_{1z}\boldsymbol{e}_z} \delta s^{\mathrm{e}\, i_1 i'}_{\boldsymbol{k}\boldsymbol{k}_1 q_{1z}} \\
& \qquad + g^{*i_1 i'}_{\boldsymbol{k}_1-\boldsymbol{k}+q_{1z}\boldsymbol{e}_z} \delta s^{\mathrm{e}*\, i_1 i}_{\boldsymbol{k}\boldsymbol{k}_1 q_{1z}} - g^{*ii_1}_{\boldsymbol{k}-\boldsymbol{k}_1+q_{1z}\boldsymbol{e}_z} \delta s^{\mathrm{e}*\, i' i_1}_{\boldsymbol{k}_1 \boldsymbol{k} q_{1z}} \Big] && \Big\rceil\ H_{\mathrm{Fr}}\ \text{(2nd order)} \\
& + \sum_{i_1}\left(\mathscr{E}^{\mathrm{Ce}}_{i'i_1\boldsymbol{k}} f^{\mathrm{e}}_{ii_1\boldsymbol{k}} - \mathscr{E}^{\mathrm{Ce}}_{i_1 i\boldsymbol{k}} f^{\mathrm{e}}_{i_1 i'\boldsymbol{k}}\right) \\
& + \sum_{j_1}\left(\mathscr{U}^{\mathrm{C}}_{i'j_1\boldsymbol{k}} p^{*}_{j_1 i\boldsymbol{k}} - \mathscr{U}^{\mathrm{C}*}_{ij_1\boldsymbol{k}} p_{j_1 i'\boldsymbol{k}}\right) && \Big\rceil\ H_{\mathrm{Cb}}\ \text{(MF)} \\
\mathrm{i}\hbar\frac{\mathrm{d}}{\mathrm{d}t}f^{\mathrm{h}}_{jj'\boldsymbol{k}} = \quad & \left(\varepsilon^{\mathrm{h}}_{j'\boldsymbol{k}} - \varepsilon^{\mathrm{h}}_{j\boldsymbol{k}}\right) f^{\mathrm{h}}_{jj'\boldsymbol{k}} && \Big\rceil\ H_0 \\
& + \sum_{i_1}\left(- \boldsymbol{E}\cdot\boldsymbol{M}_{i_1 j'} p^{*}_{ji_1\boldsymbol{k}} + \boldsymbol{E}\cdot\boldsymbol{M}^{*}_{i_1 j} p_{j'i_1\boldsymbol{k}}\right) && \Big\rceil\ H_{\mathrm{opt}} \\
& + \sum_{j_1}\left(\mathscr{E}^{\mathrm{Ph}}_{j'j_1} f^{\mathrm{h}}_{jj_1\boldsymbol{k}} - \mathscr{E}^{\mathrm{Ph}}_{j_1 j} f^{\mathrm{h}}_{j_1 j'\boldsymbol{k}}\right) && \Big\rceil\ H_{\mathrm{Fr}}\ \text{(1st order)} \\
& + \sum_{j_1 \boldsymbol{k}_1 q_{1z}} \Big[- g^{j_1 j'}_{\boldsymbol{k}-\boldsymbol{k}_1+q_{1z}\boldsymbol{e}_z} \delta s^{\mathrm{h}\, j j_1}_{\boldsymbol{k}\boldsymbol{k}_1 q_{1z}} + g^{j j_1}_{\boldsymbol{k}_1-\boldsymbol{k}+q_{1z}\boldsymbol{e}_z} \delta s^{\mathrm{h}\, j_1 j'}_{\boldsymbol{k}_1 \boldsymbol{k} q_{1z}} \\
& \qquad - g^{*j' j_1}_{\boldsymbol{k}_1-\boldsymbol{k}+q_{1z}\boldsymbol{e}_z} \delta s^{\mathrm{h}*\, j_1 j}_{\boldsymbol{k}_1 \boldsymbol{k} q_{1z}} + g^{*j_1 j}_{\boldsymbol{k}-\boldsymbol{k}_1+q_{1z}\boldsymbol{e}_z} \delta s^{\mathrm{h}*\, j' j_1}_{\boldsymbol{k}\boldsymbol{k}_1 q_{1z}} \Big] && \Big\rceil\ H_{\mathrm{Fr}}\ \text{(2nd order)} \\
& + \sum_{j_1}\left(\mathscr{E}^{\mathrm{Ch}}_{j'j_1\boldsymbol{k}} f^{\mathrm{h}}_{jj_1\boldsymbol{k}} - \mathscr{E}^{\mathrm{Ch}}_{j_1 j\boldsymbol{k}} f^{\mathrm{h}}_{j_1 j'\boldsymbol{k}}\right) \\
& + \sum_{i_1}\left(\mathscr{U}^{\mathrm{C}}_{i_1 j'\boldsymbol{k}} p^{*}_{ji_1\boldsymbol{k}} - \mathscr{U}^{\mathrm{C}*}_{i_1 j\boldsymbol{k}} p_{j'i_1\boldsymbol{k}}\right) && \Big\rceil\ H_{\mathrm{Cb}}\ \text{(MF)} \\
\mathrm{i}\hbar\frac{\mathrm{d}}{\mathrm{d}t}p_{ji\boldsymbol{k}} = \quad & \left(\varepsilon^{\mathrm{e}}_{i\boldsymbol{k}} + \varepsilon^{\mathrm{h}}_{j\boldsymbol{k}}\right) p_{ji\boldsymbol{k}} && \Big\rceil\ H_0 \\
& + \sum_{i_1} \boldsymbol{E}\cdot\boldsymbol{M}_{i_1 j} f^{\mathrm{e}}_{i_1 i\boldsymbol{k}} + \sum_{j_1} \boldsymbol{E}\cdot\boldsymbol{M}_{ij_1} f^{\mathrm{h}}_{j_1 j\boldsymbol{k}} - \boldsymbol{E}\cdot\boldsymbol{M}_{ij} && \Big\rceil\ H_{\mathrm{opt}} \\
& + \sum_{i_1} \mathscr{E}^{\mathrm{Pe}}_{ii_1} p_{ji_1\boldsymbol{k}} + \sum_{j_1} \mathscr{E}^{\mathrm{Ph}}_{jj_1} p_{j_1 i\boldsymbol{k}} && \Big\rceil\ H_{\mathrm{Fr}}\ \text{(1st order)} \\
& + \sum_{i_1 \boldsymbol{k}_1 q_{1z}} \left[g^{i i_1}_{\boldsymbol{k}-\boldsymbol{k}_1+q_{1z}\boldsymbol{e}_z} \delta s^{\mathrm{he}\, j i_1}_{\boldsymbol{k}_1 \boldsymbol{k} q_{1z}} + g^{*i_1 i}_{\boldsymbol{k}_1-\boldsymbol{k}+q_{1z}\boldsymbol{e}_z} \delta s^{\mathrm{hek}\, j i_1}_{\boldsymbol{k}\boldsymbol{k}_1 q_{1z}} \right] \\
& - \sum_{j_1 \boldsymbol{k}_1 q_{1z}} \left[g^{j_1 j}_{\boldsymbol{k}_1-\boldsymbol{k}+q_{1z}\boldsymbol{e}_z} \delta s^{\mathrm{he}\, j_1 i}_{\boldsymbol{k}\boldsymbol{k}_1 q_{1z}} + g^{*j j_1}_{\boldsymbol{k}-\boldsymbol{k}_1+q_{1z}\boldsymbol{e}_z} \delta s^{\mathrm{hek}\, j_1 i}_{\boldsymbol{k}_1 \boldsymbol{k} q_{1z}} \right] && \Big\rceil\ H_{\mathrm{Fr}}\ \text{(2nd order)} \\
& + \sum_{i_1}\left(\mathscr{E}^{\mathrm{Ce}}_{ii_1\boldsymbol{k}} p_{ji_1\boldsymbol{k}} - \mathscr{U}^{\mathrm{C}}_{i_1 j\boldsymbol{k}} f^{\mathrm{e}}_{i_1 i\boldsymbol{k}}\right) \\
& + \sum_{j_1}\left(\mathscr{E}^{\mathrm{Ch}}_{jj_1\boldsymbol{k}} p_{j_1 i\boldsymbol{k}} - \mathscr{U}^{\mathrm{C}}_{ij_1\boldsymbol{k}} f^{\mathrm{h}}_{j_1 j\boldsymbol{k}}\right) + \mathscr{U}^{\mathrm{C}}_{ij\boldsymbol{k}} && \Big\rceil\ H_{\mathrm{Cb}}\ \text{(MF)}
\end{aligned}
$$

$$
\begin{aligned}
\mathrm{i}\hbar\frac{\mathrm{d}}{\mathrm{d}t}B_{q_z} = {} & \hbar\omega_{\mathrm{LO}}B_{q_z} && \Big] H_0\\
& + 2^*\sum_{i_1 i_2 \boldsymbol{k_1}} g^{*\,i_1 i_2}_{q_z} f^{\mathrm{e}}_{i_2 i_1 \boldsymbol{k_1}} - 2^*\sum_{j_1 j_2 \boldsymbol{k_1}} g^{*\,j_2 j_1}_{q_z} f^{\mathrm{h}}_{j_2 j_1 \boldsymbol{k_1}} && \Big] H_{\mathrm{Fr}}\ (1\text{st order})
\end{aligned}
$$

$$
\begin{aligned}
\mathrm{i}\hbar\frac{\mathrm{d}}{\mathrm{d}t}\delta s^{\mathrm{e}\,i i'}_{\boldsymbol{k}\boldsymbol{k}' q_z} = {} & \left(\varepsilon^{\mathrm{e}}_{i'\boldsymbol{k}} - \varepsilon^{\mathrm{e}}_{i\boldsymbol{k}'} + \hbar\omega_{\mathrm{LO}}\right)\delta s^{\mathrm{e}\,i i'}_{\boldsymbol{k}\boldsymbol{k}' q_z} && \Big] H_0\\
& - \sum_{j_1} \boldsymbol{E}\cdot\boldsymbol{M}_{i' j_1}\delta s^{\mathrm{hek}*\,j_1 i}_{\boldsymbol{k}\boldsymbol{k}' q_z} + \sum_{j_1} \boldsymbol{E}\cdot\boldsymbol{M}^*_{i j_1}\delta s^{\mathrm{he}\,j_1 i'}_{\boldsymbol{k}\boldsymbol{k}' q_z} && \Big] H_{\mathrm{opt}}\\
& + \sum_{i_1}\left(\mathscr{E}^{\mathrm{Pe}}_{i' i_1}\delta s^{\mathrm{e}\,i i_1}_{\boldsymbol{k}\boldsymbol{k}' q_z} - \mathscr{E}^{\mathrm{Pe}}_{i_1 i}\delta s^{\mathrm{e}\,i_1 i'}_{\boldsymbol{k}\boldsymbol{k}' q_z}\right) + \sum_{i_1}\left(B^{\mathrm{P2e}\,i_1 i'}_{\boldsymbol{k}'-\boldsymbol{k}, q_z} f^{\mathrm{e}}_{i i_1 \boldsymbol{k}'} - B^{\mathrm{P2e}\,i i_1}_{\boldsymbol{k}'-\boldsymbol{k}, q_z} f^{\mathrm{e}}_{i_1 i' \boldsymbol{k}}\right) && \Big]\\
& + \sum_{i_1 i_2} f^{\mathrm{e}}_{i i_1 \boldsymbol{k}'} g^{*\,i_1 i_2}_{\boldsymbol{q}}(\delta_{i_2 i'} - f^{\mathrm{e}}_{i_2 i' \boldsymbol{k}}) - \sum_{j_1 j_2} g^{*\,j_2 j_1}_{\boldsymbol{q}} p^*_{j_2 i \boldsymbol{k}'} p_{j_1 i' \boldsymbol{k}} && \Big] H_{\mathrm{Fr}}\ (2\text{nd})\\
& + \sum_{i_1}\left(\mathscr{E}^{\mathrm{Ce}}_{i' i_1 \boldsymbol{k}}\delta s^{\mathrm{e}\,i i_1}_{\boldsymbol{k}\boldsymbol{k}' q_z} - \mathscr{E}^{\mathrm{Ce}}_{i_1 i \boldsymbol{k}'}\delta s^{\mathrm{e}\,i_1 i'}_{\boldsymbol{k}\boldsymbol{k}' q_z}\right) && \Big]\\
& + \sum_{j_1}\left(\mathscr{U}^{\mathrm{C}}_{i' j_1 \boldsymbol{k}}\delta s^{\mathrm{hek}*\,j_1 i}_{\boldsymbol{k}\boldsymbol{k}' q_z} - \mathscr{U}^{\mathrm{C}*}_{i j_1 \boldsymbol{k}'}\delta s^{\mathrm{he}\,j_1 i'}_{\boldsymbol{k}\boldsymbol{k}' q_z}\right) && \Big] H_{\mathrm{Cb}}\ (\mathrm{MF})\\
& + \sum_{i_1}\left(\mathscr{E}^{\mathrm{Cse}}_{i' i_1 \boldsymbol{k}\boldsymbol{k}' q_z} f^{\mathrm{e}}_{i i_1 \boldsymbol{k}'} - \mathscr{E}^{\mathrm{Cse}}_{i_1 i \boldsymbol{k}\boldsymbol{k}' q_z} f^{\mathrm{e}}_{i_1 i' \boldsymbol{k}}\right) && \Big]\\
& + \sum_{j_1}\left(\mathscr{U}^{\mathrm{Cshe}}_{i' j_1 \boldsymbol{k}\boldsymbol{k}' q_z} p^*_{j_1 i \boldsymbol{k}'} - \mathscr{U}^{\mathrm{Cshek}*}_{i j_1 \boldsymbol{k}\boldsymbol{k}' q_z} p_{j_1 i' \boldsymbol{k}}\right) && \Big] H_{\mathrm{Cb}}\ (>\mathrm{MF})
\end{aligned}
$$

$$
\begin{aligned}
\mathrm{i}\hbar\frac{\mathrm{d}}{\mathrm{d}t}\delta s^{\mathrm{h}\,j j'}_{\boldsymbol{k}\boldsymbol{k}' q_z} = {} & \left(\varepsilon^{\mathrm{h}}_{j'\boldsymbol{k}'} - \varepsilon^{\mathrm{h}}_{j\boldsymbol{k}} + \hbar\omega_{\mathrm{LO}}\right)\delta s^{\mathrm{h}\,j j'}_{\boldsymbol{k}\boldsymbol{k}' q_z} && \Big] H_0\\
& - \sum_{i_1} \boldsymbol{E}\cdot\boldsymbol{M}_{i_1 j'}\delta s^{\mathrm{hek}*\,j i_1}_{\boldsymbol{k}\boldsymbol{k}' q_z} + \sum_{i_1} \boldsymbol{E}\cdot\boldsymbol{M}^*_{i_1 j}\delta s^{\mathrm{he}\,j' i_1}_{\boldsymbol{k}\boldsymbol{k}' q_z} && \Big] H_{\mathrm{opt}}\\
& + \sum_{j_1}\left(\mathscr{E}^{\mathrm{Ph}}_{j' j_1}\delta s^{\mathrm{h}\,j j_1}_{\boldsymbol{k}\boldsymbol{k}' q_z} - \mathscr{E}^{\mathrm{Ph}}_{j_1 j}\delta s^{\mathrm{h}\,j_1 j'}_{\boldsymbol{k}\boldsymbol{k}' q_z}\right) + \sum_{j_1}\left(B^{\mathrm{P2h}\,j_1 j'}_{\boldsymbol{k}'-\boldsymbol{k}, q_z} f^{\mathrm{h}}_{j j_1 \boldsymbol{k}} - B^{\mathrm{P2h}\,j j_1}_{\boldsymbol{k}'-\boldsymbol{k}, q_z} f^{\mathrm{h}}_{j_1 j' \boldsymbol{k}'}\right) && \Big]\\
& - \sum_{j_1 j_2} f^{\mathrm{h}}_{j j_1 \boldsymbol{k}} g^{*\,j_2 j_1}_{\boldsymbol{q}}(\delta_{j_2 j'} - f^{\mathrm{h}}_{j_2 j' \boldsymbol{k}'}) + \sum_{i_1 i_2} g^{*\,i_1 i_2}_{\boldsymbol{q}} p_{j' i_1 \boldsymbol{k}'} p^*_{j i_2 \boldsymbol{k}} && \Big] H_{\mathrm{Fr}}\ (2\text{nd})\\
& + \sum_{j_1}\left(\mathscr{E}^{\mathrm{Ch}}_{j' j_1 \boldsymbol{k}'}\delta s^{\mathrm{h}\,j j_1}_{\boldsymbol{k}\boldsymbol{k}' q_z} - \mathscr{E}^{\mathrm{Ch}}_{j_1 j \boldsymbol{k}}\delta s^{\mathrm{h}\,j_1 j'}_{\boldsymbol{k}\boldsymbol{k}' q_z}\right) && \Big]\\
& + \sum_{i_1}\left(\mathscr{U}^{\mathrm{C}}_{i_1 j' \boldsymbol{k}'}\delta s^{\mathrm{hek}*\,j i_1}_{\boldsymbol{k}\boldsymbol{k}' q_z} - \mathscr{U}^{\mathrm{C}*}_{i_1 j \boldsymbol{k}}\delta s^{\mathrm{he}\,j' i_1}_{\boldsymbol{k}\boldsymbol{k}' q_z}\right) && \Big] H_{\mathrm{Cb}}\ (\mathrm{MF})\\
& + \sum_{j_1}\left(\mathscr{E}^{\mathrm{Csh}}_{j' j_1 \boldsymbol{k}\boldsymbol{k}' q_z} f^{\mathrm{h}}_{j j_1 \boldsymbol{k}} - \mathscr{E}^{\mathrm{Csh}}_{j_1 j \boldsymbol{k}\boldsymbol{k}' q_z} f^{\mathrm{h}}_{j_1 j' \boldsymbol{k}'}\right) && \Big]\\
& + \sum_{i_1}\left(\mathscr{U}^{\mathrm{Cshe}}_{i_1 j' \boldsymbol{k}\boldsymbol{k}' q_z} p^*_{j i_1 \boldsymbol{k}} - \mathscr{U}^{\mathrm{Cshek}*}_{i_1 j \boldsymbol{k}\boldsymbol{k}' q_z} p_{j' i_1 \boldsymbol{k}'}\right) && \Big] H_{\mathrm{Cb}}\ (>\mathrm{MF})
\end{aligned}
$$

$$
\begin{aligned}
\mathrm{i}\hbar\frac{\mathrm{d}}{\mathrm{d}t}\delta s^{\mathrm{he}\,ji}_{\boldsymbol{k}\boldsymbol{k}'q_z} &= \left(\varepsilon^{\mathrm{e}}_{i\boldsymbol{k}}+\varepsilon^{\mathrm{h}}_{j\boldsymbol{k}'}+\hbar\omega_{\mathrm{LO}}\right)\delta s^{\mathrm{he}\,ji}_{\boldsymbol{k}\boldsymbol{k}'q_z} && \Big]\ H_0\\
&+\sum_{j_1}\boldsymbol{E}\cdot\boldsymbol{M}_{ij_1}\delta s^{\mathrm{h}\,j_1j}_{\boldsymbol{k}\boldsymbol{k}'q_z}+\sum_{i_1}\boldsymbol{E}\cdot\boldsymbol{M}_{i_1j}\delta s^{\mathrm{e}\,i_1i}_{\boldsymbol{k}\boldsymbol{k}'q_z} && \Big]\ H_{\mathrm{opt}}\\
&+\sum_{i_1}\mathscr{E}^{\mathrm{Pe}}_{ii_1}\delta s^{\mathrm{he}\,ji_1}_{\boldsymbol{k}\boldsymbol{k}'q_z}+\sum_{j_1}\mathscr{E}^{\mathrm{Ph}}_{jj_1}\delta s^{\mathrm{he}\,j_1i}_{\boldsymbol{k}\boldsymbol{k}'q_z}+\sum_{i_1}B^{\mathrm{P2e}\,i_1i}_{\boldsymbol{k}'-\boldsymbol{k},q_z}p_{ji_1\boldsymbol{k}'}+\sum_{j_1}B^{\mathrm{P2h}\,j_1j}_{\boldsymbol{k}'-\boldsymbol{k},q_z}p_{j_1i\boldsymbol{k}} && \Big]\ H_{\mathrm{Fr}}\ (2\mathrm{nd})\\
&+\sum_{i_1i_2}p_{ji_1\boldsymbol{k}'}g^{*i_1i_2}_{\boldsymbol{q}}(\delta_{i_2i}-f^{\mathrm{e}}_{i_2i\boldsymbol{k}})-\sum_{j_1j_2}p_{j_1i\boldsymbol{k}}g^{*j_2j_1}_{\boldsymbol{q}}(\delta_{j_2j}-f^{\mathrm{h}}_{j_2j\boldsymbol{k}'}) && \Big]\\
&+\sum_{i_1}\left(\mathscr{E}^{\mathrm{Ce}}_{ii_1\boldsymbol{k}}\delta s^{\mathrm{he}\,ji_1}_{\boldsymbol{k}\boldsymbol{k}'q_z}-\mathscr{U}^{\mathrm{C}}_{i_1j\boldsymbol{k}'}\delta s^{\mathrm{e}\,i_1i}_{\boldsymbol{k}\boldsymbol{k}'q_z}\right) && \Big]\\
&+\sum_{j_1}\left(\mathscr{E}^{\mathrm{Ch}}_{jj_1\boldsymbol{k}'}\delta s^{\mathrm{he}\,j_1i}_{\boldsymbol{k}\boldsymbol{k}'q_z}-\mathscr{U}^{\mathrm{C}}_{ij_1\boldsymbol{k}}\delta s^{\mathrm{h}\,j_1j}_{\boldsymbol{k}\boldsymbol{k}'q_z}\right) && \Big]\ H_{\mathrm{Cb}}\ (\mathrm{MF})\\
&+\sum_{i_1}\left(\mathscr{E}^{\mathrm{Cse}}_{ii_1\boldsymbol{k}\boldsymbol{k}'q_z}p_{ji_1\boldsymbol{k}'}-\mathscr{U}^{\mathrm{Cshe}}_{i_1j\boldsymbol{k}\boldsymbol{k}'q_z}f^{\mathrm{e}}_{i_1i\boldsymbol{k}}\right) && \Big]\\
&+\sum_{j_1}\left(\mathscr{E}^{\mathrm{Csh}}_{jj_1\boldsymbol{k}\boldsymbol{k}'q_z}p_{j_1i\boldsymbol{k}}-\mathscr{U}^{\mathrm{Cshe}}_{ij_1\boldsymbol{k}\boldsymbol{k}'q_z}f^{\mathrm{h}}_{j_1j\boldsymbol{k}'}\right)+\mathscr{U}^{\mathrm{Cshe}}_{ij\boldsymbol{k}\boldsymbol{k}'q_z} && \Big]\ H_{\mathrm{Cb}}\ (>\mathrm{MF})
\end{aligned}
$$

$$
\begin{aligned}
\mathrm{i}\hbar\frac{\mathrm{d}}{\mathrm{d}t}\delta s^{\mathrm{hek}\,ji}_{\boldsymbol{k}\boldsymbol{k}'q_z} &= \left(\varepsilon^{\mathrm{e}}_{i\boldsymbol{k}'}+\varepsilon^{\mathrm{h}}_{j\boldsymbol{k}}-\hbar\omega_{\mathrm{LO}}\right)\delta s^{\mathrm{hek}\,ji}_{\boldsymbol{k}\boldsymbol{k}'q_z} && \Big]\ H_0\\
&+\sum_{j_1}\boldsymbol{E}\cdot\boldsymbol{M}_{ij_1}\delta s^{\mathrm{h}*\,jj_1}_{\boldsymbol{k}\boldsymbol{k}'q_z}+\sum_{i_1}\boldsymbol{E}\cdot\boldsymbol{M}_{i_1j}\delta s^{\mathrm{e}*\,ii_1}_{\boldsymbol{k}\boldsymbol{k}'q_z} && \Big]\ H_{\mathrm{opt}}\\
&+\sum_{i_1}\mathscr{E}^{\mathrm{Pe}}_{ii_1}\delta s^{\mathrm{hek}\,ji_1}_{\boldsymbol{k}\boldsymbol{k}'q_z}+\sum_{j_1}\mathscr{E}^{\mathrm{Ph}}_{jj_1}\delta s^{\mathrm{hek}\,j_1i}_{\boldsymbol{k}\boldsymbol{k}'q_z}+\sum_{i_1}B^{\mathrm{P2e}\,*ii_1}_{\boldsymbol{k}'-\boldsymbol{k},q_z}p_{ji_1\boldsymbol{k}}+\sum_{j_1}B^{\mathrm{P2h}\,*jj_1}_{\boldsymbol{k}'-\boldsymbol{k},q_z}p_{j_1i\boldsymbol{k}'} && \Big]\ H_{\mathrm{Fr}}\ (2\mathrm{nd})\\
&+\sum_{i_1i_2}p_{ji_2\boldsymbol{k}}g^{i_1i_2}_{\boldsymbol{q}}f^{\mathrm{e}}_{i_1i\boldsymbol{k}'}-\sum_{j_1j_2}p_{j_2i\boldsymbol{k}'}g^{j_2j_1}_{\boldsymbol{q}}f^{\mathrm{h}}_{j_1j\boldsymbol{k}} && \Big]\\
&+\sum_{i_1}\left(\mathscr{E}^{\mathrm{Ce}}_{ii_1\boldsymbol{k}'}\delta s^{\mathrm{hek}\,ji_1}_{\boldsymbol{k}\boldsymbol{k}'q_z}-\mathscr{U}^{\mathrm{C}}_{i_1j\boldsymbol{k}}\delta s^{\mathrm{e}*\,ii_1}_{\boldsymbol{k}\boldsymbol{k}'q_z}\right) && \Big]\\
&+\sum_{j_1}\left(\mathscr{E}^{\mathrm{Ch}}_{jj_1\boldsymbol{k}}\delta s^{\mathrm{hek}\,j_1i}_{\boldsymbol{k}\boldsymbol{k}'q_z}-\mathscr{U}^{\mathrm{C}}_{ij_1\boldsymbol{k}'}\delta s^{\mathrm{h}*\,jj_1}_{\boldsymbol{k}\boldsymbol{k}'q_z}\right) && \Big]\ H_{\mathrm{Cb}}\ (\mathrm{MF})\\
&+\sum_{i_1}\left(\mathscr{E}^{\mathrm{Cse}*}_{i_1i\boldsymbol{k}\boldsymbol{k}'q_z}p_{ji_1\boldsymbol{k}}-\mathscr{U}^{\mathrm{Cshek}}_{i_1j\boldsymbol{k}\boldsymbol{k}'q_z}f^{\mathrm{e}}_{i_1i\boldsymbol{k}'}\right) && \Big]\\
&+\sum_{j_1}\left(\mathscr{E}^{\mathrm{Csh}*}_{j_1j\boldsymbol{k}\boldsymbol{k}'q_z}p_{j_1i\boldsymbol{k}'}-\mathscr{U}^{\mathrm{Cshek}}_{ij_1\boldsymbol{k}\boldsymbol{k}'q_z}f^{\mathrm{h}}_{j_1j\boldsymbol{k}}\right)+\mathscr{U}^{\mathrm{Cshek}}_{ij\boldsymbol{k}\boldsymbol{k}'q_z} && \Big]\ H_{\mathrm{Cb}}\ (>\mathrm{MF})
\end{aligned}
$$

$$
\begin{aligned}
\mathrm{i}\hbar\frac{\mathrm{d}}{\mathrm{d}t}\delta n_{\boldsymbol{k}q_zq_z'} = \ & 2^*\sum_{i_1i_2}\left(-g^{i_1i_2}_{\boldsymbol{k}+q_z\boldsymbol{e}_z}\delta S^{\mathrm{e}\,i_1i_2}_{\boldsymbol{k}q_z'}+g^{*i_1i_2}_{\boldsymbol{k}+q_z'\boldsymbol{e}_z}\delta S^{\mathrm{e}*\,i_1i_2}_{\boldsymbol{k}q_z}\right) && \Big]\\
&+2^*\sum_{j_1j_2}\left(g^{j_2j_1}_{\boldsymbol{k}+q_z\boldsymbol{e}_z}\delta S^{\mathrm{h}\,j_1j_2}_{\boldsymbol{k}q_z'}-g^{*j_2j_1}_{\boldsymbol{k}+q_z'\boldsymbol{e}_z}\delta S^{\mathrm{h}*\,j_1j_2}_{\boldsymbol{k}q_z}\right) && \Big]\ H_{\mathrm{Fr}}\ (2\mathrm{nd\ order})
\end{aligned}
$$

$$
\begin{aligned}
\mathrm{i}\hbar\frac{\mathrm{d}}{\mathrm{d}t}\delta b_{\boldsymbol{k}q_zq_z'} = \ & 2\hbar\omega_{\mathrm{LO}}\,\delta b_{\boldsymbol{k}q_zq_z'} && \Big]\ H_0\\
&+2^*\sum_{i_1i_2}\left(g^{*i_1i_2}_{-\boldsymbol{k}+q_z'\boldsymbol{e}_z}\delta S^{\mathrm{e}\,i_2i_1}_{\boldsymbol{k}q_z}+g^{*i_1i_2}_{\boldsymbol{k}+q_z\boldsymbol{e}_z}\delta S^{\mathrm{e}\,i_2i_1}_{\boldsymbol{k}q_z'}\right) && \Big]\\
&+2^*\sum_{j_1j_2}\left(-g^{*j_2j_1}_{-\boldsymbol{k}+q_z'\boldsymbol{e}_z}\delta S^{\mathrm{h}\,j_2j_1}_{\boldsymbol{k}q_z}-g^{*j_2j_1}_{\boldsymbol{k}+q_z\boldsymbol{e}_z}\delta S^{\mathrm{h}\,j_2j_1}_{\boldsymbol{k}q_z'}\right) && \Big]\ H_{\mathrm{Fr}}\ (2\mathrm{nd\ order})
\end{aligned}
$$

5.4 Order separation

5.4.1 State vector formulation

State vector components

For phonon variables up to order $E^2 g^2$

$$
\begin{aligned}
\left|\psi^{\mathrm{cd(1,0)}}\right\rangle &= \sum_{ijk} \alpha^{\mathrm{cd(1,0)}}_{ijk} c^\dagger_{ik} d^\dagger_{j-k} |0\rangle \\
\left|\psi^{\mathrm{cdb(1,1)}}\right\rangle &= \sum_{ijkk'q_z} \alpha^{\mathrm{cdb(1,1)}}_{ijkk'q_z} c^\dagger_{ik} d^\dagger_{j-k'} b^\dagger_{k'-k+q_z e_z} |0\rangle \\
\left|\psi^{\mathrm{cdbb(1,2)}}\right\rangle &= \sum_{ijkk'q_z} \alpha^{\mathrm{cdbb(1,2)}}_{ijkk'q_z} c^\dagger_{ik} d^\dagger_{j-k'} b^\dagger_{k'-k+q_z e_z} b^\dagger_0 |0\rangle \\
\left|\psi^{\mathrm{b(2,1)}}\right\rangle &= \sum_{q_z} \alpha^{\mathrm{b(2,1)}}_{q_z} b^\dagger_{q_z e_z} |0\rangle \\
\left|\psi^{\mathrm{bb(2,2)}}\right\rangle &= \alpha^{\mathrm{bb(2,2)}} b^\dagger_0 b^\dagger_0 |0\rangle
\end{aligned}
$$

For phonon variables up to order $E^2 g^4$

$$
\begin{aligned}
\left|\psi^{\mathrm{cd(1,2)}}\right\rangle &= \sum_{ijk} \alpha^{\mathrm{cd(1,2)}}_{ijk} c^\dagger_{ik} d^\dagger_{j-k} |0\rangle \\
\left|\psi^{\mathrm{cdb(1,3)}}\right\rangle &= \sum_{ijk} \alpha^{\mathrm{cdb(1,3)}}_{ijk} c^\dagger_{ik} d^\dagger_{j-k} b^\dagger_0 |0\rangle \\
\left|\psi^{\mathrm{cdbb(1,4)}}\right\rangle &= \sum_{ijk} \alpha^{\mathrm{cdbb(1,4)}}_{ijk} c^\dagger_{ik} d^\dagger_{j-k} b^\dagger_0 b^\dagger_0 |0\rangle \\
\left|\psi^{\mathrm{cdbbb(1,3)}}\right\rangle &= \sum_{ijkk'q_z} \alpha^{\mathrm{cdbbb(1,3)}}_{ijkk'q_z} c^\dagger_{ik} d^\dagger_{j-k'} b^\dagger_{k'-k+q_z e_z} b^\dagger_0 b^\dagger_0 |0\rangle \\
\left|\psi^{\mathrm{b(2,3)}}\right\rangle &= \alpha^{\mathrm{b(2,3)}} b^\dagger_0 |0\rangle \\
\left|\psi^{\mathrm{bb(2,4)}}\right\rangle &= \alpha^{\mathrm{bb(2,4)}} b^\dagger_0 b^\dagger_0 |0\rangle
\end{aligned}
$$

Equations of motion

Energy-dependent phase oscillation; $(\mathrm{b})^{\mathrm{n}}$ means n phonon operators, $n = 0$ is allowed

$$
\begin{aligned}
\mathrm{i}\hbar \frac{\mathrm{d}}{\mathrm{d}t} \alpha^{\mathrm{cd(b)^n}}_{ijk} \Big|^{H_0} &= \left(\varepsilon^{\mathrm{e}}_{ik} + \varepsilon^{\mathrm{h}}_{jk} + n \cdot \hbar\omega_{\mathrm{LO}}\right) \alpha^{\mathrm{cd(b)^n}}_{ijk} \\
\mathrm{i}\hbar \frac{\mathrm{d}}{\mathrm{d}t} \alpha^{\mathrm{cd(b)^n}}_{ijkk'q_z} \Big|^{H_0} &= \left(\varepsilon^{\mathrm{e}}_{ik} + \varepsilon^{\mathrm{h}}_{jk'} + n \cdot \hbar\omega_{\mathrm{LO}}\right) \alpha^{\mathrm{cd(b)^n}}_{ijkk'q_z} \\
\mathrm{i}\hbar \frac{\mathrm{d}}{\mathrm{d}t} \alpha^{\mathrm{(b)^n}}_{q_z} \Big|^{H_0} &= n \cdot \hbar\omega_{\mathrm{LO}}\, \alpha^{\mathrm{cd(b)^n}}_{q_z}
\end{aligned}
$$

Coulomb interaction

$$
\begin{aligned}
\mathrm{i}\hbar \frac{\mathrm{d}}{\mathrm{d}t} \alpha^{\mathrm{cd(b)^n}}_{ijk} \Big|^{H_{\mathrm{Cb}}} &= -\sum_{i_1 j_1 k_1} V^{i j_1 j i_1}_{k_1} \alpha^{\mathrm{cd(b)^n}}_{i_1 j_1, k-k_1} \\
\mathrm{i}\hbar \frac{\mathrm{d}}{\mathrm{d}t} \alpha^{\mathrm{cd(b)^n}}_{ijkk'q_z} \Big|^{H_{\mathrm{Cb}}} &= -\sum_{i_1 j_1 k_1} V^{i j_1 j i_1}_{k_1} \alpha^{\mathrm{cd(b)^n}}_{i_1 j_1, k-k_1, k'-k_1, q_z}
\end{aligned}
$$

For phonon variables up to order $E^2 g^2$

$$
\begin{aligned}
\mathrm{i}\hbar\frac{\mathrm{d}}{\mathrm{d}t}\alpha^{\mathrm{cd}(1,0)}_{ij\boldsymbol{k}}\Big|^{H_{\mathrm{opt}}} &= -\boldsymbol{E}\cdot\boldsymbol{M}_{ij}\\
\mathrm{i}\hbar\frac{\mathrm{d}}{\mathrm{d}t}\alpha^{\mathrm{cdb}(1,1)}_{ij\boldsymbol{k}\boldsymbol{k}'q_{\mathrm{z}}}\Big|^{H_{\mathrm{Fr}}} &= \sum_{i_1} g^{*i_1 i}_{\boldsymbol{k}'-\boldsymbol{k}+q_{\mathrm{z}}\boldsymbol{e}_{\mathrm{z}}}\alpha^{\mathrm{cd}(1,0)}_{i_1 j\boldsymbol{k}'} - \sum_{j_1} g^{*j j_1}_{\boldsymbol{k}'-\boldsymbol{k}+q_{\mathrm{z}}\boldsymbol{e}_{\mathrm{z}}}\alpha^{\mathrm{cd}(1,0)}_{ij_1\boldsymbol{k}}\\
\mathrm{i}\hbar\frac{\mathrm{d}}{\mathrm{d}t}\alpha^{\mathrm{cdbb}(1,2)}_{ij\boldsymbol{k}\boldsymbol{k}'q_{\mathrm{z}}}\Big|^{H_{\mathrm{Fr}}} &= \sum_{i_1}\Big[g^{*i_1 i}_{\boldsymbol{k}'-\boldsymbol{k}+q_{\mathrm{z}}\boldsymbol{e}_{\mathrm{z}}}\alpha^{\mathrm{cdb}(1,1)}_{i_1 j\boldsymbol{k}'\boldsymbol{k}'0} + \big(1-\delta_{\boldsymbol{k}\boldsymbol{k}'}\delta_{q_{\mathrm{z}},0}\big)g^{*i_1 i}_{0}\alpha^{\mathrm{cdb}(1,1)}_{i_1 j\boldsymbol{k}\boldsymbol{k}'q_{\mathrm{z}}}\Big]\\
&\quad -\sum_{j_1}\Big[g^{*j j_1}_{\boldsymbol{k}'-\boldsymbol{k}+q_{\mathrm{z}}\boldsymbol{e}_{\mathrm{z}}}\alpha^{\mathrm{cdb}(1,1)}_{ij_1\boldsymbol{k}\boldsymbol{k}0} + \big(1-\delta_{\boldsymbol{k}\boldsymbol{k}'}\delta_{q_{\mathrm{z}},0}\big)g^{*j j_1}_{0}\alpha^{\mathrm{cdb}(1,1)}_{ij_1\boldsymbol{k}\boldsymbol{k}'q_{\mathrm{z}}}\Big]\\
\mathrm{i}\hbar\frac{\mathrm{d}}{\mathrm{d}t}\alpha^{\mathrm{b}(2,1)}_{q_{\mathrm{z}}}\Big|^{H_{\mathrm{opt}}} &= -\sum_{i_1 j_1\boldsymbol{k}_1}\boldsymbol{E}\cdot\boldsymbol{M}^{*}_{i_1 j_1}\alpha^{\mathrm{cdb}(1,1)}_{i_1 j_1\boldsymbol{k}_1\boldsymbol{k}_1 q_{\mathrm{z}}}\\
\mathrm{i}\hbar\frac{\mathrm{d}}{\mathrm{d}t}\alpha^{\mathrm{bb}(2,2)}\Big|^{H_{\mathrm{opt}}} &= -\sum_{i_1 j_1\boldsymbol{k}_1}\boldsymbol{E}\cdot\boldsymbol{M}^{*}_{i_1 j_1}\alpha^{\mathrm{cdbb}(1,2)}_{i_1 j_1\boldsymbol{k}_1\boldsymbol{k}_1 0}
\end{aligned}
$$

For phonon variables up to order $E^2 g^4$

$$
\begin{aligned}
\mathrm{i}\hbar\frac{\mathrm{d}}{\mathrm{d}t}\alpha^{\mathrm{cd}(1,2)}_{ij\boldsymbol{k}}\Big|^{H_{\mathrm{Fr}}} &= \sum_{i_1\boldsymbol{k}_1 q_{1\mathrm{z}}} g^{i i_1}_{\boldsymbol{k}_1+q_{1\mathrm{z}}\boldsymbol{e}_{\mathrm{z}}}\alpha^{\mathrm{cdb}(1,1)}_{i_1 j,\boldsymbol{k}_1+\boldsymbol{k},\boldsymbol{k}q_{1\mathrm{z}}} - \sum_{j_1\boldsymbol{k}_1 q_{1\mathrm{z}}} g^{j_1 j}_{\boldsymbol{k}_1+q_{1\mathrm{z}}\boldsymbol{e}_{\mathrm{z}}}\alpha^{\mathrm{cdb}(1,1)}_{ij_1\boldsymbol{k},\boldsymbol{k}_1+\boldsymbol{k},q_{1\mathrm{z}}}\\
\mathrm{i}\hbar\frac{\mathrm{d}}{\mathrm{d}t}\alpha^{\mathrm{cdb}(1,3)}_{ij\boldsymbol{k}}\Big|^{H_{\mathrm{Fr}}^{\mathrm{ann}}} &= \sum_{i_1\boldsymbol{k}_1 q_{1\mathrm{z}}} g^{i i_1}_{\boldsymbol{k}_1+q_{1\mathrm{z}}\boldsymbol{e}_{\mathrm{z}}}\alpha^{\mathrm{cdbb}(1,2)}_{i_1 j,\boldsymbol{k}_1+\boldsymbol{k},\boldsymbol{k}q_{1\mathrm{z}}} + \sum_{i_1} g^{i i_1}_{0}\alpha^{\mathrm{cdbb}(1,2)}_{i_1 j\boldsymbol{k}\boldsymbol{k}0}\\
&\quad - \sum_{j_1\boldsymbol{k}_1 q_{1\mathrm{z}}} g^{j_1 j}_{\boldsymbol{k}_1+q_{1\mathrm{z}}\boldsymbol{e}_{\mathrm{z}}}\alpha^{\mathrm{cdbb}(1,2)}_{ij_1\boldsymbol{k},\boldsymbol{k}_1+\boldsymbol{k},q_{1\mathrm{z}}} - \sum_{j_1} g^{j_1 j}_{0}\alpha^{\mathrm{cdbb}(1,2)}_{ij_1\boldsymbol{k}\boldsymbol{k}0}\\
\mathrm{i}\hbar\frac{\mathrm{d}}{\mathrm{d}t}\alpha^{\mathrm{cdb}(1,3)}_{ij\boldsymbol{k}}\Big|^{H_{\mathrm{Fr}}^{\mathrm{creat}}} &= \sum_{i_1} g^{*i_1 i}_{0}\alpha^{\mathrm{cd}(1,2)}_{i_1 j\boldsymbol{k}} - \sum_{j_1} g^{*j j_1}_{0}\alpha^{\mathrm{cd}(1,2)}_{ij_1\boldsymbol{k}}\\
\mathrm{i}\hbar\frac{\mathrm{d}}{\mathrm{d}t}\alpha^{\mathrm{cdbb}(1,4)}_{ij\boldsymbol{k}}\Big|^{H_{\mathrm{Fr}}^{\mathrm{ann}}} &= \sum_{i_1\boldsymbol{k}_1 q_{1\mathrm{z}}} g^{i i_1}_{\boldsymbol{k}_1+q_{1\mathrm{z}}\boldsymbol{e}_{\mathrm{z}}}\alpha^{\mathrm{cdbbb}(1,3)}_{i_1 j,\boldsymbol{k}_1+\boldsymbol{k},\boldsymbol{k}q_{1\mathrm{z}}} + 2\sum_{i_1} g^{i i_1}_{0}\alpha^{\mathrm{cdbbb}(1,3)}_{i_1 j\boldsymbol{k}\boldsymbol{k}0}\\
&\quad - \sum_{j_1\boldsymbol{k}_1 q_{1\mathrm{z}}} g^{j_1 j}_{\boldsymbol{k}_1+q_{1\mathrm{z}}\boldsymbol{e}_{\mathrm{z}}}\alpha^{\mathrm{cdbbb}(1,3)}_{ij_1\boldsymbol{k},\boldsymbol{k}_1+\boldsymbol{k},q_{1\mathrm{z}}} - 2\sum_{j_1} g^{j_1 j}_{0}\alpha^{\mathrm{cdbbb}(1,3)}_{ij_1\boldsymbol{k}\boldsymbol{k}0}\\
\mathrm{i}\hbar\frac{\mathrm{d}}{\mathrm{d}t}\alpha^{\mathrm{cdbb}(1,4)}_{ij\boldsymbol{k}}\Big|^{H_{\mathrm{Fr}}^{\mathrm{creat}}} &= \sum_{i_1} g^{*i_1 i}_{0}\alpha^{\mathrm{cdb}(1,3)}_{i_1 j\boldsymbol{k}} - \sum_{j_1} g^{*j j_1}_{0}\alpha^{\mathrm{cdb}(1,3)}_{ij_1\boldsymbol{k}}\\
\mathrm{i}\hbar\frac{\mathrm{d}}{\mathrm{d}t}\alpha^{\mathrm{cdbbb}(1,3)}_{ij\boldsymbol{k}\boldsymbol{k}'q_{\mathrm{z}}}\Big|^{H_{\mathrm{Fr}}} &= \sum_{i_1}\Big[g^{*i_1 i}_{\boldsymbol{k}'-\boldsymbol{k}+q_{\mathrm{z}}\boldsymbol{e}_{\mathrm{z}}}\alpha^{\mathrm{cdbb}(1,2)}_{i_1 j\boldsymbol{k}'\boldsymbol{k}'0} + \big(1-\delta_{\boldsymbol{k}\boldsymbol{k}'}\delta_{q_{\mathrm{z}},0}\big)g^{*i_1 i}_{0}\alpha^{\mathrm{cdbb}(1,2)}_{i_1 j\boldsymbol{k}\boldsymbol{k}'q_{\mathrm{z}}}\Big]\\
&\quad -\sum_{j_1}\Big[g^{*j j_1}_{\boldsymbol{k}'-\boldsymbol{k}+q_{\mathrm{z}}\boldsymbol{e}_{\mathrm{z}}}\alpha^{\mathrm{cdbb}(1,2)}_{ij_1\boldsymbol{k}\boldsymbol{k}0} + \big(1-\delta_{\boldsymbol{k}\boldsymbol{k}'}\delta_{q_{\mathrm{z}},0}\big)g^{*j j_1}_{0}\alpha^{\mathrm{cdbb}(1,2)}_{ij_1\boldsymbol{k}\boldsymbol{k}'q_{\mathrm{z}}}\Big]\\
\mathrm{i}\hbar\frac{\mathrm{d}}{\mathrm{d}t}\alpha^{\mathrm{b}(2,3)}\Big|^{H_{\mathrm{opt}}} &= -\sum_{i_1 j_1\boldsymbol{k}_1}\boldsymbol{E}\cdot\boldsymbol{M}^{*}_{i_1 j_1}\alpha^{\mathrm{cdb}(1,3)}_{i_1 j_1\boldsymbol{k}_1}\\
\mathrm{i}\hbar\frac{\mathrm{d}}{\mathrm{d}t}\alpha^{\mathrm{bb}(2,4)}\Big|^{H_{\mathrm{opt}}} &= -\sum_{i_1 j_1\boldsymbol{k}_1}\boldsymbol{E}\cdot\boldsymbol{M}^{*}_{i_1 j_1}\alpha^{\mathrm{cdbb}(1,4)}_{i_1 j_1\boldsymbol{k}_1}
\end{aligned}
$$

Derived observables

Phonon variables up to order $E^2 g^2$

$$\begin{aligned}\left\langle b_{q_z \boldsymbol{e}_z}\right\rangle\Big|^{(2,1)} &= \left\langle 0\middle| b_{q_z \boldsymbol{e}_z}\middle|\psi^{\mathrm{b}(2,1)}\right\rangle + \left\langle \psi^{\mathrm{cd}(1,0)}\middle| b_{q_z \boldsymbol{e}_z}\middle|\psi^{\mathrm{cdb}(1,1)}\right\rangle \\ &= \alpha^{\mathrm{b}(2,1)}_{q_z} + \sum_{i_1 j_1 \boldsymbol{k_1}} \alpha^{\mathrm{cd}(1,0)*}_{i_1 j_1 \boldsymbol{k_1}} \alpha^{\mathrm{cdb}(1,1)}_{i_1 j_1 \boldsymbol{k_1} \boldsymbol{k_1} q_z}\end{aligned}$$

$$\begin{aligned}\left\langle b^\dagger_{\boldsymbol{k}+q_z \boldsymbol{e}_z} b_{\boldsymbol{k}+q'_z \boldsymbol{e}_z}\right\rangle\Big|^{(2,2)} &= \left\langle \psi^{\mathrm{cdb}(1,1)}\middle| b^\dagger_{\boldsymbol{k}+q_z \boldsymbol{e}_z} b_{\boldsymbol{k}+q'_z \boldsymbol{e}_z}\middle|\psi^{\mathrm{cdb}(1,1)}\right\rangle \\ &= \sum_{i_1 j_1 \boldsymbol{k_1}} \alpha^{\mathrm{cdb}(1,1)*}_{i_1 j_1 \boldsymbol{k_1}, \boldsymbol{k_1}+\boldsymbol{k}, q_z} \alpha^{\mathrm{cdb}(1,1)}_{i_1 j_1 \boldsymbol{k_1}, \boldsymbol{k_1}+\boldsymbol{k}, q'_z}\end{aligned}$$

$$\begin{aligned}\left\langle b_0 b_0\right\rangle\Big|^{(2,2)} &= \left\langle 0\middle| b_0 b_0\middle|\psi^{\mathrm{bb}(2,2)}\right\rangle + \left\langle \psi^{\mathrm{cd}(1,0)}\middle| b_0 b_0\middle|\psi^{\mathrm{cdbb}(1,2)}\right\rangle \\ &= 2\alpha^{\mathrm{bb}(2,2)} + 2\sum_{i_1 j_1 \boldsymbol{k_1}} \alpha^{\mathrm{cd}(1,0)*}_{i_1 j_1 \boldsymbol{k_1}} \alpha^{\mathrm{cdbb}(1,2)}_{i_1 j_1 \boldsymbol{k_1} \boldsymbol{k_1} 0}\end{aligned}$$

Additional contributions up to order $E^2 g^4$

$$\begin{aligned}\left\langle b_0\right\rangle^{(2,3)} =& \left\langle 0\middle| b_0\middle|\psi^{\mathrm{b}(2,3)}\right\rangle + \left\langle \psi^{\mathrm{cd}(1,0)}\middle| b_0\middle|\psi^{\mathrm{cdb}(1,3)}\right\rangle + \left\langle \psi^{\mathrm{cd}(1,2)}\middle| b_0\middle|\psi^{\mathrm{cdb}(1,1)}\right\rangle \\ &+ \left\langle \psi^{\mathrm{cdb}(1,1)}\middle| b_0\middle|\psi^{\mathrm{cdbb}(1,2)}\right\rangle \\ =& \alpha^{\mathrm{b}(2,3)} + \sum_{i_1 j_1 \boldsymbol{k_1}} \alpha^{\mathrm{cd}(1,0)*}_{i_1 j_1 \boldsymbol{k_1}} \alpha^{\mathrm{cdb}(1,3)}_{i_1 j_1 \boldsymbol{k_1}} + \sum_{i_1 j_1 \boldsymbol{k_1}} \alpha^{\mathrm{cd}(1,2)*}_{i_1 j_1 \boldsymbol{k_1}} \alpha^{\mathrm{cdb}(1,1)}_{i_1 j_1 \boldsymbol{k_1} \boldsymbol{k_1} 0} \\ &+ \sum_{i_1 j_1 \boldsymbol{k_1} \boldsymbol{k_2} q_{1z}} \alpha^{\mathrm{cdb}(1,1)*}_{i_1 j_1 \boldsymbol{k_1} \boldsymbol{k_2} q_{1z}} \alpha^{\mathrm{cdbb}(1,2)}_{i_1 j_1 \boldsymbol{k_1} \boldsymbol{k_2} q_{1z}} + \sum_{i_1 j_1 \boldsymbol{k_1}} \alpha^{\mathrm{cdb}(1,1)*}_{i_1 j_1 \boldsymbol{k_1} \boldsymbol{k_1} 0} \alpha^{\mathrm{cdbb}(1,2)}_{i_1 j_1 \boldsymbol{k_1} \boldsymbol{k_1} 0}\end{aligned}$$

$$\begin{aligned}\left\langle b^\dagger_0 b_0\right\rangle^{(2,4)} =& 2\,\mathrm{Re}\left\langle \psi^{\mathrm{cdb}(1,1)}\middle| b^\dagger_0 b_0\middle|\psi^{\mathrm{cdb}(1,3)}\right\rangle + \left\langle \psi^{\mathrm{cdbb}(1,2)}\middle| b^\dagger_0 b_0\middle|\psi^{\mathrm{cdbb}(1,2)}\right\rangle \\ =& 2\,\mathrm{Re}\sum_{i_1 j_1 \boldsymbol{k_1}} \alpha^{\mathrm{cdb}(1,1)*}_{i_1 j_1 \boldsymbol{k_1} \boldsymbol{k_1} 0} \alpha^{\mathrm{cdb}(1,3)}_{i_1 j_1 \boldsymbol{k_1}} \\ &+ \sum_{i_1 j_1 \boldsymbol{k_1} \boldsymbol{k_2} q_{1z}} \left|\alpha^{\mathrm{cdbb}(1,2)}_{i_1 j_1 \boldsymbol{k_1} \boldsymbol{k_2} q_{1z}}\right|^2 + 3\sum_{i_1 j_1 \boldsymbol{k_1}} \left|\alpha^{\mathrm{cdbb}(1,2)}_{i_1 j_1 \boldsymbol{k_1} \boldsymbol{k_1} 0}\right|^2\end{aligned}$$

$$\begin{aligned}\left\langle b_0 b_0\right\rangle^{(2,4)} =& \left\langle 0\middle| b_0 b_0\middle|\psi^{\mathrm{bb}(2,4)}\right\rangle + \left\langle \psi^{\mathrm{cd}(1,0)}\middle| b_0 b_0\middle|\psi^{\mathrm{cdbb}(1,4)}\right\rangle + \left\langle \psi^{\mathrm{cd}(1,2)}\middle| b_0 b_0\middle|\psi^{\mathrm{cdbb}(1,2)}\right\rangle \\ &+ \left\langle \psi^{\mathrm{cdb}(1,1)}\middle| b_0 b_0\middle|\psi^{\mathrm{cdbbb}(1,3)}\right\rangle \\ =& 2\alpha^{\mathrm{bb}(2,4)} + 2\sum_{i_1 j_1 \boldsymbol{k_1}} \alpha^{\mathrm{cd}(1,0)*}_{i_1 j_1 \boldsymbol{k_1}} \alpha^{\mathrm{cdbb}(1,4)}_{i_1 j_1 \boldsymbol{k_1}} + 2\sum_{i_1 j_1 \boldsymbol{k_1}} \alpha^{\mathrm{cd}(1,2)*}_{i_1 j_1 \boldsymbol{k_1}} \alpha^{\mathrm{cdbb}(1,2)}_{i_1 j_1 \boldsymbol{k_1} \boldsymbol{k_1} 0} \\ &+ 2\sum_{i_1 j_1 \boldsymbol{k_1} \boldsymbol{k_2} q_{1z}} \alpha^{\mathrm{cdb}(1,1)*}_{i_1 j_1 \boldsymbol{k_1} \boldsymbol{k_2} q_{1z}} \alpha^{\mathrm{cdbbb}(1,3)}_{i_1 j_1 \boldsymbol{k_1} \boldsymbol{k_2} q_{1z}} + 4\sum_{i_1 j_1 \boldsymbol{k_1}} \alpha^{\mathrm{cdb}(1,1)*}_{i_1 j_1 \boldsymbol{k_1} \boldsymbol{k_1} 0} \alpha^{\mathrm{cdbbb}(1,3)}_{i_1 j_1 \boldsymbol{k_1} \boldsymbol{k_1} 0}\end{aligned}$$

Electronic variables up to order $E^2 g^2$

$$\begin{aligned}\left\langle d_{j-\boldsymbol{k}} c_{i\boldsymbol{k}}\right\rangle^{\leq(1,2)} =& \left\langle 0\middle| d_{j-\boldsymbol{k}} c_{i\boldsymbol{k}}\middle|\psi^{\mathrm{cd}(1,0)}\right\rangle + \left\langle 0\middle| d_{j-\boldsymbol{k}} c_{i\boldsymbol{k}}\middle|\psi^{\mathrm{cd}(1,2)}\right\rangle \\ =& \alpha^{\mathrm{cd}(1,0)}_{ij\boldsymbol{k}} + \alpha^{\mathrm{cd}(1,2)}_{ij\boldsymbol{k}}\end{aligned}$$

$$\begin{aligned}\left\langle c^\dagger_{i\boldsymbol{k}} c_{i'\boldsymbol{k}}\right\rangle^{\leq(2,2)} =& \left\langle \psi^{\mathrm{cd}(1,0)}\middle| c^\dagger_{i\boldsymbol{k}} c_{i'\boldsymbol{k}}\middle|\psi^{\mathrm{cd}(1,0)}\right\rangle + \left\langle \psi^{\mathrm{cd}(1,2)}\middle| c^\dagger_{i\boldsymbol{k}} c_{i'\boldsymbol{k}}\middle|\psi^{\mathrm{cd}(1,0)}\right\rangle \\ &+ \left\langle \psi^{\mathrm{cd}(1,0)}\middle| c^\dagger_{i\boldsymbol{k}} c_{i'\boldsymbol{k}}\middle|\psi^{\mathrm{cd}(1,2)}\right\rangle + \left\langle \psi^{\mathrm{cdb}(1,1)}\middle| c^\dagger_{i\boldsymbol{k}} c_{i'\boldsymbol{k}}\middle|\psi^{\mathrm{cdb}(1,1)}\right\rangle \\ =& \sum_{j_1} \alpha^{\mathrm{cd}(1,0)*}_{i j_1 \boldsymbol{k}} \alpha^{\mathrm{cd}(1,0)}_{i' j_1 \boldsymbol{k}} + \sum_{j_1} \alpha^{\mathrm{cd}(1,2)*}_{i j_1 \boldsymbol{k}} \alpha^{\mathrm{cd}(1,0)}_{i' j_1 \boldsymbol{k}} + \sum_{j_1} \alpha^{\mathrm{cd}(1,0)*}_{i j_1 \boldsymbol{k}} \alpha^{\mathrm{cd}(1,2)}_{i' j_1 \boldsymbol{k}} \\ &+ \sum_{j_1 \boldsymbol{k_1} q_{1\mathrm{z}}} \alpha^{\mathrm{cdb}(1,1)*}_{i j_1 \boldsymbol{k} \boldsymbol{k_1} q_{1\mathrm{z}}} \alpha^{\mathrm{cdb}(1,1)}_{i' j_1 \boldsymbol{k} \boldsymbol{k_1} q_{1\mathrm{z}}}\end{aligned}$$

$$\begin{aligned}\left\langle d^\dagger_{i\boldsymbol{k}} d_{j'\boldsymbol{k}}\right\rangle^{\leq(2,2)} =& \left\langle \psi^{\mathrm{cd}(1,0)}\middle| d^\dagger_{j\boldsymbol{k}} d_{j'\boldsymbol{k}}\middle|\psi^{\mathrm{cd}(1,0)}\right\rangle + \left\langle \psi^{\mathrm{cd}(1,2)}\middle| d^\dagger_{j\boldsymbol{k}} d_{j'\boldsymbol{k}}\middle|\psi^{\mathrm{cd}(1,0)}\right\rangle \\ &+ \left\langle \psi^{\mathrm{cd}(1,0)}\middle| d^\dagger_{j\boldsymbol{k}} d_{j'\boldsymbol{k}}\middle|\psi^{\mathrm{cd}(1,2)}\right\rangle + \left\langle \psi^{\mathrm{cdb}(1,1)}\middle| d^\dagger_{j\boldsymbol{k}} d_{j'\boldsymbol{k}}\middle|\psi^{\mathrm{cdb}(1,1)}\right\rangle \\ =& \sum_{i_1} \alpha^{\mathrm{cd}(1,0)*}_{i_1 j \boldsymbol{k}} \alpha^{\mathrm{cd}(1,0)}_{i_1 j' \boldsymbol{k}} + \sum_{i_1} \alpha^{\mathrm{cd}(1,2)*}_{i_1 j \boldsymbol{k}} \alpha^{\mathrm{cd}(1,0)}_{i_1 j' \boldsymbol{k}} + \sum_{i_1} \alpha^{\mathrm{cd}(1,0)*}_{i_1 j \boldsymbol{k}} \alpha^{\mathrm{cd}(1,2)}_{i_1 j' \boldsymbol{k}} \\ &+ \sum_{i_1 \boldsymbol{k_1} q_{1\mathrm{z}}} \alpha^{\mathrm{cdb}(1,1)*}_{i_1 j \boldsymbol{k_1} \boldsymbol{k} q_{1\mathrm{z}}} \alpha^{\mathrm{cdb}(1,1)}_{i_1 j' \boldsymbol{k_1} \boldsymbol{k} q_{1\mathrm{z}}}\end{aligned}$$

5.4.2 Density matrix formulation

The dynamical variables and the interaction matrices are defined in the section on correlation expansion (5.3). Throughout this section the definition $\boldsymbol{q} = \boldsymbol{k'} - \boldsymbol{k} + q_{\mathrm{z}}\boldsymbol{e}_{\mathrm{z}}$ is implied. n_{B} is the population number of thermally excited LO phonons.

$$\begin{aligned}
\mathrm{i}\hbar\frac{\mathrm{d}}{\mathrm{d}t} f^{\mathrm{e}(2,0)}_{ii'\boldsymbol{k}} =& \left(\varepsilon^{\mathrm{e}}_{i'\boldsymbol{k}} - \varepsilon^{\mathrm{e}}_{i\boldsymbol{k}}\right) f^{\mathrm{e}(2,0)}_{ii'\boldsymbol{k}} && \Big] H_0 \\
&+ \sum_{j_1} \left(- \boldsymbol{E}\cdot\boldsymbol{M}_{i'j_1} p^{(1,0)*}_{j_1 i\boldsymbol{k}} + \boldsymbol{E}\cdot\boldsymbol{M}^*_{ij_1} p^{(1,0)}_{j_1 i'\boldsymbol{k}}\right) && \Big] H_{\mathrm{opt}} \\
&+ \sum_{j_1} \left(\mathscr{U}^{\mathrm{C}(1,0)}_{i'j_1\boldsymbol{k}} p^{(1,0)*}_{j_1 i\boldsymbol{k}} - \mathscr{U}^{\mathrm{C}(1,0)*}_{ij_1\boldsymbol{k}} p^{(1,0)}_{j_1 i'\boldsymbol{k}}\right) && \Big] H_{\mathrm{Cb}} \\
\mathrm{i}\hbar\frac{\mathrm{d}}{\mathrm{d}t} f^{\mathrm{h}(2,0)}_{jj'\boldsymbol{k}} =& \left(\varepsilon^{\mathrm{h}}_{j'\boldsymbol{k}} - \varepsilon^{\mathrm{h}}_{j\boldsymbol{k}}\right) f^{\mathrm{h}(2,0)}_{jj'\boldsymbol{k}} && \Big] H_0 \\
&+ \sum_{i_1} \left(- \boldsymbol{E}\cdot\boldsymbol{M}_{i_1 j'} p^{(1,0)*}_{j i_1\boldsymbol{k}} + \boldsymbol{E}\cdot\boldsymbol{M}^*_{i_1 j} p^{(1,0)}_{j' i_1\boldsymbol{k}}\right) && \Big] H_{\mathrm{opt}} \\
&+ \sum_{i_1} \left(\mathscr{U}^{\mathrm{C}(1,0)}_{i_1 j'\boldsymbol{k}} p^{(1,0)*}_{j i_1\boldsymbol{k}} - \mathscr{U}^{\mathrm{C}(1,0)*}_{i_1 j\boldsymbol{k}} p^{(1,0)}_{j' i_1\boldsymbol{k}}\right) && \Big] H_{\mathrm{Cb}} \\
\mathrm{i}\hbar\frac{\mathrm{d}}{\mathrm{d}t} p^{(1,0)}_{ji\boldsymbol{k}} =& \left(\varepsilon^{\mathrm{e}}_{i\boldsymbol{k}} + \varepsilon^{\mathrm{h}}_{j\boldsymbol{k}}\right) p^{(1,0)}_{ji\boldsymbol{k}} && \Big] H_0 \\
&- \boldsymbol{E}\cdot\boldsymbol{M}_{ij} && \Big] H_{\mathrm{opt}} \\
&+ \mathscr{U}^{\mathrm{C}(1,0)}_{ij\boldsymbol{k}} && \Big] H_{\mathrm{Cb}}
\end{aligned}$$

$$
\begin{aligned}
&\mathrm{i}\hbar\frac{\mathrm{d}}{\mathrm{d}t}\delta s^{\mathrm{e}(2,1)ii'}_{\boldsymbol{k}\boldsymbol{k}'q_z} = \left(\varepsilon^{\mathrm{e}}_{i'\boldsymbol{k}} - \varepsilon^{\mathrm{e}}_{i\boldsymbol{k}'} + \hbar\omega_{\mathrm{LO}}\right)\delta s^{\mathrm{e}(2,1)ii'}_{\boldsymbol{k}\boldsymbol{k}'q_z} && \Big] H_0\\
&\quad - \sum_{j_1} \boldsymbol{E}\cdot\boldsymbol{M}_{i'j_1}\delta s^{\mathrm{hek}(1,1)*j_1 i}_{\boldsymbol{k}\boldsymbol{k}'q_z} + \sum_{j_1} \boldsymbol{E}\cdot\boldsymbol{M}^{*}_{ij_1}\delta s^{\mathrm{he}(1,1)j_1 i'}_{\boldsymbol{k}\boldsymbol{k}'q_z} && \Big] H_{\mathrm{opt}}\\
&\quad + \sum_{i_1}\left[(1+n_{\mathrm{B}})g^{*i_1 i'}_{\boldsymbol{q}} f^{\mathrm{e}(2,0)}_{ii_1\boldsymbol{k}'} - n_{\mathrm{B}} g^{*ii_1}_{\boldsymbol{q}} f^{\mathrm{e}(2,0)}_{i_1 i'\boldsymbol{k}}\right] - \sum_{j_1 j_2} g^{*j_2 j_1}_{\boldsymbol{q}}\, p^{(1,0)*}_{j_2 i\boldsymbol{k}'}\, p^{(1,0)}_{j_1 i'\boldsymbol{k}} && \Big] H_{\mathrm{Fr}}\\
&\quad + \sum_{j_1}\left(\mathscr{U}^{\mathrm{C}(1,0)}_{i'j_1\boldsymbol{k}}\delta s^{\mathrm{hek}(1,1)*j_1 i}_{\boldsymbol{k}\boldsymbol{k}'q_z} - \mathscr{U}^{\mathrm{C}(1,0)*}_{ij_1\boldsymbol{k}'}\delta s^{\mathrm{he}(1,1)j_1 i'}_{\boldsymbol{k}\boldsymbol{k}'q_z}\right)\\
&\quad + \sum_{j_1}\left(\mathscr{U}^{\mathrm{Cshe}(1,1)}_{i'j_1\boldsymbol{k}\boldsymbol{k}'q_z} p^{(1,0)*}_{j_1 i\boldsymbol{k}'} - \mathscr{U}^{\mathrm{Cshek}(1,1)*}_{ij_1\boldsymbol{k}\boldsymbol{k}'q_z} p^{(1,0)}_{j_1 i'\boldsymbol{k}}\right) && \Big] H_{\mathrm{Cb}}
\end{aligned}
$$

$$
\begin{aligned}
&\mathrm{i}\hbar\frac{\mathrm{d}}{\mathrm{d}t}\delta s^{\mathrm{h}(2,1)jj'}_{\boldsymbol{k}\boldsymbol{k}'q_z} = \left(\varepsilon^{\mathrm{h}}_{j'\boldsymbol{k}'} - \varepsilon^{\mathrm{h}}_{j\boldsymbol{k}} + \hbar\omega_{\mathrm{LO}}\right)\delta s^{\mathrm{h}(2,1)jj'}_{\boldsymbol{k}\boldsymbol{k}'q_z} && \Big] H_0\\
&\quad - \sum_{i_1} \boldsymbol{E}\cdot\boldsymbol{M}_{i_1 j'}\delta s^{\mathrm{hek}(1,1)*ji_1}_{\boldsymbol{k}\boldsymbol{k}'q_z} + \sum_{i_1} \boldsymbol{E}\cdot\boldsymbol{M}^{*}_{i_1 j}\delta s^{\mathrm{he}(1,1)j'i_1}_{\boldsymbol{k}\boldsymbol{k}'q_z} && \Big] H_{\mathrm{opt}}\\
&\quad - \sum_{j_1}\left[(1+n_{\mathrm{B}})g^{*j'j_1}_{\boldsymbol{q}} f^{\mathrm{h}(2,0)}_{jj_1\boldsymbol{k}} - n_{\mathrm{B}} g^{j_1 j}_{\boldsymbol{q}} f^{\mathrm{h}(2,0)}_{j_1 j'\boldsymbol{k}'}\right] + \sum_{i_1 i_2} g^{*i_1 i_2}_{\boldsymbol{q}}\, p^{(1,0)}_{j'i_1\boldsymbol{k}'} p^{(1,0)*}_{ji_2\boldsymbol{k}} && \Big] H_{\mathrm{Fr}}\\
&\quad + \sum_{i_1}\left(\mathscr{U}^{\mathrm{C}(1,0)}_{i_1 j'\boldsymbol{k}'}\delta s^{\mathrm{hek}(1,1)*ji_1}_{\boldsymbol{k}\boldsymbol{k}'q_z} - \mathscr{U}^{\mathrm{C}(1,0)*}_{i_1 j\boldsymbol{k}}\delta s^{\mathrm{he}(1,1)j'i_1}_{\boldsymbol{k}\boldsymbol{k}'q_z}\right)\\
&\quad + \sum_{i_1}\left(\mathscr{U}^{\mathrm{Cshe}(1,1)}_{i_1 j'\boldsymbol{k}\boldsymbol{k}'q_z} p^{(1,0)*}_{ji_1\boldsymbol{k}} - \mathscr{U}^{\mathrm{Cshek}(1,1)*}_{i_1 j\boldsymbol{k}\boldsymbol{k}'q_z} p^{(1,0)}_{j'i_1\boldsymbol{k}'}\right) && \Big] H_{\mathrm{Cb}}
\end{aligned}
$$

$$
\begin{aligned}
&\mathrm{i}\hbar\frac{\mathrm{d}}{\mathrm{d}t}\delta s^{\mathrm{he}(1,1)ji}_{\boldsymbol{k}\boldsymbol{k}'q_z} = \left(\varepsilon^{\mathrm{e}}_{i\boldsymbol{k}} + \varepsilon^{\mathrm{h}}_{j\boldsymbol{k}'} + \hbar\omega_{\mathrm{LO}}\right)\delta s^{\mathrm{he}(1,1)ji}_{\boldsymbol{k}\boldsymbol{k}'q_z} && \Big] H_0\\
&\quad + (1+n_{\mathrm{B}})\Big[\sum_{i_1} g^{*i_1 i}_{\boldsymbol{q}}\, p^{(1,0)}_{ji_1\boldsymbol{k}'} - \sum_{j_1} g^{*ij_1}_{\boldsymbol{q}}\, p^{(1,0)}_{j_1 i\boldsymbol{k}}\Big] && \Big] H_{\mathrm{Fr}}\\
&\quad + \mathscr{U}^{\mathrm{Cshe}(1,1)}_{ij\boldsymbol{k}\boldsymbol{k}'q_z} && \Big] H_{\mathrm{Cb}}
\end{aligned}
$$

$$
\begin{aligned}
&\mathrm{i}\hbar\frac{\mathrm{d}}{\mathrm{d}t}\delta s^{\mathrm{hek}(1,1)ji}_{\boldsymbol{k}\boldsymbol{k}'q_z} = \left(\varepsilon^{\mathrm{e}}_{i\boldsymbol{k}'} + \varepsilon^{\mathrm{h}}_{j\boldsymbol{k}} - \hbar\omega_{\mathrm{LO}}\right)\delta s^{\mathrm{hek}(1,1)ji}_{\boldsymbol{k}\boldsymbol{k}'q_z} && \Big] H_0\\
&\quad + n_{\mathrm{B}}\Big[\sum_{i_1} g^{ii_1}_{\boldsymbol{q}}\, p^{(1,0)}_{ji_1\boldsymbol{k}} - \sum_{j_1} g^{j_1 j}_{\boldsymbol{q}}\, p^{(1,0)}_{j_1 i\boldsymbol{k}'}\Big] && \Big] H_{\mathrm{Fr}}\\
&\quad + \mathscr{U}^{\mathrm{Cshek}(1,1)}_{ij\boldsymbol{k}\boldsymbol{k}'q_z} && \Big] H_{\mathrm{Cb}}
\end{aligned}
$$

$$
\begin{aligned}
\mathrm{i}\hbar\frac{\mathrm{d}}{\mathrm{d}t}B^{(2,1)}_{q_z} = \quad & \hbar\omega_{\mathrm{LO}}B^{(2,1)}_{q_z} && \Big] H_0 \\
& + 2^* \sum_{i_1 i_2 \boldsymbol{k_1}} g^{*\,i_1 i_2}_{q_z} f^{\mathrm{e}(2,0)}_{i_2 i_1 \boldsymbol{k_1}} - 2^* \sum_{j_1 j_2 \boldsymbol{k_1}} g^{*\,j_2 j_1}_{q_z} f^{\mathrm{h}(2,0)}_{j_2 j_1 \boldsymbol{k_1}} && \Big] H_{\mathrm{Fr}}
\end{aligned}
$$

$$
\begin{aligned}
\mathrm{i}\hbar\frac{\mathrm{d}}{\mathrm{d}t}\delta b^{(2,2)}_{\boldsymbol{k}q_z q_z'} = \; & 2\hbar\omega_{\mathrm{LO}}\,\delta b^{(2,2)}_{\boldsymbol{k}q_z q_z'} && \Big] H_0 \\
& + 2^* \sum_{i_1 i_2} \left(g^{*\,i_1 i_2}_{-\boldsymbol{k}+q_z'\boldsymbol{e}_z} \delta S^{\mathrm{e}\,(2,1)\,i_2 i_1}_{\boldsymbol{k}q_z} + g^{*\,i_1 i_2}_{\boldsymbol{k}+q_z\boldsymbol{e}_z} \delta S^{\mathrm{e}\,(2,1)\,i_2 i_1}_{\boldsymbol{k}q_z'} \right) \\
& + 2^* \sum_{j_1 j_2} \left(- g^{*\,j_2 j_1}_{-\boldsymbol{k}+q_z'\boldsymbol{e}_z} \delta S^{\mathrm{h}\,(2,1)\,j_2 j_1}_{\boldsymbol{k}q_z} - g^{*\,j_2 j_1}_{\boldsymbol{k}+q_z\boldsymbol{e}_z} \delta S^{\mathrm{h}\,(2,1)\,j_2 j_1}_{\boldsymbol{k}q_z'} \right) && \Big] H_{\mathrm{Fr}}
\end{aligned}
$$

$$
\begin{aligned}
\mathrm{i}\hbar\frac{\mathrm{d}}{\mathrm{d}t}\delta n^{(2,2)}_{\boldsymbol{k}q_z q_z'} = \; & 2^* \sum_{i_1 i_2} \left(- g^{i_1 i_2}_{\boldsymbol{k}+q_z\boldsymbol{e}_z} \delta S^{\mathrm{e}\,(2,1)\,i_1 i_2}_{\boldsymbol{k}q_z'} + g^{*\,i_1 i_2}_{\boldsymbol{k}+q_z'\boldsymbol{e}_z} \delta S^{\mathrm{e}\,(2,1)*\,i_1 i_2}_{\boldsymbol{k}q_z} \right) && \Big] H_{\mathrm{Fr}} \\
& + 2^* \sum_{j_1 j_2} \left(g^{j_2 j_1}_{\boldsymbol{k}+q_z\boldsymbol{e}_z} \delta S^{\mathrm{h}\,(2,1)\,j_1 j_2}_{\boldsymbol{k}q_z'} - g^{*\,j_2 j_1}_{\boldsymbol{k}+q_z'\boldsymbol{e}_z} \delta S^{\mathrm{h}\,(2,1)*\,j_1 j_2}_{\boldsymbol{k}q_z} \right) &&
\end{aligned}
$$

List of symbols

This list is limited to symbols that are used in several places but are only defined once. If a symbol is not listed here, it might refer to a material parameter (section 5.1.1) or serve as an abbreviation for a dynamical variable (section 5.3).

symbol	meaning	see page
2^*	a factor of two that results from an implicit spin sum	28
A	system area in in-plane direction	13
$b_{\alpha,\boldsymbol{q}}$, $b^\dagger_{\alpha,\boldsymbol{q}}$	phonon operators, α is branch index	11
$b_{\boldsymbol{q}}$, $b^\dagger_{\boldsymbol{q}}$	phonon operators, LO branch	18
$\boldsymbol{e}_\mathrm{z}$	unit vector in z-direction	
$g^{n_1 n_2}_{\boldsymbol{q}}$	Fröhlich coupling element	18
N	number of primitive unit cells in system volume	11
$\hat{\boldsymbol{p}}(\boldsymbol{r})$	lattice momentum operator	12
$\hat{\boldsymbol{P}}$	spatial average of $\hat{\boldsymbol{p}}(\boldsymbol{r})$	45
$\phi^{\mathrm{e/h}}_n(z)$	electron/hole envelope function	14
τ	FWHM of laser pulse (field amplitude, not intensity)	17
$\hat{\boldsymbol{u}}(\boldsymbol{r})$	lattice displacement operator	12
$\hat{\boldsymbol{U}}$	spatial average of $\hat{\boldsymbol{u}}(\boldsymbol{r})$	45
V	system volume	11
$V^{n_1 n_2 n_3 n_4}_{\boldsymbol{k}}$	Coulomb matrix element	16
ω_0	laser central frequency	17

List of publications

T. Papenkort, V. M. Axt, and T. Kuhn: Optical excitation of squeezed longitudinal optical phonon states in an electrically biased quantum well, Phys. Rev. B **85**, 235317 (2012).

J. M. Daniels, T. Papenkort, D. E. Reiter, T. Kuhn, and V. M. Axt: Quantum kinetics of squeezed lattice displacement generated by phonon down conversion, Phys. Rev. B **84**, 165310 (2011).

T. Papenkort, T. Kuhn, and V. M. Axt: Generation of coherent LO phonons in optically driven quantum wells, Phys. Status Solidi C **8**, 1121 (2011).

D. E. Reiter, D. Wigger, J. M. Daniels, T. Papenkort, A. Vagov, V. M. Axt, and T. Kuhn: Fluctuation properties of phonons generated by ultrafast optical excitation of a quantum dot, Phys. Status Solidi B **248**, 825 (2010).

T. Papenkort, T. Kuhn, and V. M. Axt: Resonant generation of coherent LO phonons by charge oscillations in a biased quantum well, Phys. Rev. B **81**, 205320 (2010).

T. Papenkort, T. Kuhn, and V. M. Axt: Interplay between coherent and incoherent phonons in optically excited biased quantum wells, J. Phys.: Conf. Ser. **210**, 012054 (2010).

D. E. Reiter, S. Sauer, J. Huneke, T. Papenkort, T. Kuhn, A. Vagov, and V. M. Axt: Generation of squeezed phonon states by optical excitation of a quantum dot, J. Phys. Conf. Ser. **193**, 012121 (2009).

T. Papenkort, T. Kuhn, and V. M. Axt: Nonequilibrium dynamics and coherent control of BCS superconductors driven by ultrashort THz pulses, J. Phys.: Conf. Ser. **193**, 012050 (2009).

T. Papenkort, T. Kuhn, and V. M. Axt: Ultrafast coherent dynamics in optically driven BCS systems, Phys. Status Solidi B **246**, 325 (2009).

T. Papenkort, T. Kuhn, and V. M. Axt: Coherent control of the gap dynamics of BCS superconductors in the nonadiabatic regime, Phys. Rev. B **78**, 132505 (2008),
also published in Virtual Journal of Ultrafast Science **7**, Issue 11 (2008).

T. Papenkort, V. M. Axt, and T. Kuhn: Coherent dynamics and pump-probe spectra of BCS superconductors, Phys. Rev. B **76**, 224522 (2007),
also published in Virtual Journal of Ultrafast Science **7**, Issue 1 (2008).

References

[1] S. Adachi: GaAs and related materials: Bulk semiconducting and superlattice properties, World Scientific, Singapore (1994).

[2] V. M. Axt, G. Bartels, and A. Stahl: Intraband dynamics at the semiconductor band edge: Shortcomings of the Bloch equation method, Phys. Rev. Lett. **76**, 2543 (1996).

[3] V. M. Axt and A. Stahl: A dynamics-controlled truncation scheme for the hierarchy of density matrices in semiconductor optics, Z. Phys. B **93**, 195 (1994).

[4] M. Bargheer, N. Zhavoronkov, Y. Gritsai, J. C. Woo, D. S. Kim, M. Woerner, and T. Elsaesser: Coherent atomic motions in a nanostructure studied by femtosecond x-ray diffraction, Science **306**, 1771 (2004).

[5] M. Bargheer, N. Zhavoronkov, J. C. Woo, D. S. Kim, M. Woerner, and T. Elsaesser: Excitation mechanisms of coherent phonons unravelled by femtosecond x-ray diffraction, Phys. Status Solidi B **243**, 2389 (2006).

[6] G. Bastard: Wave mechanics applied to semiconductor heterostructures, Halsted Press, New York (1988).

[7] R. P. Beardsley, A. V. Akimov, M. Henini, and A. J. Kent: Coherent terahertz sound amplification and spectral line narrowing in a Stark ladder superlattice, Phys. Rev. Lett. **104**, 085501 (2010).

[8] W. E. Bron, J. Kuhl, and B. K. Rhee: Picosecond-laser-induced transient dynamics of phonons in GaP and ZnSe, Phys. Rev. B **34**, 6961 (1986).

[9] A. Carmele, M. Richter, W. W. Chow, and A. Knorr: Antibunching of thermal radiation by a room-temperature phonon bath: A numerically solvable model for a strongly interacting light-matter-reservoir system, Phys. Rev. Lett. **104**, 156801 (2010).

[10] T. K. Cheng, J. Vidal, H. J. Zeiger, G. Dresselhaus, M. S. Dresselhaus, and E. P. Ippen: Mechanism for displacive excitation of coherent phonons in Sb, Bi, Te, and Ti_2O_3, Appl. Phys. Lett. **59**, 1923 (1991).

[11] G. C. Cho, W. Kütt, and H. Kurz: Subpicosecond time-resolved coherent-phonon oscillations in GaAs, Phys. Rev. Lett. **65**, 764 (1990).

[12] C. Cohen-Tannoudji, J. Dupont-Roc, and G. Grynberg: Photons and Atoms, chapter 3, John Wiley & Sons, New York (1989).

[13] J. M. Daniels, T. Papenkort, D. E. Reiter, T. Kuhn, and V. M. Axt: Quantum kinetics of squeezed lattice displacement generated by phonon down conversion, Phys. Rev. B **84**, 165310 (2011).

[14] T. Dekorsy, A. Bartels, H. Kurz, K. Köhler, R. Hey, and K. Ploog: Coupled Bloch-phonon oscillations in semiconductor superlattices, Phys. Rev. Lett. **85**, 1080 (2000).

[15] T. Dekorsy, G. Cho, and H. Kurz: Coherent phonons in condensed media, in M. Cardona and G. Güntherodt (Editors), Light Scattering in Solids VIII, volume 76 of *Topics in Applied Physics*, pp. 169–209, Springer-Verlag Berlin Heidelberg (2000), also available at http://nbn-resolving.de/urn:nbn:de:bsz:352-opus-121275.

[16] T. Dekorsy, T. Pfeifer, W. Kütt, and H. Kurz: Subpicosecond carrier transport in GaAs surface-space-charge fields, Phys. Rev. B **47**, 3842 (1993).

[17] T. Eberle, S. Steinlechner, J. Bauchrowitz, V. Händchen, H. Vahlbruch, M. Mehmet, H. Müller-Ebhardt, and R. Schnabel: Quantum enhancement of the zero-area Sagnac interferometer topology for gravitational wave detection, Phys. Rev. Lett. **104**, 251102 (2010).

[18] M. Fox: Optical properties of solids, Oxford University Press, New York (2001).

[19] D. Gammon, B. V. Shanabrook, and D. S. Katzer: Excitons, phonons, and interfaces in GaAs/AlAs quantum-well structures, Phys. Rev. Lett. **67**, 1547 (1991).

[20] G. A. Garrett, T. F. Albrecht, J. F. Whitaker, and R. Merlin: Coherent THz phonons driven by light pulses and the Sb problem: What is the mechanism?, Phys. Rev. Lett. **77**, 3661 (1996).

[21] G. A. Garrett, A. G. Rojo, A. K. Sood, J. F. Whitaker, and R. Merlin: Vacuum squeezing of solids: Macroscopic quantum states driven by light pulses, Science **275**, 1638 (1997).

[22] A. W. Ghosh, L. Jönsson, and J. W. Wilkins: Bloch oscillations in the presence of plasmons and phonons, Phys. Rev. Lett. **85**, 1084 (2000).

[23] R. T. Harley: Spin dynamics of free carriers in quantum wells, in M. I. Dyakonov (Editor), Spin physics in semiconductors, volume 157 of *Springer series in solid-state sciences*, chapter 2, pp. 29–54, Springer-Verlag Berlin Heidelberg (2008).

[24] X. Hu and F. Nori: Squeezed phonon states: Modulating quantum fluctuations of atomic displacements, Phys. Rev. Lett. **76**, 2294 (1996).

[25] X. Hu and F. Nori: Phonon squeezed states generated by second-order Raman scattering, Phys. Rev. Lett. **79**, 4605 (1997).

[26] X. Hu and F. Nori: Phonon squeezed states: quantum noise reduction in solids, Phys. B **263-264**, 16 (1999).

[27] A. Hussain and S. R. Andrews: Absence of phase-dependent noise in time-domain reflectivity studies of impulsively excited phonons, Phys. Rev. B **81**, 224304 (2010).

[28] S. L. Johnson, P. Beaud, E. Vorobeva, C. J. Milne, E. D. Murray, S. Fahy, and G. Ingold: Directly observing squeezed phonon states with femtosecond x-ray diffraction, Phys. Rev. Lett. **102**, 175503 (2009).

[29] Y. Kasai, D. Suzuki, H. Kunugita, and K. Ema: Resonantly excited coherent optical phonons in wide-gap semiconductor ZnTe, J. Lumin. **129**, 1820 (2009).

[30] O. Kojima, K. Mizoguchi, and M. Nakayama: Enhancement of coherent longitudinal optical phonon oscillations in a GaAs/AlAs multiple quantum well due to intersubband energy tuning under an electric field, Phys. Rev. B **70**, 233306 (2004).

[31] A. Krügel, V. Axt, T. Kuhn, P. Machnikowski, and A. Vagov: The role of acoustic phonons for Rabi oscillations in semiconductor quantum dots, Appl. Phys. B **81**, 897 (2005).

[32] T. Kuhn: Ladungsträgerdynamik in Halbleitersystemen fern vom Gleichgewicht: Elektronisches Rauschen und kohärente Prozesse, Verlag Shaker, Aachen (1994).

[33] T. Kuhn: Density matrix theory of coherent ultrafast dynamics, in E. Schöll (Editor), Theory of transport properties of semiconductor nanostructures, pp. 173–214, Chapman and Hall, London (1998).

[34] W. A. Kütt, W. Albrecht, and H. Kurz: Generation of coherent phonons in condensed media, IEEE J. Quantum Electron. **28**, 2434 (1992).

[35] A. V. Kuznetsov and C. J. Stanton: Theory of coherent phonon oscillations in semiconductors, Phys. Rev. Lett. **73**, 3243 (1994).

[36] A. V. Kuznetsov and C. J. Stanton: Coherent phonon oscillations in GaAs, Phys. Rev. B **51**, 7555 (1995).

[37] A. V. Kuznetsov and C. J. Stanton: Theory of coherent phonon oscillations in bulk GaAs, in K. Tsen (Editor), Ultrafast phenomena in semiconductors, pp. 353–403, Springer, New York (2001).

[38] M. V. Lebedev and O. V. Misochko: Generation of coherent phonons in opaque crystals: A radio engineering analogy, Phys. Solid State **51**, 1843 (2009).

[39] Y.-S. Lim, S.-C. Yoon, K.-J. Yee, Y.-H. Ahn, E. Oh, and J.-H. Lee: Coherent optical phonon oscillations in cubic ZnSe, Appl. Phys. Lett. **82**, 2446 (2003).

[40] R. Loudon and P. L. Knight: Squeezed light, J. Mod. Opt. **34**, 709 (1987).

[41] O. Madelung: Introduction to solid-state theory, Springer-Verlag Berlin (1981).

[42] A. Melnikov, O. Misochko, and S. Chekalin: Generation of coherent phonons in bismuth by ultrashort laser pulses in the visible and NIR: Displacive versus impulsive excitation mechanism, Phys. Lett. A **375**, 2017 (2011).

[43] R. Merlin: Generating coherent THz phonons with light pulses, Solid State Commun. **102**, 207 (1997).

[44] O. V. Misochko: Coherent phonons and their properties, JETP **92**, 246 (2001).

[45] O. V. Misochko, K. Kisoda, K. Sakai, and S. Nakashima: Peculiar noise properties of phonons generated by femtosecond laser pulses in antimony, Appl. Phys. Lett. **76**, 961 (2000).

[46] O. V. Misochko, K. Sakai, and S. Nakashima: Phase-dependent noise in femtosecond pump-probe experiments on Bi and GaAs, Phys. Rev. B **61**, 11225 (2000).

[47] K. Mizoguchi, Y. Kanzawa, S. Saito, K. Sakai, and M. Nakayama: Enhanced terahertz emission from coherent longitudinal optical phonons in a quantum well structure under applied bias, Appl. Phys. Lett. **94**, 171105 (2009).

[48] K. Mizoguchi, O. Kojima, T. Furuichi, M. Nakayama, K. Akahane, N. Yamamoto, and N. Ohtani: Coupled mode of the coherent optical phonon and excitonic quantum beat in GaAs/AlAs multiple quantum wells, Phys. Rev. B **69**, 233302 (2004).

[49] M. Nakayama, S.-i. Ito, K. Mizoguchi, S. Sait, and K. Sakai: Generation of intense and monochromatic terahertz radiation from coherent longitudinal optical phonons in GaAs/AlAs multiple quantum wells at room temperature, Appl. Phys. Expr. **1**, 012004 (2008).

[50] T. Pfeifer, T. Dekorsy, W. Kütt, and H. Kurz: Generation mechanism for coherent LO phonons in surface-space-charge fields of III-V-compounds, Appl. Phys. A: Mater. Sci. Process. **55**, 482 (1992).

[51] D. E. Reiter, S. Sauer, J. Huneke, T. Papenkort, T. Kuhn, A. Vagov, and V. M. Axt: Generation of squeezed phonon states by optical excitation of a quantum dot, J. Phys. Conf. Ser. **193**, 012121 (2009).

[52] D. E. Reiter, D. Wigger, V. M. Axt, and T. Kuhn: Generation and dynamics of phononic cat states after optical excitation of a quantum dot, Phys. Rev. B **84**, 195327 (2011).

[53] F. Rossi and T. Kuhn: Theory of ultrafast phenomena in photoexcited semiconductors, Rev. Mod. Phys. **74**, 895 (2002).

[54] S. Sauer, J. M. Daniels, D. E. Reiter, T. Kuhn, A. Vagov, and V. M. Axt: Lattice fluctuations at a double phonon frequency with and without squeezing: An exactly solvable model of an optically excited quantum dot, Phys. Rev. Lett. **105**, 157401 (2010).

[55] Y. Shinohara, K. Yabana, Y. Kawashita, J.-I. Iwata, T. Otobe, and G. F. Bertsch: Coherent phonon generation in time-dependent density functional theory, Phys. Rev. B **82**, 155110 (2010).

[56] T. E. Stevens, J. Kuhl, and R. Merlin: Coherent phonon generation and the two stimulated Raman tensors, Phys. Rev. B **65**, 144304 (2002).

[57] D. Strauch and B. Dorner: Phonon dispersion in GaAs, J. Phys.: Condens. Matter **2**, 1457 (1990).

[58] M. Tegmark and H. S. Shapiro: Decoherence produces coherent states: An explicit proof for harmonic chains, Phys. Rev. E **50**, 2538 (1994).

[59] F. Vallée and F. Bogani: Coherent time-resolved investigation of LO-phonon dynamics in GaAs, Phys. Rev. B **43**, 12049 (1991).

[60] M. E. Wieser and T. B. Coplen: Atomic weights of the elements 2009 (IUPAC Technical Report), Pure Appl. Chem. **83**, 359 (2011).

[61] H. J. Zeiger, J. Vidal, T. K. Cheng, E. P. Ippen, G. Dresselhaus, and M. S. Dresselhaus: Theory for displacive excitation of coherent phonons, Phys. Rev. B **45**, 768 (1992).

[62] W. H. Zurek: Decoherence, einselection, and the quantum origins of the classical, Rev. Mod. Phys. **75**, 715 (2003).

Danke!

Dank gebührt Prof. Tilmann Kuhn und Prof. Martin Axt; Doris, Jonas, Jan, Paul, Sebi, Eva, Piotrek, Julian, Tomek, Peter, Dan, Thorsten, Matthias, Ansgar, Kasia, Paweł, ebenso Sandra und Daniel; Simon, Giso, Stefan und Anne-Nicole, Johannes, Christian und Ludwig; und meiner Familie.